Luminescent Guest Encapsulated Metal-Organic Framework Composites for Photonic Sensing Technology

Yang Zhang

Lady Margaret Hall

University of Oxford

A thesis submitted for the degree of

Doctor of Philosophy

Hilary 2022

This thesis is dedicated to my parents,

Zhongyi Zhang (张仲义) and Juhong Zhang (张举红),

and to my family in China.

…

Their endless love and support made me the person I am today.

I would not be standing at the end of this long journey if not for them.

PREFACE

This thesis is submitted for the degree of Doctor of Philosophy in the University of Oxford, United Kingdom. The research presented in this work was carried out by the author between October 2018 and December 2021 in the Department of Engineering Science, under the supervision of Professor Jin-Chong Tan.

To the best of my knowledge, the work described in this dissertation is original, except where due reference has been made, acknowledging the work of others. Nothing has been included that is the outcome of work done in collaboration with others, except where explicitly noted. No part of this dissertation, or any similar to it, has been, or is currently being submitted for any degree at this, or any other university. This thesis is less than 250 pages in length.

The work presented herein has been partially published/submitted in the following journal papers:

1. **Y. Zhang**, M. Gutiérrez, A.K. Chaudhari, and J.C. Tan, "Dye-Encapsulated Zeolitic Imidazolate Framework (ZIF-71) for Fluorochromic Sensing of Pressure, Temperature, and Volatile Solvents", *ACS Applied Materials & Interfaces*, 12, 37477-37488 (2020).
2. **Y. Zhang** and J.C. Tan, "Electrospun Rhodamine@MOF/Polymer Luminescent Fibers with a Quantum Yield of Over 90%", *iScience*, 24, 103035 (2021).
3. T. Xiong, **Y. Zhang**, L. Donà, M. Gutiérrez, A.F. Möslein, A.S. Babal, N. Amin, B. Civalleri, and J.C. Tan, "Tunable Fluorescein-Encapsulated Zeolitic Imidazolate Framework-8 Nanoparticles for Solid-State Lighting", *ACS Applied Nano Materials*, 4, 10321-10333 (2021). <Co-First Authorship>

4. **Y. Zhang**, T. Xiong, A.F. Möslein, S. Mollick, V. Kachwal, A.S. Babal, N. Amin and J.C. Tan, "Nanoconfinement of Tetraphenylethylene in Zeolitic Metal-Organic Framework for Turn-On Mechanofluorochromic Stress Sensing", *Applied Materials Today*, 27, 101434 (2022).
5. M. Gutiérrez, **Y. Zhang**, and J.C. Tan, "Confinement of Luminescent Guests in Metal-Organic Frameworks: Understanding Pathways from Synthesis and Multimodal Characterization to Potential Applications of LG@MOF Systems", *Chemical Reviews* (2022). <Review Article, Co-First Authorship>
6. **Y. Zhang**, S. Mollick, M. Tricarico, J. Ye, D. Sherman, J.C. Tan, "Turn-On Fluorescence Chemical Sensing Through Transformation of Self-Trapped Exciton States at Room Temperature", Submitted (2022).

Yang Zhang

Oxford

ABSTRACT

Luminescent metal-organic frameworks (LMOFs) are promising hybrid materials and are considered ideal for fabricating sensors and optoelectronics. A unique direction of LMOFs research is to harness MOFs as 'hosts' to encapsulate various luminescent 'guest' (LG) molecules for producing LG@MOF systems. However, feasible design ideas and in-depth mechanism analyses are scarce, compromising their practical engineering potential. This section, combined with the structure, synthesis, types, and applications of LG@MOF systems, is described in detail in Chapter 1 and 2.

In Chapter 3, 4, and 5, three new LG@MOF systems have been designed and prepared. The results demonstrated that effective wavelength-tuning (~ tens of nanometres) or turn-on (~ tenfold) type sensing materials could be readily synthesised even with common fluorescent materials (e.g., rhodamine B, tetraphenylethylene, perylene). Different polymers have been combined with the obtained LG@MOF systems to enhance stability and processability.

Detailed photophysical characterisations have been conducted to investigate the obtained LG@MOF systems. By analysing the excitation, emission, lifetime, and quantum yield, three novel sensing mechanisms have been proposed: (i) Guest aggregates of different sizes are protected differently by the MOF, thus, generating sensing behaviours. Moreover, the configuration of the guest aggregates may change under stimuli leading to further sensing performance (Chapter 3); (ii) MOF can provide a strong caging effect to aggregation-induced emission (AIE) materials resulting in turn-on type mechanochromism (Chapter 4); (iii) The lattice of MOF can influence the electron-phonon coupling of guest excimers causing distinct luminescent properties (Chapter 5).

Overall, this work helps address the pain points of LG@MOFs research and illustrates the possibility for large scale production, which may inspire more research into high-performance fluorescent sensors. These are summarised in Chapter 6, along with some specific examples of future development.

ACKNOWLEDGEMENTS

I would particularly like to thank my supervisor, Professor Jin-Chong Tan, for his intellectual and moral support throughout my research. I am especially grateful to Professor Tan for his continuous guidance, constant encouragement, and fun-filled squash training sessions. His immense knowledge and plentiful experience have inspired me in all the time of my academic research and daily life.

Many thanks also to my College for providing funding, comfortable accommodation, and fitting workstations. I am thankful to the Diamond Light Source and Research Complex at Harwell for allowing me to conduct beamtime experiments and use the advanced facilities.

I am truly grateful to all my colleagues in the Multifunctional Materials and Composites Laboratory not only for the countless great scientific discussions, but also for the numerous happy time we have shared. Special thanks to Abhijeet, Annika, Arun, Bárbara, Dylan, Jiahao, Kirill, Mario, Michele, Samraj, Sujeet, Tao, Vishal, Yueting, Zhixin for their deep friendship and assistance. To all of you, thank you for the laughs, group lunches, punting, volleyball, etc.

I would like to thank my girlfriend, basketball teammates, and all friends outside the lab who have made the past few years some of the best in my life. The fond memories of our training, games, trips, dinners, and parties will always inspire me to keep going. Last but not least, I would like to thank my Dad and Mom, to whom this thesis is dedicated, for their support and encouragement!

Contents

List of Figures

List of Tables

List of Abbreviations

ACN	Acetonitrile
ACQ	Aggregation-caused quenching
AIE	Aggregation-induced emission
ANT	Anthracene
ATR-FTIR	Fourier transform infrared spectroscopy with attenuated total reflection
bdc	Benzenedicarboxylate
BTX	Benzene, toluene, and xylene
B3LYP	Becke, 3 parameter, Lee Yang Parr
CSM	Continuous stiffness measurement
dcIm	4,5-Dichloroimidazole
DCM	4-(Dicyanomethylene)-2-methyl-6-(4-dimethylaminostyryl)-4H pyran
DE	Diethyl ether
DFT	Density functional theory
DIC	Dichloromethane
DMA	N,N-Dimethylacetamide
DMF	N,N-Dimethylformamide
DO	Dioxane
dpNDI	N,N′-Di(4-pyridyl)-1,4,5,8-naphthalenediimide

Gaq_3	Gallium(III) tris(8-hydroxyquinolinato)
HCR	High-concentration reaction
LG	Luminescent guest
LMCT	Ligand metal charge transfer
MIL	Materials of Institute Lavoisier
mIm	2-methylimidazolate
MOF	Metal-organic framework
NanoFTIR	Nanoscale Fourier transform infrared spectroscopy
NC	Metal nanocluster
NDC	Naphthalene dicarboxylic acid
NMR	Nuclear magnetic resonance
NP	Nanoparticle
PEG	Polyethylene glycol
PMMA	Polymethyl methacrylate
PTA	*p*-Phthalic acid
PU	Polyurethane
PVAc	Polyvinyl acetate
PVDF	Polyvinylidene difluoride
PXRD	Powder X-ray diffraction
QD	Quantum dot
QY	Quantum yield
Rh6G	Rhodamine 6G
RhB	Rhodamine B

RT	Room temperature
SEM	Scanning electron microscopy
SWCNT	Single-walled carbon nanotube
TCPE	Tetrakis(4-carboxyphenyl)ethylene
TEA	Triethylamine
TEM	Transmission electron microscopy
TGA	Thermogravimetric analysis
THF	Tetrahydrofuran
TNP	2,4,6-Trinitrophenol
TPE	Tetraphenylethene
tpt	2,4,6-Tri(4-pyridinyl)-1,3,5-triazine
UiO	University of Oslo
UV	Ultraviolet
UV-Vis	Ultraviolet-visible
VOC	Volatile organic compound
ZIF	Zeolitic imidazolate framework
ZnQ	Zinc bis-(8-hydroxyquinoline)

List of Symbols

°C	Degrees Celsius
Å	Angstroms
cm	Centimetres
K	Kelvin
m	Mass
M	Molecular weight
m	Meters
mm	Millimetres
n	Number of moles
nm	Nanometres
T_m	Melting Temperature
λ	Wavelength
µL	Microliters
µm	Micrometres

1

Introduction

The core of sensor-related research is to accurately detect and quantify different chemical substances or physical quantities, which is key to many application fields, such as environmental detection, clinical diagnosis, engineering monitoring, etc. [1, 2] Within sensor-related research, fluorescence sensing has attracted increasing attention in recent decades. This type of sensing uses the change in fluorescence signals (i.e., peak intensity increase/decrease; peak wavelength shift) to detect and track the presence of a specific analyte or target condition. Compared to other sensing types, such as electronic and other optical sensors (i.e. using dielectric constants [3, 4], diffraction [5], scattering [6], refractive index [7], etc. as sensing signals), fluorescence sensing is considered to have high sensitivity, high selectivity, broad adaptability, and technical simplicity [8]. It does not require complex instrumentations and can be manufactured into portable sensing devices [8, 9], therefore, offering many promising application prospects.

Among the various materials proposed for making fluorescent sensors, such as inorganic luminescent materials [10] and organic derivatives [8], metal-organic frameworks (MOFs) have been demonstrated as one of the most propitious candidates [11, 12]. MOFs are extended crystalline materials consisting of metal ions/clusters as nodes coordinated by multitopic organic ligands (linkers), giving

rise to a long-range ordered, nanoporous, and highly tuneable structure (Figure 1.1). Theoretically, the fluorescent properties of MOFs are diverse, and by tailoring their molecular building blocks (i.e. metal centres and/or organic linkers), a variety of fluorescence sensing performances can be readily prepared. Moreover, due to the filter and preconcentration effect, the controllable porous MOF structure may help to optimise the sensing selectivity and sensitivity (Figure 1.1). Thus, it is known that MOFs are a good platform for making fluorescence sensing materials.

The fluorescence sensing properties of MOF can be further enhanced by encapsulating luminescent guests to form the 'guest@MOF' system. As shown in Figure 1.1, the resulting composite system can leverage the porous architecture of the MOF host and may further enhance the functions of the confined guests within the nanopores. On the one hand, it can exploit the porosity of MOF to apply a caging effect (i.e. restricting the vibration of the guests within a confined environment), reduce the non-radiative decay of the guest, help to overcome the aggregation-caused quenching (ACQ) phenomenon, thereby broadening the application of conventional luminescent materials with improved fluorescent properties. On the other hand, in the guest@MOF system, specific host-guest interactions can be introduced by simply changing the building blocks of MOF host to generate fluorescence sensing behaviour. More importantly, the structural parameters of MOFs (e.g., framework topology, pore size, pore chemical affinity, etc.) can be rationally designed and controlled, which allow a wide variety of guests to be encapsulated at the nanoscale. Based on these advantages, it is feasible to design

more high-performance smart fluorescence sensors by harnessing the concept of guest@MOF nanoconfined materials.

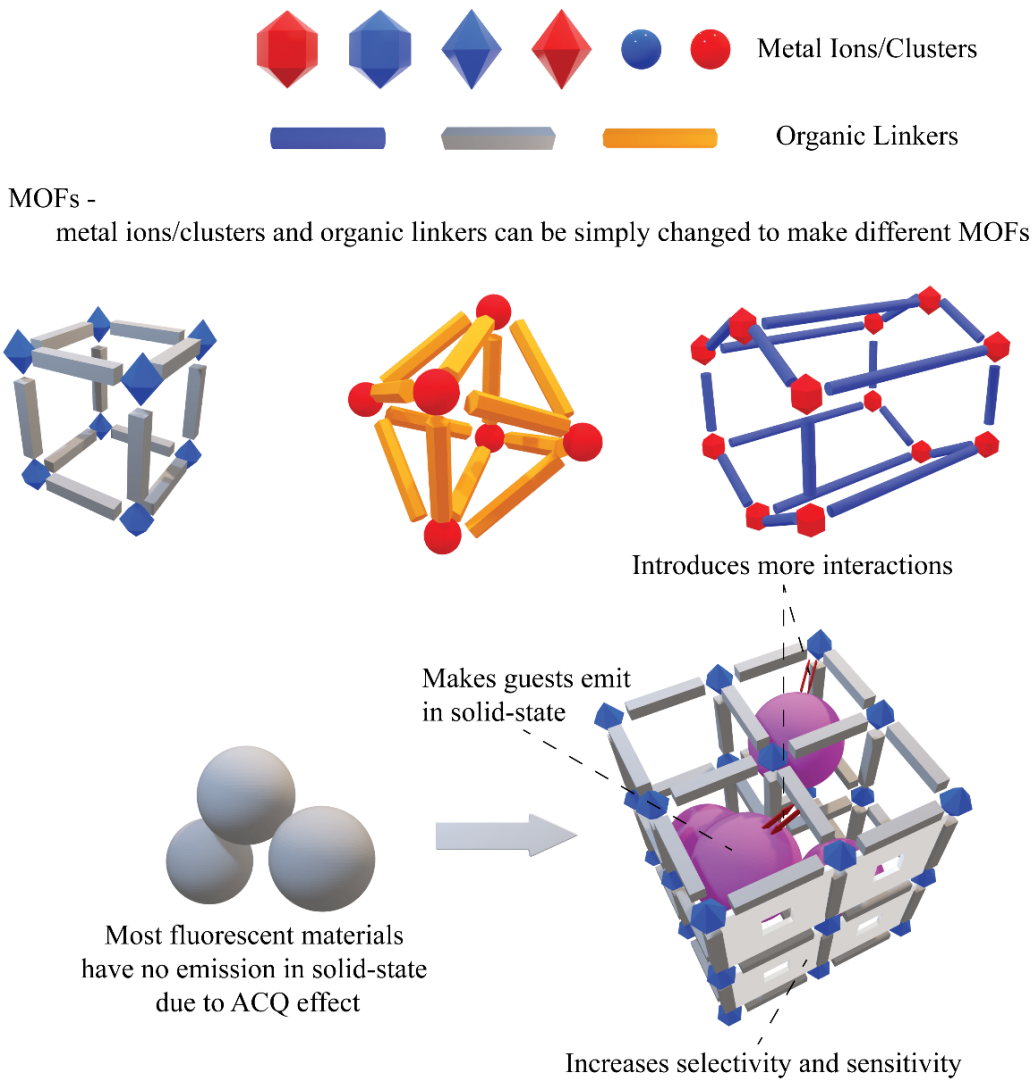

Figure 1.1. Schematic of the tuneable architectural features of MOF and the benefits conferred by the guest@MOF composite system.

However, the research on guest@MOF systems is still in its infancy [12]. For example, the sensing mechanisms reported so far are lacklustre, and there is a lack of comprehensive study of the fluorescence sensing mechanism based on the

photophysics. These shortcomings result in that the existing guest@MOF systems generally do not have real engineering applications.

This DPhil thesis aims to address the aforementioned challenges by designing more robust fluorescence sensing guest@MOF systems, and comprehensively analysing the underpinning mechanisms from the perspective of photophysics. This paper-based integrated thesis consists of three main parts:

- Part I: Introduction and brief literature review
- Part II: Summary of novel fluorescent guest@MOF systems developed by the author and a photophysical study of their sensing mechanisms
- Part III: Published papers

Structure, property, application, and their relationships are the main focus of MOF-related research. Therefore, after briefly describing the aims and objectives (Chapter 1), Part I gives a short literature review on the concept, structures, synthesis methods, guest types, and applications of the representative guest@MOF systems reported to date (Chapter 2).

Distinct from the previous research mentioned in the literature, the author designed some new guest@MOF systems with promising sensing performance by changing the type or functions of luminescent guests confined within the MOF host. Most of them were further made into guest@MOF/polymer composites with practical engineering application potential. Part II explains these design ideas and the resultant sensing behaviour in response to physical and chemical stimuli, and

demonstrates the underlying mechanisms through rigorous photophysical characterisation, especially emission/excitation spectra, fluorescence lifetime, and quantum yield data (Chapters 3, 4, and 5). Chapter 6 gives an overall summary of the author's doctoral research and personal opinions on future developments in the field of guest@MOF fluorescence sensing.

Part III is the collection of peer-reviewed papers published or submitted, in which the different material systems described in Part II are reported in full.

2

Literature Review

2.1 Basic Concept of Guest@MOF System

Metal-organic frameworks (MOFs), also known as coordination polymers, are an interesting class of nanoporous crystalline materials that can be regarded as a generalised inorganic-organic hybrid material, comprising organic 'bridging' ligands connected by coordination bonds to metal ions or clusters (Figure 1.1).

Compared with traditional porous materials, such as hypercrosslinked polymers, zeolites, and porous carbons, the unique structural features of MOFs allow them to combine the benefits of traditional materials with their own unique advantages:

i. MOF is highly crystalline, which is helpful for the determination of its precise spatial structure using single crystal and polycrystalline diffraction methods [13]. This can provide important information about structural changes for the specific analysis of MOF to enable rational design and crystal engineering of materials for practical applications.

ii. Due to the relatively long bridging organic ligands, MOFs can exhibit an exceedingly high porosity and specific surface area. For example, the porosity of MOF-399 can reach 94%, and its specific surface area is as high as 7140 m^2/g [14].

iii. The framework structure of MOFs has a certain degree of mechanical flexibility because MOFs have coordination bonds in the structure [15]. This flexibility may result in intriguing chemical/physical functions and anomalous mechanical properties, such as the multi-step adsorption/desorption process, negative Poisson's ratio and negative thermal expansion [16]. Traditional inorganic molecular sieve materials such as zeolites do not have this feature.

iv. The structure of MOFs is very diverse and tuneable. Both of the metal centres and organic ligands in the MOF can be readily altered according to different requirements, allowing tuning of its physical/chemical properties. Furthermore, the organic ligands can carry a variety of reactive functional groups [17], which can also enhance the designability (Figure 1.1).

These advantages have led to intense research on the fluorescent properties and sensing characteristics of MOFs [11, 18-20]. In particular, the highly adjustable and porous MOF structure allows it to easily have one or more fluorescence sources, providing a broad designable platform for fluorescence based sensing and optoelectronic applications. As shown in Figure 2.1, metal centres, organic linkers, charge transfer, and guests can all act as fluorescent sources, which can be further designed and modified to enable fluorescence sensing. Meanwhile, the high specific surface area and the predictable pore geometry and chemical affinity (i.e. altering its polarizability, hydrophilicity/phobicity and pore size) provide a structural basis for achieving high sensitivity and high selectivity that are central to fluorescence sensing. It is worth noting that the stability of many MOFs has been criticised and

that some MOFs are expensive and difficult to synthesise, which requires additional attention in applications.

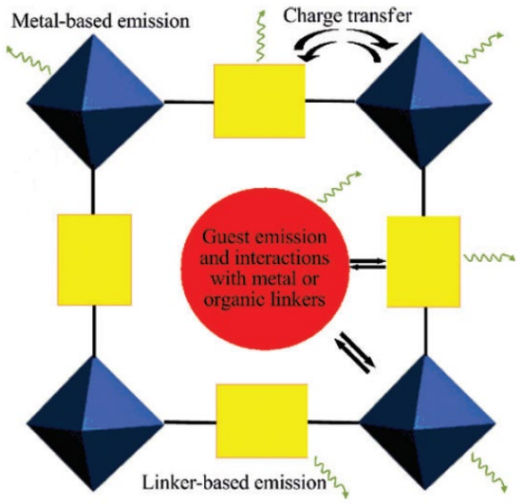

Figure 2.1. Representation of different emission pathways in a MOF, wherein metal centres (blue octahedra) are linked by organic linkers (yellow rectangles) with an encapsulated guest residing in the pore (denoted by red circle). Reproduced with permission from ref [11]. Copyright 2009 Royal Society of Chemistry.

Compared with other forms of MOF fluorescence, the idea of combining a luminescent 'guest' and a MOF 'host' as a composite system (guest@MOF) to yield tuneable fluorescence and to design sensors has become increasingly attractive over the last five years. The reasons are as follows:

i. Although adding the guest can cause a reduction in porosity and possibly in crystallinity, the guest@MOF system basically retains the above-mentioned advantages brought by the MOF structure [18].

ii. The porosity of MOF can disperse/separate the nanoconfined guest molecules, helping to overcome the ACQ effect, thus, enabling them to emit

light in the solid-state form [21], which will greatly widen their applications in fluorescence sensing. In addition, the large number of commercially available fluorophores also offers plenty of promising candidates to prepare different combinations of guest@MOF systems.

iii. Interaction between the guest and MOF may occur and result in many novel emergent properties. Some guests themselves contain weak forces, such as π-π stacking. When this kind of guest is introduced into a MOF, these weak forces may interact with the strong forces attributed to the MOF host (i.e. the strong coordination bonds between the linker and metal ions) [18] and produce more sensing behaviour.

iv. It is typically straightforward to synthesise the guest@MOF system. Specific methods are described in Section 2.3. In short, the synthesis of the guest@MOF system generally is relatively fast (compared with modifying linker routes) and does not require complex experimental steps/instruments, which is promising for future scaling up and commercialisation.

2.2 Structures

It is commonly considered that when the guest is embedded/encapsulated within the MOF crystals, the guest and MOF form a ‘guest@MOF’ system. Depending on the relative dimension of the guest and the size of a single MOF pore, the structure can be further divided into the ‘normal’ and ‘core-shell’ types (Figure 2.2). In the former, the guest size is smaller than the pores (Figure 2.2a), while in the latter, the guest is larger than the pores (Figure 2.2b).

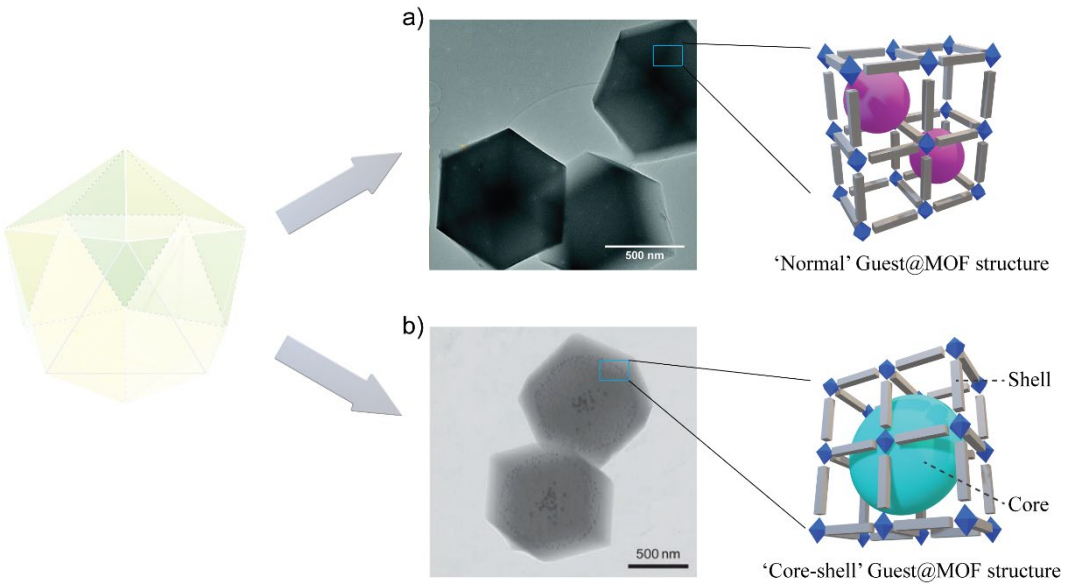

Figure 2.2. Scheme of the 'normal' and 'core-shell' type guest@MOF structure. (a) The 'normal' guest@MOF structure where the guest is smaller than the MOF pore. Transmission electron microscopy (TEM) could not observe the guest due to its small dimension. Reproduced with permission from ref [22]. Copyright 2016 Royal Society of Chemistry (b) The 'core-shell' guest@MOF structure, and TEM could be used to observe the relatively large guest aggregates. Reproduced with permission from ref [23]. Copyright 2012 Nature Publishing Group.

The structure of guest@MOF systems has an important effect on their fluorescent properties. For example, if the guest adheres to the surface of MOF crystals instead of being encapsulated or embedded, the MOF cannot effectively apply the caging effect, leading to relatively poor fluorescence and absence of any sensing behaviour [24, 25]. ZnQ@OX-1 [ZnQ = Zinc bis-(8-hydroxyquinoline), OX-1 = $(TEA)_2[Zn_3bdc_4]$·solvent, TEA = triethylamine, bdc = benzenedicarboxylate, solvent = N,N-dimethylformamide (DMF) or N,N-dimethylacetamide (DMA)] developed by Chaudhari *et al.* [26] can show the fluorescence sensing of acetone vapour, but the system will only display green or blue emission without any sensing properties if the ZnQ guest is located outside the

OX-1 crystals. It is worth noting that the influence of ‘normal’ and ‘core-shell’ structure on the sensing properties has been poorly studied and this aspect needs further discussion and more systematic research.

2.3 Synthetic Protocols

Synthesis is known to play a significantly important role in controlling the structure and properties of framework materials. At present, the synthetic protocols of guest@MOF systems can be roughly divided into two categories: One is called the post-synthesis method (Figure 2.3a), and the other is the in-situ synthesis method (Figure 2.3b). The following will analyse the basic concepts, applicability, advantages, and disadvantages of these two methods and give some representative examples to understand better their basic features and applications.

2.3.1 Post-synthesis

Simply put, the post-synthesis method is to set the MOF crystals into an environment filled with guest monomers or precursors and let the guest slowly enter the pores/channels of the MOF host. This method can give full consideration to the stability of the guests for avoiding the guest being destroyed or degraded during the MOF synthesis process [27]. Nevertheless, the size of the guest needs to be smaller than the size of the MOF window aperture to make sure the guest can theoretically enter the MOF pore/channel. Also, it is evident that this kind of absorption process

may lead to a non-uniform distribution of the guest in the MOF, resulting in a lower concentration of inward guests within the bulk crystal [28].

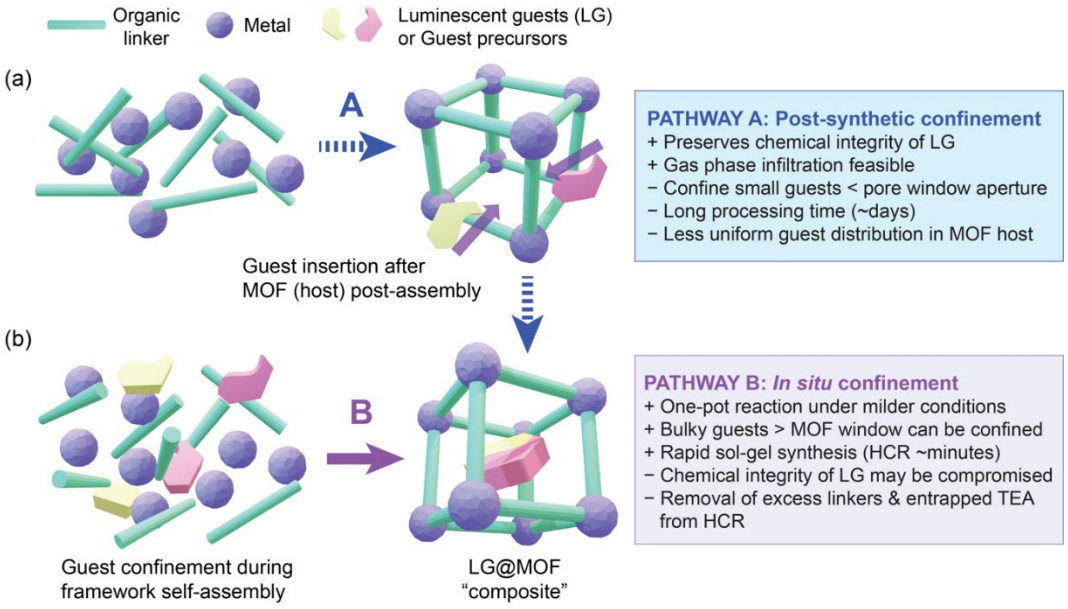

Figure 2.3. Synthetic protocols of LG@MOF systems. (a) Post-synthesis and (b) in-situ methods. The text boxes summarise the advantages and disadvantages of the two methods. (HCR = high-concentration reaction).

Currently, the commonly used post-synthesis methods are liquid impregnation and gas-phase infiltration. The former involves immersing the MOF crystals into a high-concentration guest solution, in which the ion exchange and/or diffusion effect helps MOF absorb the guest to form the guest@MOF system. For example, Yan *et al.* [29] prepared a luminescent guest@MOF system by directly adding MOF crystals [IRMOF-8, $Zn_4O(O_2C\text{-}2,6\text{-napthalene-}CO_2)_3$] to a DCM-DMF solution [DCM = 4-(dicyanomethylene)-2-methyl-6-(4-dimethylaminostyryl)-4*H*-pyran] under ultrasonication for 1 hour. The formed DCM@IRMOF-8

showed a blue/red two-colour emission which was sensitive to volatile organic solvents.

Gas-phase infiltration, the other commonly used post-synthesis method, uses a high-temperature and low-pressure environment to vaporise the guest and then allows the MOF crystals to capture it. The principle is similar to liquid impregnation, but the required equipment and experimental conditions are more complicated [30]. The significant advantage of gas-phase infiltration is that no solvent is needed, which helps to increase the guest loading and prevents the MOF from absorbing excess solvent, thereby affecting the fluorescence. Tu *et al.* [31] applied this method to synthesise the ANT@ZIF-8 composite with yellow-to-purple photo-switchable emission [ANT = anthracene, ZIF-8 = $Zn(mIm)_2$, mIm = 2-methylimidazolate]. Solution ^1H nuclear magnetic resonance (NMR) spectroscopy and thermogravimetric analysis (TGA) results suggest an average of 3.6 ANT molecules per ZIF-8 MOF pore, which proves that gas-phase infiltration may achieve a high guest loading due to the removal of solvent effects [31].

2.3.2 In-Situ Synthesis

Unlike the post-synthesis method, the in-situ synthesis method involves the addition of the guest to the reactants prior to the formation of MOF crystals. In other words, this method can be thought of as mixing the guest molecules directly with the basic building blocks of MOFs (the metal ions/clusters and organic linkers). In this case, many guests with dimensions larger than the MOF window can be

encapsulated into the MOF pores. Some guests whose size is relatively larger than the MOF pores can also be embedded using this method to form a core-shell guest@MOF system (Figure 2.2). Overall, in-situ synthesis is relatively more straightforward and can yield a better guest distribution confined in the bulk crystal, but more attention should be paid to the stability of guests during the synthesis process.

The most commonly used in-situ synthesis is *via* one-pot reactions, in which the guests, metals, and organic linkers are directly combined in solution within the same vessel, and then molecular self-assembly occurs to complete the reaction. Ambient reaction conditions are usually sufficient for many one-pot reactions to happen. For instance, Asadi *et al.* [32] used one-pot synthesis under room temperature to prepare a core-shell structure of a guest@MOF system: PEG-ZnS QD@ZIF-67 [PEG-ZnS QD = polyethylene glycol-capped ZnS quantum dots, ZIF-67 = $Co(mIm)_2$]. However, certain one-pot reactions require high temperatures. For example, a series of luminescent guests@NKU-111 composites [NKU-111 = $Cd_3(tpt)_2(PTA)_3(H_2O)_3 \cdot 2H_2O$, tpt = 2,4,6-tri(4-pyridinyl)-1,3,5-triazine, PTA = p-phthalic acid] prepared by Zhang *et al.* [33] was synthesised at 100 °C *via* one-pot reaction.

Another in-situ synthesis method is the recently developed HCR approach. The experimental procedures are illustrated in Figure 2.4. Due to the small amount of solvent used and the addition of deprotonating agents (e.g. TEA), the HCR speed is rapid (~minutes or less), where the guest@MOF structures form immediately upon solution combination, resulting in crystals with a much smaller size (usually

~10−100 nm). For example, the Fluorescein@ZIF-8 [24] and Gaq_3@ZIF-8 [Gaq_3 = gallium(III) tris(8-hydroxyquinolinato)] [34] systems prepared by HCR show a crystal size of 50 − 100 nm and the reaction is completed instantly. In comparison, the normal one-pot reaction of ZIF-8 synthesis typically takes 24 hours, and results in crystal sizes of about 1 − 5 μm [35]. Not coincidentally, the RhB@ZIF-71 system [ZIF-71 = $Zn(dcIm)_2$, dcIm = 4,5-dichloroimidazole, RhB = rhodamine B] obtained *via* HCR is also generated instantaneously with a crystal size of 50 − 150 nm, whereas the one-pot RhB@ZIF-71 requires 24 hours and has a size of about 800 nm [25, 36].

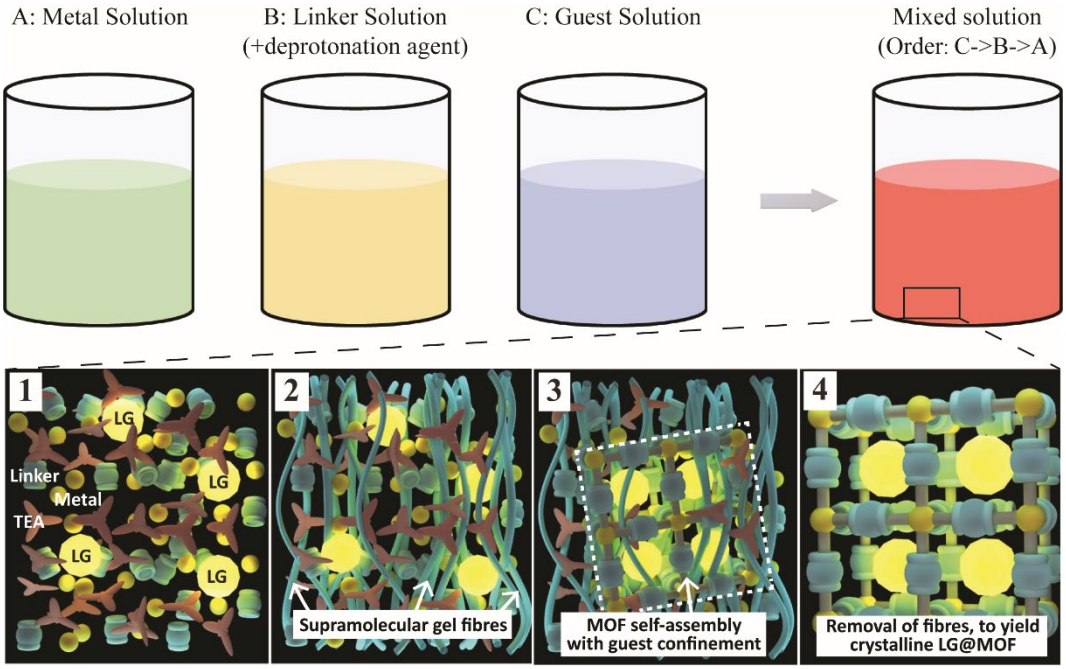

Figure 2.4. Schematic illustrating the experimental procedures and the sequential stages of HCR for synthesising guest@MOF systems. 1-4 self-assembly processes will be completed instantly during the experiment. Reproduced from ref [26]. Copyright 2017 John Wiley and Sons.

2.4 Types of Luminescent Guest for Confinement in MOF

Due to the tunability and orderliness of the MOF structure, the types of guest that can be used in the guest@MOF systems are also diverse, including but not limited to organic dyes, metal ions/complexes/nanoclusters, quantum dots, and inorganic-organic perovskites (Figure 2.5). As mentioned in Section 2.1, for almost all types of guest, MOF can help them overcome their drawbacks of being unsuitable for fluorescence sensing and may even bestow the guest@MOF system with new sensing properties not present in the guest or host considered in isolation.

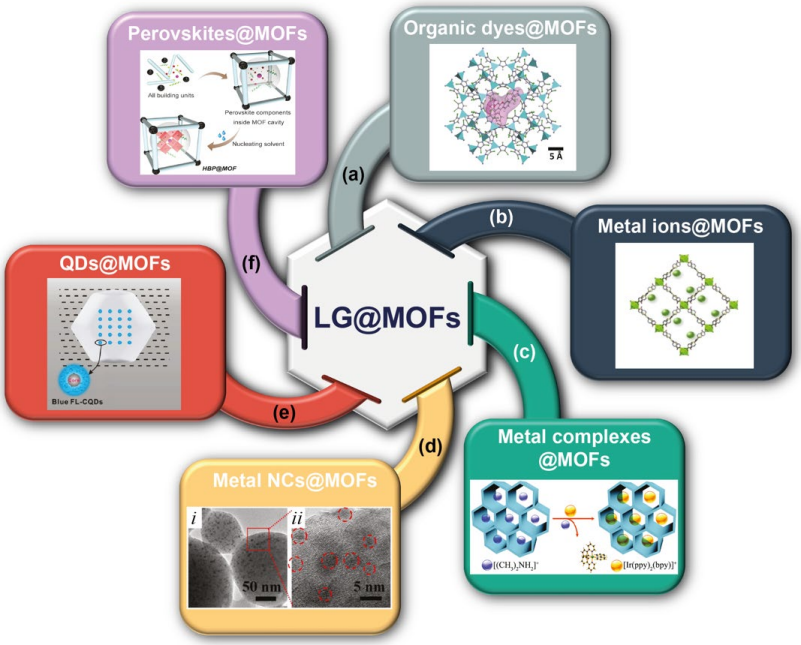

Figure 2.5. Major types of luminescent guest (LG) that have been encapsulated inside the MOF host to yield the LG@MOF composite systems: (a) organic dyes, figure inset adapted from ref [25]. Copyright 2020 American Chemical Society. (b) metal ions, figure inset adapted with permission from ref [37]. Copyright 2019 Elsevier. (c) metal complexes, figure inset adapted from ref [38]. Copyright 2017 Royal Society of Chemistry. (d) metal nanoclusters (NCs), figure inset adapted from ref [39]. Copyright 2018 American Chemical Society. (e) quantum dots (QDs), figure inset adapted from ref [40]. Copyright 2014 American Chemical Society. and (f) hybrid perovskites, figure inset adapted from ref [41]. Copyright 2019 American Chemical Society.

For example, the multi-characteristic emission of lanthanide (Ln) ions makes them suitable for use as fluorescence sensors. However, the luminescent mechanism of Ln ions relies on the theoretically forbidden f-f transitions, resulting in low quantum yields (QYs) (usually 2~13%) [12]. Macroscopically, this will cause the fluorescence signal of Ln ions to be very weak, which cannot meet the requirements for effective sensing. Within the Ln@MOF systems, an energy transfer process known as the antenna effect (i.e. the excitation occurs at a ligand and then transfers energy to the Ln ion) can be established to enhance QY and improve its sensing performance. On this basis, Ji *et al.* [37] developed a Tb@Zn-MOF (Tb = Terbium) composite which shows an energy transfer between the linker and the Tb ions. When exposed to aspartic acid, the energy transfer would be enhanced, giving a stronger fluorescence signal.

2.5 Applications of Guest@MOF for Fluorescent Sensing

With their unique structure and performance characteristics, luminescent guest@MOF systems can be used in many sensing fields. One of the sensing areas is to detect physical parameters, such as temperature [42] and stress [43]. Compared to traditional physical sensing devices, guest@MOF sensors enable fast, easy and precise measurement at sub-micron levels, and allow to measure single point, multiple points, or whole objects. For example, Liu *et al.* [44] designed a new $CsPbBr_3$@Ln-MOF powder, which showed turn-on plus self-calibrating features (Figure 2.6), giving rise to potential applications in non-invasive thermometry. Due to the powder form, it can theoretically be made into any shape to measure the

temperature of any irregularly shaped or microscopic objects. In contrast, conventional mercury thermometers have a slow response time and must contact the object, while other non-contact temperature measurement techniques, such as infrared thermal imaging, have low resolution and are greatly affected by the environment. The temperature sensor made from the guest@MOF not only overcomes the above disadvantages but can also measure the temperature inside the living body cells or the surface temperature distribution [45].

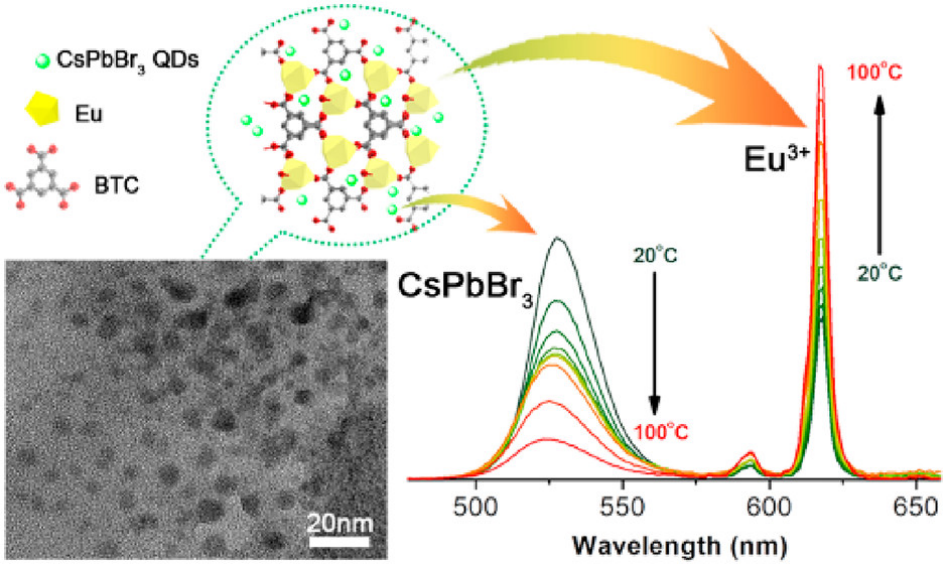

Figure 2.6. An example showing the use of guest@MOF materials for temperature sensing. Self-calibrating is to introduce additional referent emission peaks into the system, thereby reducing the interference and improving the sensitivity. Reproduced from ref [44]. Copyright 2020 American Chemical Society.

Another area of fluorescent sensing MOFs is to detect various chemical information like volatile organic compounds (VOCs) [25, 46], toxic chemicals [47], gases [26], cations [32, 48], anions [49], and pH [26, 50]. Due to its porous structure, the guest@MOF material can absorb analytes/chemicals into the nanoscale pores

[51], which will dramatically increase the sensitivity. Furthermore, because of its tuneable pore size and properties, specific guest@MOF sensors can be expediently designed for different analytes and to tailor to different environments. For example, Chen *et al.* [52] developed a Rh6G@MOF system (Rh6G = Rhodamine 6G) which has two emission peaks from the tpt ligand (363 nm) and Rh6G guest (580 nm), respectively. When exposed to 2,4,6-trinitrophenol (TNP, a toxic pollutant and highly explosive molecule), the luminescence from the ligand would be significantly quenched, whereas the Rh6G was only slightly affected. By observing the different changing ratios, the TNP molecules were detected effectively (Figure 2.7a). In addition, the authors also found that the Rh6G@MOF could selectively detect TNP among many non- and most nitroaromatic compounds (Figure 2.7b) due to the specific interaction between the acidic TNP molecule and MOF.

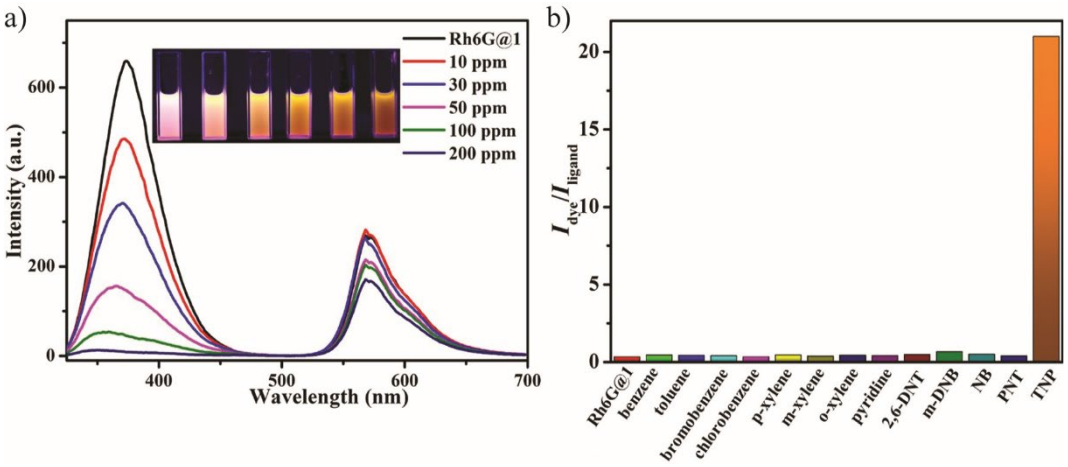

Figure 2.7. An example showing the use of guest@MOF materials for VOC sensing: (a) Emission spectra for Rh6G@MOF at different concentrations of TNP, (b) the peak-height ratio of dye to ligand after addition of 200 ppm of various analytes. Reproduced from ref [52]. Copyright 2017 American Chemical Society.

3

Aggregates@MOF

3.1 Background and Motivations

Through the previous chapters, it is understood that guest@MOF facilitates the design and preparation of fluorescence sensors. However, most current studies have only focussed on the interaction between the guest and MOF (e.g., only using the energy transfer between the guest and MOF to generate sensing behaviour) [11, 12, 20, 51]. The interactions between the guests themselves within the guest@MOF systems are still poorly understood. Furthermore, most papers avoid discussing the concentration/configuration of guests within MOF pores or structures. These shortcomings limit the further development of the guest@MOF systems for practical use.

For example, Tu *et al.* developed an ANT@ZIF-8 system with an excellent photochromic effect [31]. After 30 minutes of UV irradiation (360 nm, UV = ultraviolet), the peak emission wavelength of the ANT@ZIF-8 material changed from 550 nm to approximately 415 nm (Figure 3.1). In this study, the authors used solution ^{1}H NMR and TGA techniques to investigate the quantity of the ANTs in the ZIF-8 pores, which is innovative in the guest@MOF research field. Knowing the number of ANT molecules caged in a single ZIF-8 pore, the authors proposed an in-depth mechanism whereby 2 of the 4 ANT molecules would photodimerize

after UV irradiation producing the unique photochromic response. It is evident from this research that studying the number/configuration of the guests is of great significance for designing more advanced sensing materials. However, for the ANT@ZIF-8 system, the emission from the ANT molecules is in excimer form when not irradiated by UV, which means the ANT is not in an aggregate state, and there is no strong interaction between the ANT molecules. Thus, the guest interaction within guest@MOF systems deserves a deeper investigation.

In addition, the practical engineering application of guest@MOF systems may also be affected by their inferior stability [36]. Many guest@MOF systems are unstable and will lose their fluorescence outside the laboratory. For example, oxygen atoms in moisture may damage the coordination bonds of MOFs and UV illumination in the environment can also gradually deteriorate the fluorescence of the guests. Nevertheless, the research on improving long-term stability has not attracted enough attention.

In order to study the influence of the interaction between the guests themselves on the resultant fluorescence properties, in Paper I the author demonstrated the concept of guest aggregates encapsulated in the MOF pores. Theoretically, through first simulations, it is feasible to introduce guest aggregates into MOF and manage the number of guests within one MOF pore by selecting the appropriate guest size. Photophysical characterisation was employed to comprehensively probe the mechanism by identifying the guests' configuration, microstructure, and interaction. To improve the overall material stability, the author

showed that guest@MOF could be combined with robust commercial polymers to meet the requirements of engineering applications.

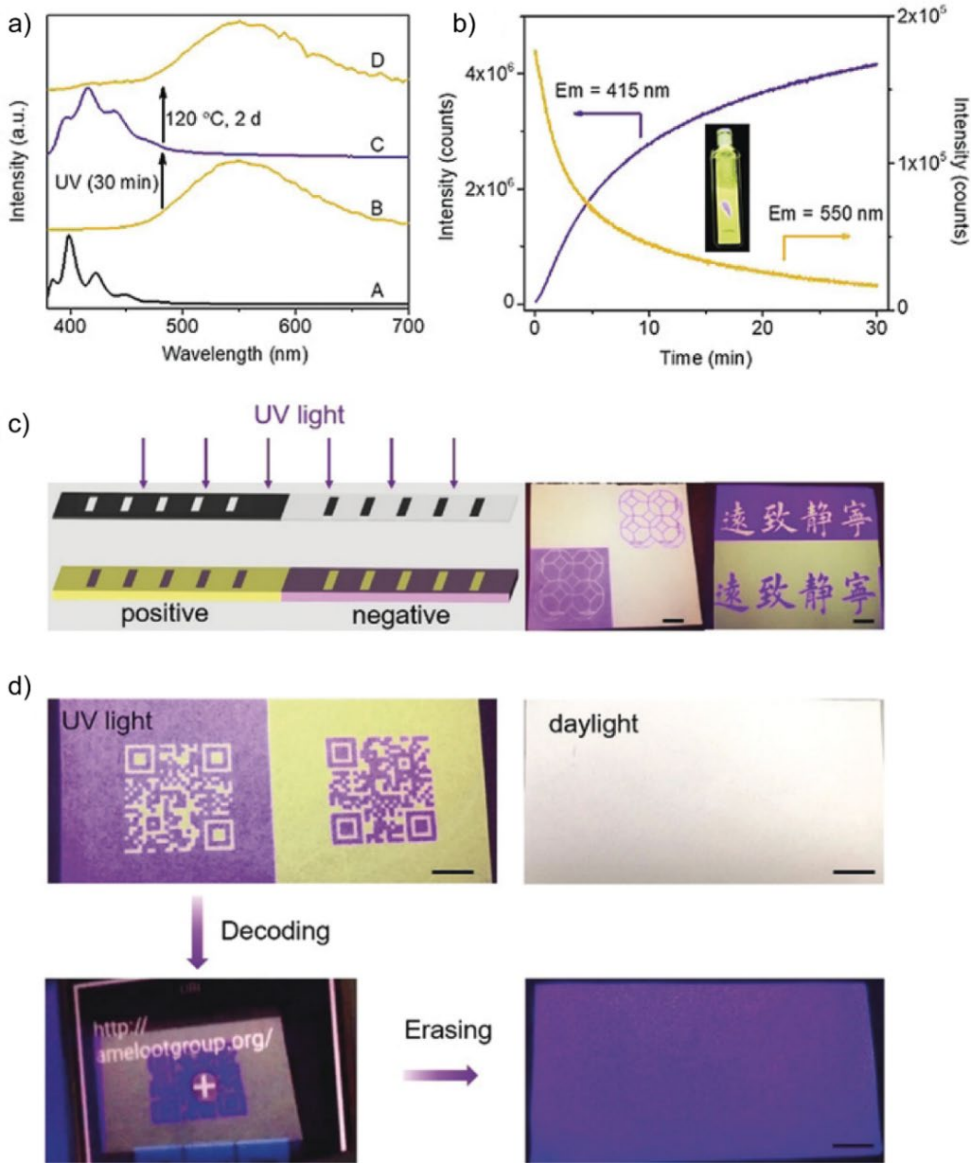

Figure 3.1. (a) Fluorescence emission spectra of a 1 mM ANT methanol solution (A), ANT@ZIF-8 (B), UV-irradiated ANT@ZIF-8 (C), and thermally treated UV-irradiated ANT@ZIF-8 (D). (b) In situ monitoring of the fluorescence emission intensity (415 nm and 550 nm) upon continuous excitation at λ=360 nm. (c) Schematic representation of photopatterning on ANT@ZIF-8 based paper in a combination of positive and negative ways (left) and optical images obtained by photopatterning (right, bar: 2 cm). (d) Top: Images of photopatterned QR codes under UV light and daylight. Bottom: Decoding of QR codes with a smartphone (left) and erasing the codes after encoding (right). Scale bar: 1 cm. Reproduced from ref [31]. Copyright 2019 John Wiley and Sons.

3.2 Brief Summary of Paper I

Paper I reported the novel RhB@ZIF-71 system as the object to discuss the effect of guest interaction on fluorescence properties. To avoid introducing too many complicated interactions at the same time, it is considered that encapsulating a bimolecular aggregate into a MOF pore is beneficial to simplify but still allow an in-depth study of the fluorescence sensing mechanism. Furthermore, to ensure the system can be fabricated, the MOF needs to have pores large enough to accommodate the guest dimer but not to interact with the guest dimer strongly, as the strong interaction is likely to prevent the intermolecular interaction within the aggregates to yield a sensing response. In addition, the produced aggregates@MOF system should preferably be easy to synthesise and scalable so that it has real application potential.

Based on the above requirements, the author chose RhB and ZIF-71 as the guest and the host, respectively. One of the reasons is related to the molecular dimensions. The molecular size of RhB is 16.19 × 12.83 × 6.97 Å (including the van der Waals surface, calculated using Discovery Studio), and the minimum/maximum distance inside the ZIF-71 pore is 16.58/22.59 Å (the minimum distance refers to the diameter of the largest sphere that will fit into the pore without contacting the framework atoms; the maximum distance is the largest distance of two atoms within the pore through the pore central area). In that situation, an RhB dimer is possible to reside in one ZIF-71 pore due to its π-conjugated planar structure. TGA characterisation supported this hypothesis, the analysis of which is shown below.

To calculate the number of RhB inside the ZIF-71 pores, the mass percentage of ZIF-71 and RhB was first estimated corresponding to their mass loss in the TGA curves (Fig. 2b in Paper I). In the case of RhB_I@ZIF-71, the loss of mass associated with ZIF-71 and RhB was determined to be 93.5% and 7.5%, respectively. For RhB_{II}@ZIF-71 and RhB_{III}@ZIF-71 composites, the mass loss of ZIF-71 was 90.8% and 83.4%, respectively, while for RhB it was 9.2% and 16.6%, respectively. From those values, the author has calculated the number of moles of RhB per moles of ZIF-71 by applying the following equations:

$$n = \frac{m}{M} \tag{1}$$

where *n* stands for the number of moles, *m* is the mass, and *M* is the molecular weight. From equation (1) it is possible to estimate the ratio between the moles of ZIF-71 and RhB:

$$\frac{n_{ZIF-71}}{n_{RhB}} = \frac{\frac{m_{ZIF-71}}{M_{ZIF-71}}}{\frac{m_{RhB}}{M_{RhB}}} = \frac{m_{ZIF-71}}{m_{RhB}} \times \frac{M_{RhB}}{M_{ZIF-71}} \tag{2}$$

Knowing that the chemical formula of ZIF-71 is $[Zn_2C_{12}H_4Cl_8N_8]$, the global chemical formula of RhB@ZIF-71 is given by:

(I) RhB_I@ZIF-71:

$$\frac{n_{ZIF-71}}{n_{RhB}} = \frac{93.5}{7.5} \times \frac{479}{674} = \frac{1}{0.098}$$

$$\mathbf{[Zn_2C_{12}H_4Cl_8N_8] \cdot (RhB)_{0.098}}$$

(II) RhB_{II}@ZIF-71:

$$\frac{n_{ZIF-71}}{n_{RhB}} = \frac{90.8}{9.2} \times \frac{479}{674} = \frac{1}{0.143}$$

$$\mathbf{[Zn_2C_{12}H_4Cl_8N_8] \cdot (RhB)_{0.143}}$$

(III) RhB_{II}@ZIF-71:

$$\frac{n_{ZIF-71}}{n_{RhB}} = \frac{83.4}{16.6} \times \frac{479}{674} = \frac{1}{0.280}$$

$$\mathbf{[Zn_2C_{12}H_4Cl_8N_8] \cdot (RhB)_{0.280}}$$

Once the amount of RhB per two atoms of Zn (i.e. Zn_2) has been calculated, and by knowing that a single pore of ZIF-71 contains 24 atoms of Zn, the mean number of RhB molecules per pore in each material can be estimated as follows:

(I) RhB_I@ZIF-71 → 0.098 × 12 = 1.2 RhB molecules per pore

(II) RhB_{II}@ZIF-71 → 0.143 × 12 = 1.7 RhB molecules per pore

(II) RhB_{III}@ZIF-71 → 0.280 × 12 = 3.4 RhB molecules per pore

Because of the spatial constraint of the ZIF-71 pore, only a maximum of two RhB guest molecules could occupy a pore volume. On this basis, it was reasoned that (I) and (II) are confined inside the pores of ZIF-71, whereas (III) has excess molecules that are adhering to the outer surfaces of the ZIF-71 crystals due to the excessive amount of RhB used in (III).

Powder X-ray diffraction (PXRD), Fourier transform infrared spectroscopy with attenuated total reflection (ATR-FTIR), TGA, and Raman vibrational spectroscopy experimental characterisation results further support the above analysis presented in Paper I. To give more intuitive evidence, a physically mixed sample of RhB + ZIF-71 was prepared, but it showed only a faint fluorescence under

UV irradiation in contrast to the highly luminescent RhB@ZIF-71 system (Figure 3.2), demonstrating that the RhB@ZIF-71 system indeed has successfully formed.

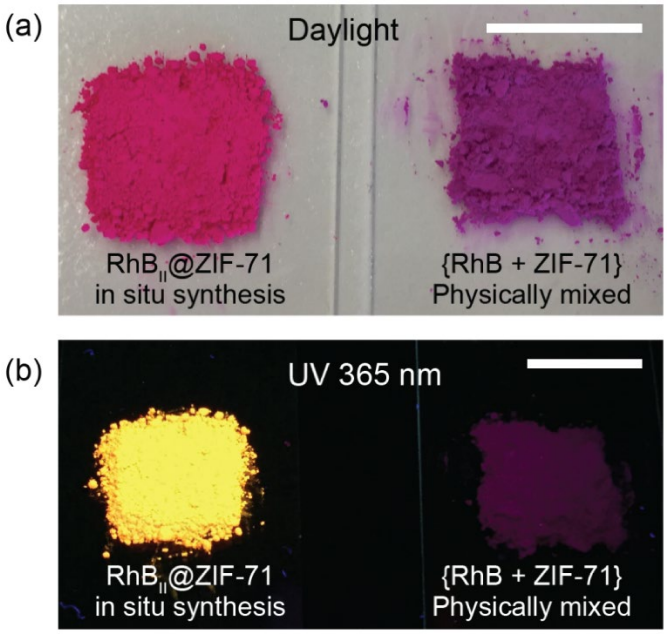

Figure 3.2. Comparing the sample colour and luminescence behaviour observed (a) under daylight and (b) in UV irradiation. Marked differences can be seen between the samples of RhB_{II}@ZIF-71 derived from in situ encapsulation synthesis (see method in Paper I), in contrast to the [RhB + ZIF-71] sample made by simple physical mixing or blending of the two constituents (in mortar and pestle by maintaining the same guest concentration as RhB_{II}@ZIF-71). The physically mixed 'composite' is not photoluminescent under UV irradiation due to the quenching of RhB guests aggregating on the outer surfaces of the ZIF-71 crystals. Conversely, it is clear that the RhB guest molecules confined in the ZIF-71 pores are well isolated and thus highly luminescent under UV excitation. Scale bar: 12.5 mm.

Another reason the author chose RhB@ZIF-71 is that there is no strong interaction between RhB and ZIF-71. Although the ligand metal charge transfer (LMCT, Figure 3.3) process of ZIF-71 was disrupted after the formation of RhB@ZIF-71 system (Fig. 3 in Paper I), the fluorescent properties of RhB@ZIF-71 are still comparable to pure RhB aggregates (Figure 3.4). Combining the excitation-

emission spectra of RhB@ZIF-71 (Fig. 3 in Paper I) and Figure 3.4, it is obvious that the RhB aggregates are successfully introduced, and their emission is not affected by the RhB-MOF interaction. Furthermore, through the in-depth analysis of the fluorescence spectra and emission lifetime (Fig. 3 in Paper I), three RhB states existing in the RhB@ZIF-71 system are identified: monomers, H-aggregates (head-to-head), and J-aggregates (head-to-tail), as shown in the schematic diagram in Paper I.

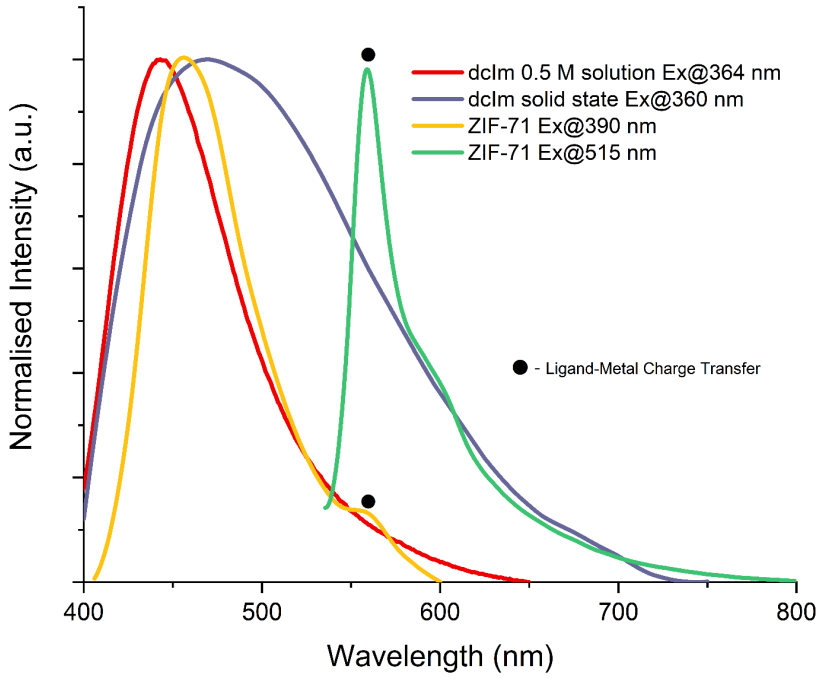

Figure 3.3. Normalised emission spectra of the dcIm linker in methanol solution (0.5 M) and in the solid state, compared to that of the pristine ZIF-71 in solid state, excited at 390 nm or 515 nm. While the LMCT emission peak disappeared after the formation of RhB@ZIF-71 system (related to Fig. 3b in Paper I).

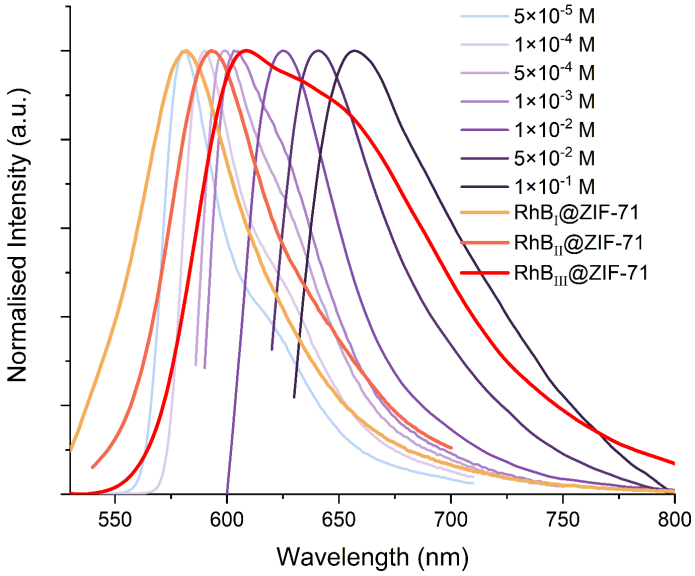

Figure 3.4. Normalised emission spectra of RhB in MeOH solution (ex@515 nm) of different concentrations, and $RhB_{I/II/III}$@ZIF-71 powders in the solid state.

After confirming the structure and property of pristine RhB@ZIF-71 powders are as expected, the sensing performance and mechanism are being investigated in Paper I. In short, it is due to the introduction of aggregates that the whole system can realise multi-response sensing for mechanical stress, temperature, and different VOCs. In principle, H-aggregates, J-aggregates, and monomers have different sizes and will receive different caging effects offered by the MOF host structure, resulting in different sensing responses. In addition, the ZIF family structures to which ZIF-71 belongs are tetrahedral metal ions bridged by imidazolate units and their phase changes under pressure were observed by *in situ* TEM [53]. The shear deformation they exhibited provides the structural basis for the mechanochromism shown in Paper I. It is worth mentioning that, along with the photophysical characterisations, a range of solvents with different sizes were selected to prove that J-aggregates are subject to a stronger caging effect (Figure 3.5). Because the pores

encapsulating larger J-aggregates has less room to accommodate additional solvents, this effect gives the relatively more red-shifted emission observed in the bulkier solvents such as IPA.

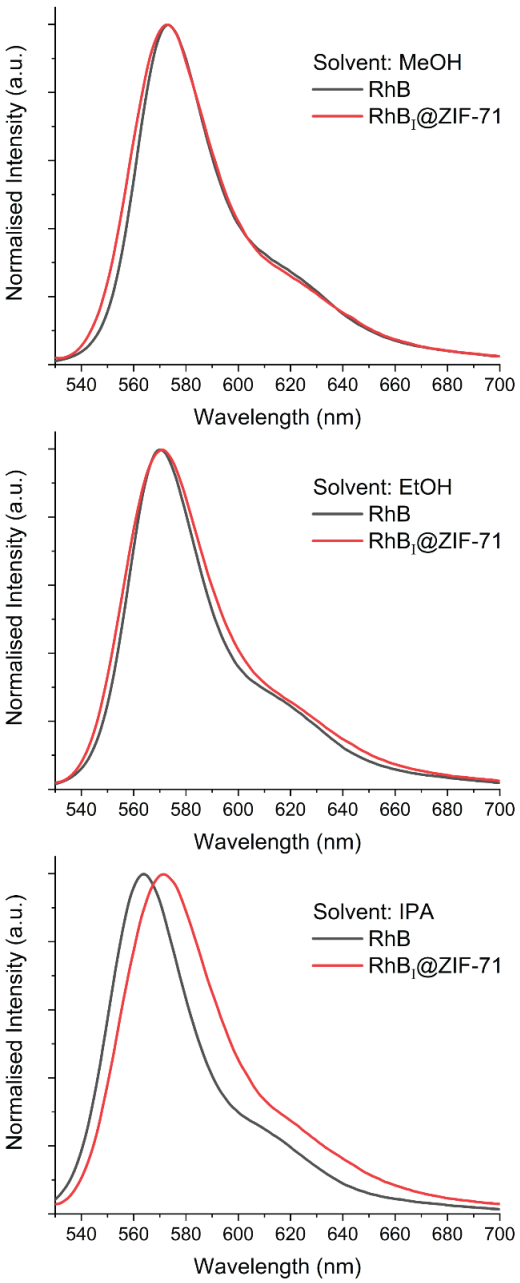

Figure 3.5. Comparison of the emission of RhB_I@ZIF-71 solutions and pure RhB in different solvents (7.5×10^{-6} M, ex@525 nm).

The aggregates-extended sensing mechanisms elucidated in this research, such as the transformation from H- to J-aggregates and J-aggregates being more stable at high temperatures, are the first exemplars shown in the guest@MOF field.

Moreover, RhB@ZIF-71 is also easy to be synthesised. The raw materials, zinc acetate, dcIm, and RhB, are readily available, and the synthesis method is the simple one-pot reaction that can be carried out at ambient conditions with a fast reaction time. Through the scanning electron microscopy (SEM) images of the crystals (Figure 3.6), it can be seen that after only 10 minutes, RhB@ZIF-71 crystals with well-defined facets have formed, showing potential for materials scaling up.

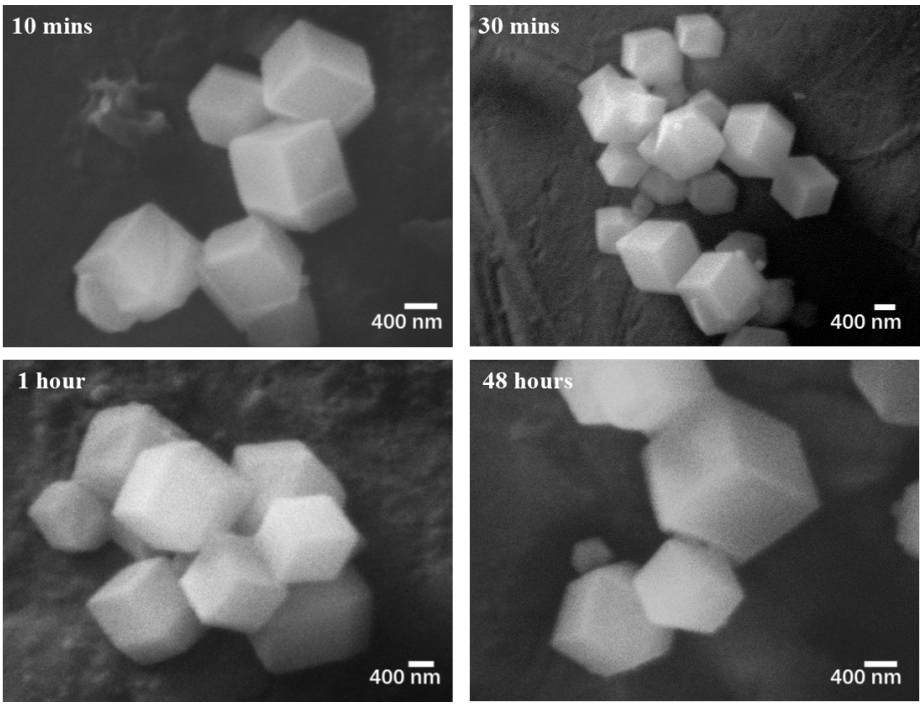

Figure 3.6. SEM images of RhB@ZIF-71 prepared using different reaction times, ranging from 10 mins to 48 hours.

3.3 Brief Summary of Paper II

According to Paper I, the sensing performance of RhB@ZIF-71 is promising, especially the multi-response sensing it exhibited: mechanochromism, thermochromism, and solvatochromism. Nevertheless, the stability of RhB@ZIF-71 should be improved further to afford practical engineering applications, though ZIF-71 itself is a reasonably stable material (due to its hydrophobicity) [54]. In addition, RhB@ZIF-71 is in a 'powder' form (i.e. fine polycrystalline crystals), which cannot satisfy a few high-precision applications like optical fibres. Therefore, it will be advantageous to combine the RhB@ZIF-71 with polymers and shape it into luminescent nanofibers (diameter < 1 μm) to address the above problems.

Paper II chose polyvinylidene difluoride (PVDF) as the polymer matrix because PVDF is non-luminescent, highly stable, hydrophobic, and easy to process (e.g., electrospinning). However, the crystal size of the normal RhB@ZIF-71 (~800 nm to 1 μm, Figure 3.6 and Fig. 1 in Paper I) is apparently way too large for preparing nanofibers. In this case, the polymer may not be able to thoroughly coat the individual crystals to give good protection. Therefore, the HCR method described in Section 2.3.2 was used to further reduce the RhB@ZIF-71 crystal size. Fig. 1 in Paper II shows that the typical size of the HCR RhB@ZIF-71 crystal is about 50 – 150 nm. As a comparison, it can be seen that combining HCR RhB@ZIF-71 with PVDF produces luminescent electrospun fibres containing uniformly dispersed RhB@ZIF-71 nanocrystals (Fig. 2 in Paper II), whereas the

fibres have many larger crystals and aggregates on the surface by using RhB@ZIF-71 obtained by the 'normal' non-HCR route (Figure 3.7).

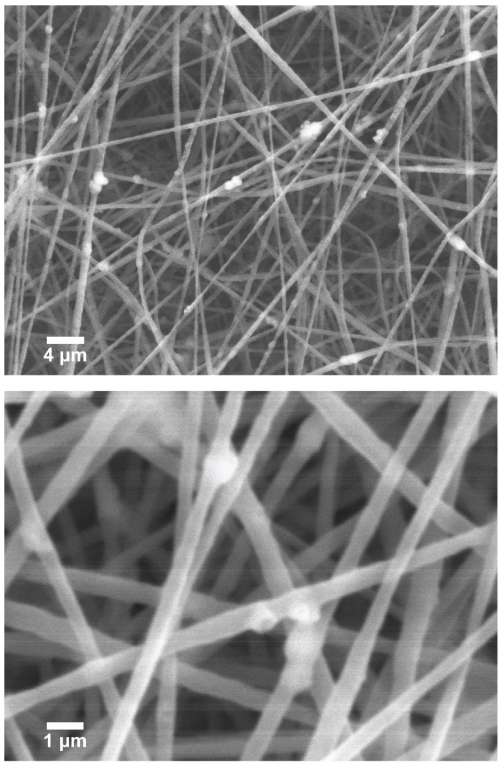

Figure 3.7. SEM images of electrospun PVDF fibres incorporating RhB@ZIF-71 micron-sized crystals obtained from the conventional method (non-HCR).

Then the HCR samples were subjected to PXRD, excitation-emission, UV-Vis (ultraviolet-visible), and ATR-FTIR characterisations to determine that the RhB@ZIF-71 nanocrystals were not decomposed during the electrospinning process. Moreover, because there is no strong interaction between RhB@ZIF-71 and PVDF, the fibres exhibit distinct RhB@ZIF-71 luminescence characteristics. These findings confirmed that the RhB@ZIF-71/PVDF composite material has formed as expected.

Particularly, RhB@ZIF-71/PVDF fibres possess many unique advantages. For example, the emission of such fibres is tuneable since the J-aggregates may have π-π interactions across the adjacent crystals (the reason is explained and illustrated in Paper II). The quantum yield of RhB@ZIF-71/PVDF fibres is very high, reaching 90%, which is much higher than other RhB-based composites reported to date (typically ~30-60%, as summarised in Table 3.1).

Table 3.1. The quantum yield of other RhB-based fluorescent materials reported in the literature compared with the results of the current study described in Paper II.

System	QY (%)	Ref
RhB/PVAc (PVAc = polyvinyl acetate); RhB/PMMA (PMMA = polymethyl methacrylate)	3.22 – 25.2	[55]
RhB@AuNP (NP = nanoparticle)	1	[56]
RhB/sol-gel silica	37.4	[57]
RhB solutions	30 – 66	[58]
RhB@ZIF-71/PVDF electrospun fibres 1wt%, 8μL/min	92 ± 0.5	This work (Paper II)

More importantly, the RhB@ZIF-71/PVDF fibre is thermochromic and thermally stable. During heating, its emission peak wavelength gradually red-shifted. Benefiting from the uniform distribution of nanocrystals and the high hydrophobicity of ZIF-71, even near the melting point of PVDF, the overall fluorescence performance of the material is still stable (Figure 3.8). The material also retains good RhB luminescence characteristics after multiple heating cycles (Figure 3.9).

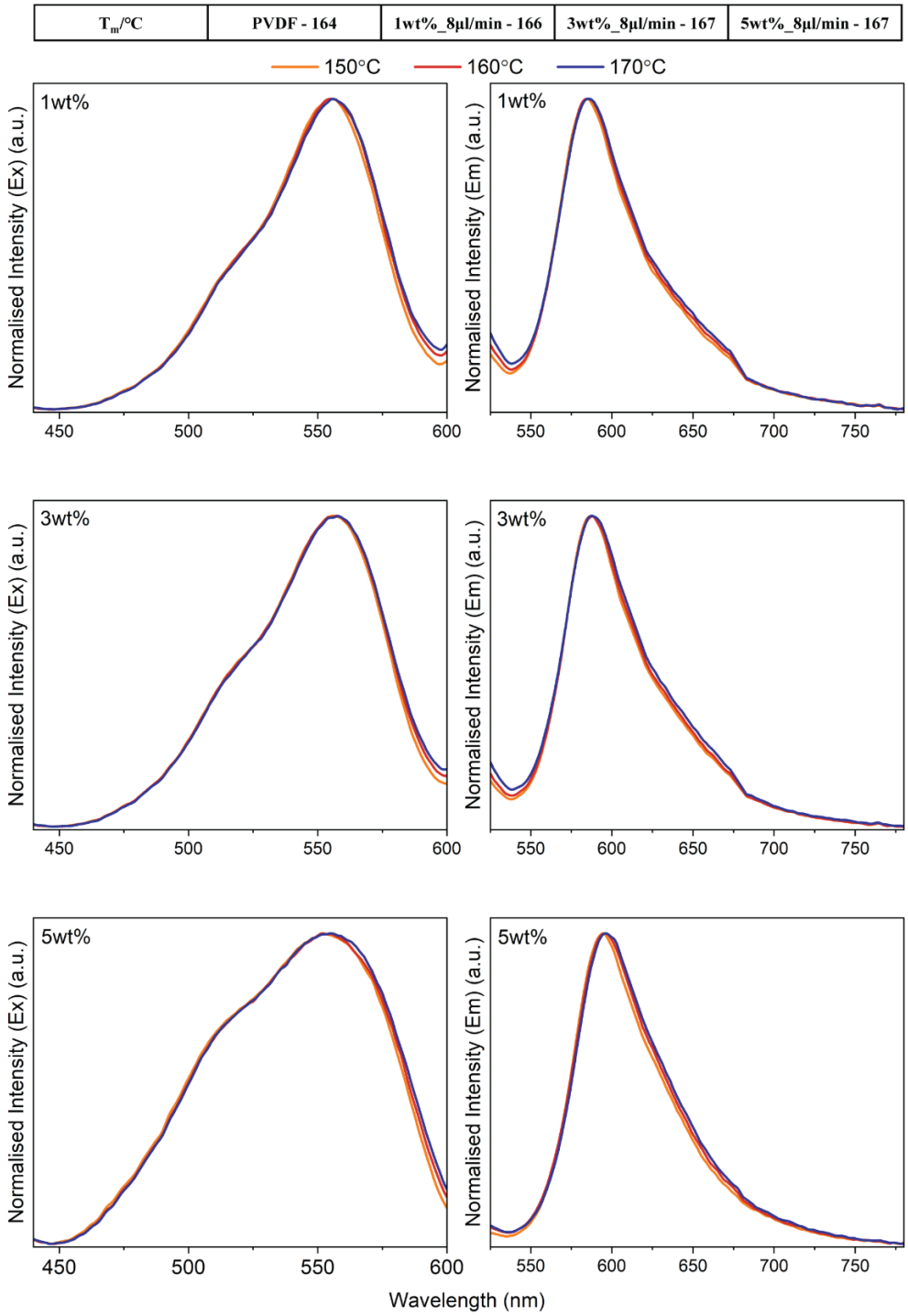

Figure 3.8. Characterisation of PVDF and RhB@ZIF-71/PVDF fibres at temperatures close to the melting temperature (T_m) of PVDF. T_m of PVDF and RhB@ZIF-71/PVDF fibres with different loading wt.%. Variation of the excitation and emission spectra during heat treatment of RhB@ZIF-71/PVDF fibres at temperatures close to the T_m of PVDF. The excitation spectra measured under em@620 nm. The emission spectra measured under ex@500 nm. All measurements were carried out in normal atmospheric conditions.

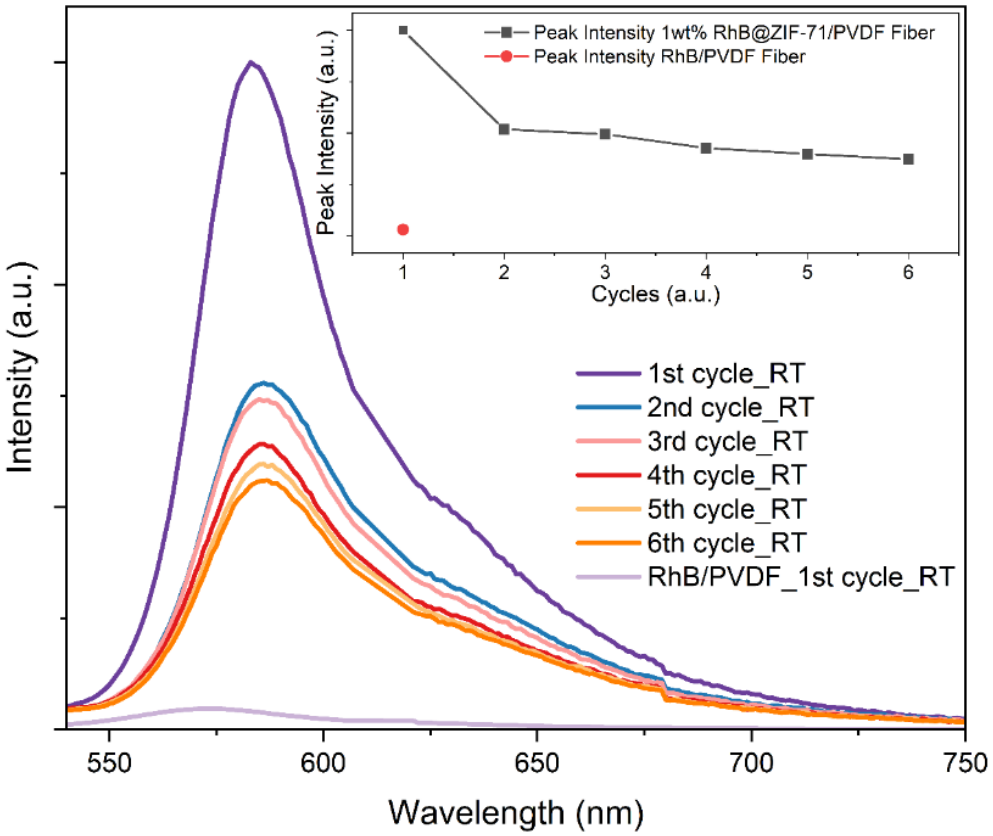

Figure 3.9. Emission property of RhB@ZIF-71/PVDF fibres after repeated heating measured under ex@500 nm. Emission spectra of RhB@ZIF-71/PVDF fibres (1 wt%, 8 μL/min) determined at room temperature (RT) after being subjected to repeated heating tests to 200 °C (denoted by the cycle number, RhB/PVDF fibre is shown for contrast). All measurements were carried out in normal atmospheric conditions.

As a comparison, RhB/PVDF fibres were prepared. For ensuring the amount of RhB in the fibres is the same, the absorbance of RhB@ZIF-71 and RhB in acetone solutions was measured. After certifying the absorbances were identical (Figure 3.10), the RhB/PVDF fibres were fabricated and they showed comparable luminescent properties to RhB@ZIF-71/PVDF fibres under ambient conditions (Figure 3.11). However, the thermal stability of RhB/PVDF fibres is poor. Its luminescence is greatly destroyed after heating (Fig. 6 in Paper II). Moreover, during the heating treatment, the emission peak wavelength of the RhB/PVDF

fibres was found to vary randomly (see Fig. 6F in Paper II), which is in stark contrast to the strong linear correlation exhibited by the RhB@ZIF-71/PVDF fibres (Fig. 6C in Paper II). The latter has promise for use in the engineering of non-invasive fluorescent thermometers. In summary, Paper II demonstrates the feasibility of preparing stable guest@MOF/polymer materials, such as electrospun fibres for photonic sensors and innovative luminescent applications.

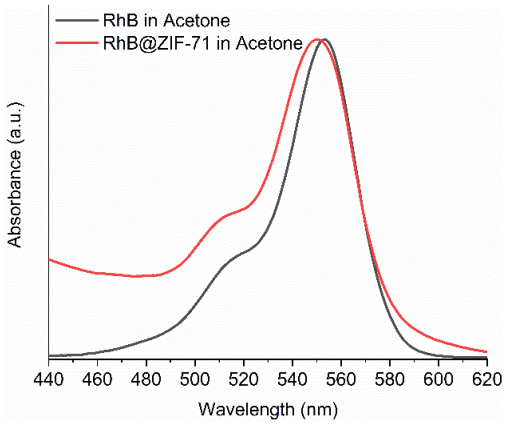

Figure 3.10. Absorption spectra of RhB and RhB@ZIF-71 in an acetone solution.

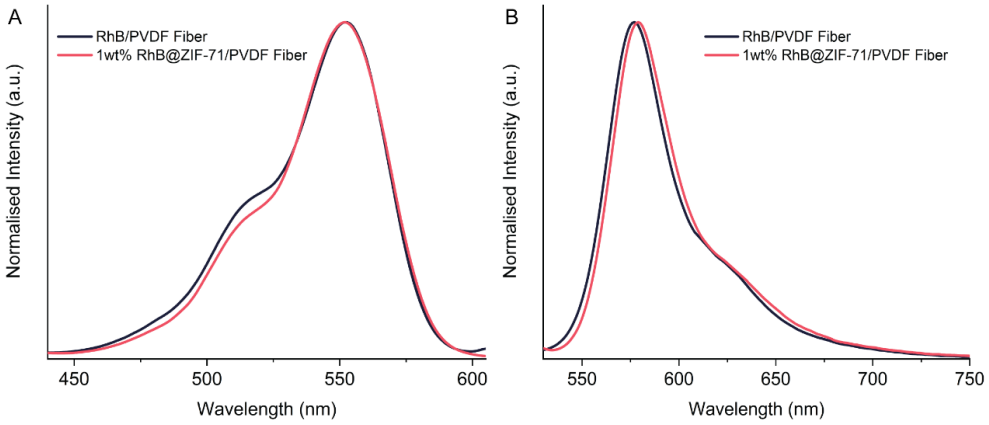

Figure 3.11. Excitation and emission spectra of RhB/PVDF fibres and RhB@ZIF-71/PVDF fibres.

4

AIE@MOF

4.1 Background and Motivations

It is clear from Section 2.4 that different kinds of guest may be used to prepare the guest@MOF systems. However, almost all of them can be classified as ACQ materials, and no report has yet considered introducing aggregation-induced emission (AIE) materials into guest@MOF systems.

AIE materials are a new fluorescence research area pioneered by Ben Zhong Tang in 2001 [59, 60]. The fluorescent property of this material is opposite to that of traditional ACQ materials: in the dispersed state, AIE materials have no emission, while in the solid state or high-concentrated state, AIE materials exhibit fluorescence. This kind of performance is closely related to the molecular structure of AIE materials. In general, the AIE molecules have a benzene-like structure that can rotate relatively freely (Figure 4.1a). When it is in a highly dispersed state, the intramolecular rotation is active, which will significantly increase the non-radiative decay and quench the fluorescence [61]. On the contrary, when it is in the solid state or high-concentrated state, AIE molecules will interact with each other, thus limiting the intramolecular rotation and improving the fluorescent properties (Figure 4.1b) [62].

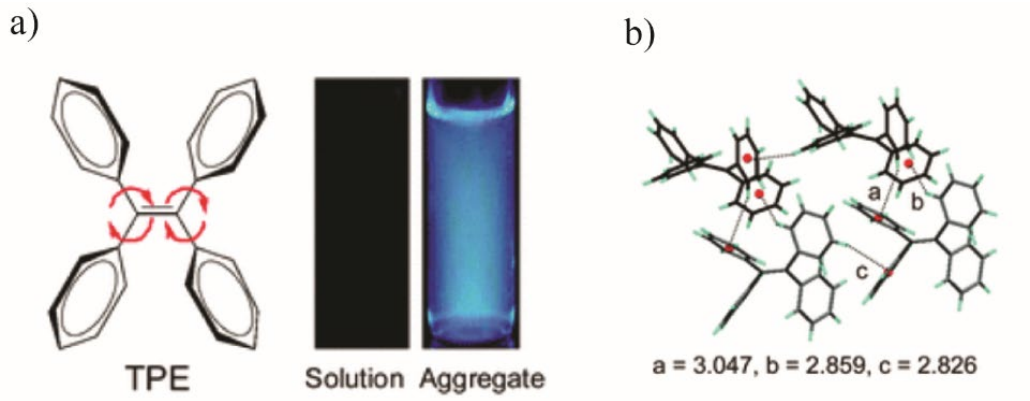

Figure 4.1. (a) Chemical structure of tetraphenylethene (TPE, a typical AIE material) and photographs of a solution and a suspension of TPE in pure tetrahydrofuran (THF) and a THF-water mixture containing 90% volume fraction of water taken under the illumination of a UV lamp. (b) Molecular packing and interactions of TPE molecules. Reproduced from ref [63]. Copyright 2012 Royal Society of Chemistry.

Although some researchers have used AIE materials to prepare MOFs, they only considered them as a linker [64-67]. In this case, the sensitivity of a few AIE materials may be optimised, but actually, the improvement is fairly limited. For example, the quantum yield of AIE-MOF materials may be very low and do not exhibit turn-on type sensing. Shustova *et al.* [61] prepared a novel MOF by coordination of tetrakis(4-carboxyphenyl)ethylene (TCPE, an AIE material) and zinc (Figure 4.2). This MOF has fluorescence and some sensing properties, as the MOF lattice can restrict the intramolecular rotation and this restriction effect is different in different solvents. However, the quantum yield of this material is meagre (1~2%) because of the lack of strong molecular restriction by the framework.

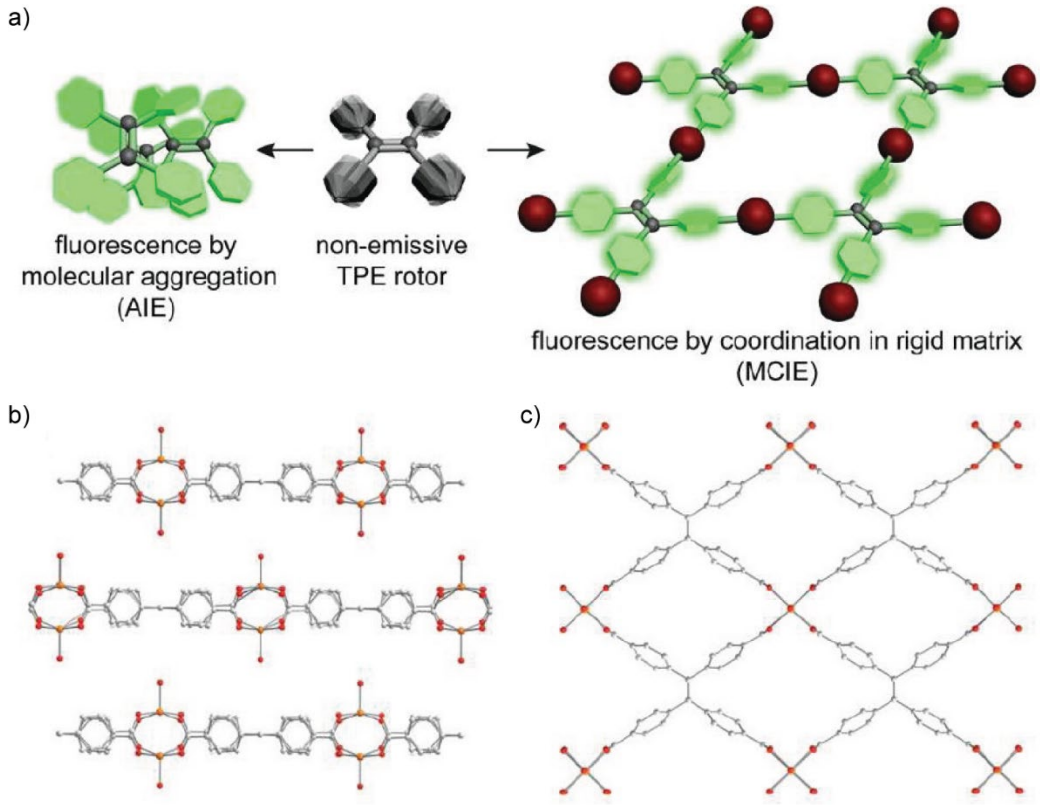

Figure 4.2. (a) Turn-on fluorescence in a TPE rotor by aggregation (AIE) and by coordination in a rigid MOF matrix. Portions of the X-ray crystal structures of the MOF depicting (b) side and (c) top views of the two-dimensional sheets. Orange, red, blue, and grey spheres represent Zn, O, N, and C atoms, respectively. Reproduced from ref [61]. Copyright 2011 American Chemical Society.

Other researchers have prepared MOFs by grafting AIE components onto common linkers. For example, Dong *et al.* [64] combined 4,4′-terphenyldicarboxylate with a TPE derivative ([2-(4-ethynylphenyl)ethene-1,1,2-triyl]tribenzene) to form a new ligand (Figure 4.3). Then they used this ligand to build a new MOF, namely NUS-13-TPE, which exhibits some degree of turn-off thermochromism and solvatochromism (Figure 4.4). The mechanism is closely related to the intramolecular rotation as well. The increase in temperature will lead to more active intramolecular rotation, weakening the fluorescent properties, while

after absorbing solvent molecules within the MOF pores, the intramolecular rotation will be partially blocked thus increasing the fluorescence. However, as shown in Figure 4.3, the synthesis steps of this material are relatively cumbersome and may have a negative impact on subsequent practical applications.

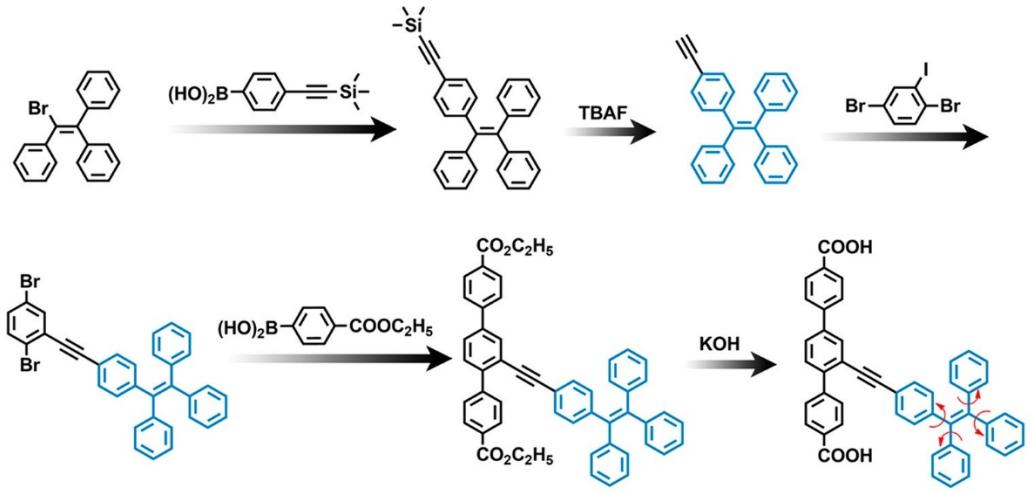

Figure 4.3. Synthesis and structure of the ligand. Reproduced from ref [64]. Copyright 2020 American Chemical Society.

The author is proposing the use of AIE material as a guest to form AIE@MOF systems. This approach can not only simplify the experimental steps, but also restricts the intramolecular rotation of AIE-based guests by a nanoconfinement effect. More importantly, this kind of nanoconfinement could be used as the 'focus' for designing sensors, giving the AIE@MOF system a unique sensing behaviour. In addition, while preparing the AIE@MOF system, the materials processability can be optimised and improved by selecting a suitable/stable MOF host suitable for future engineering applications.

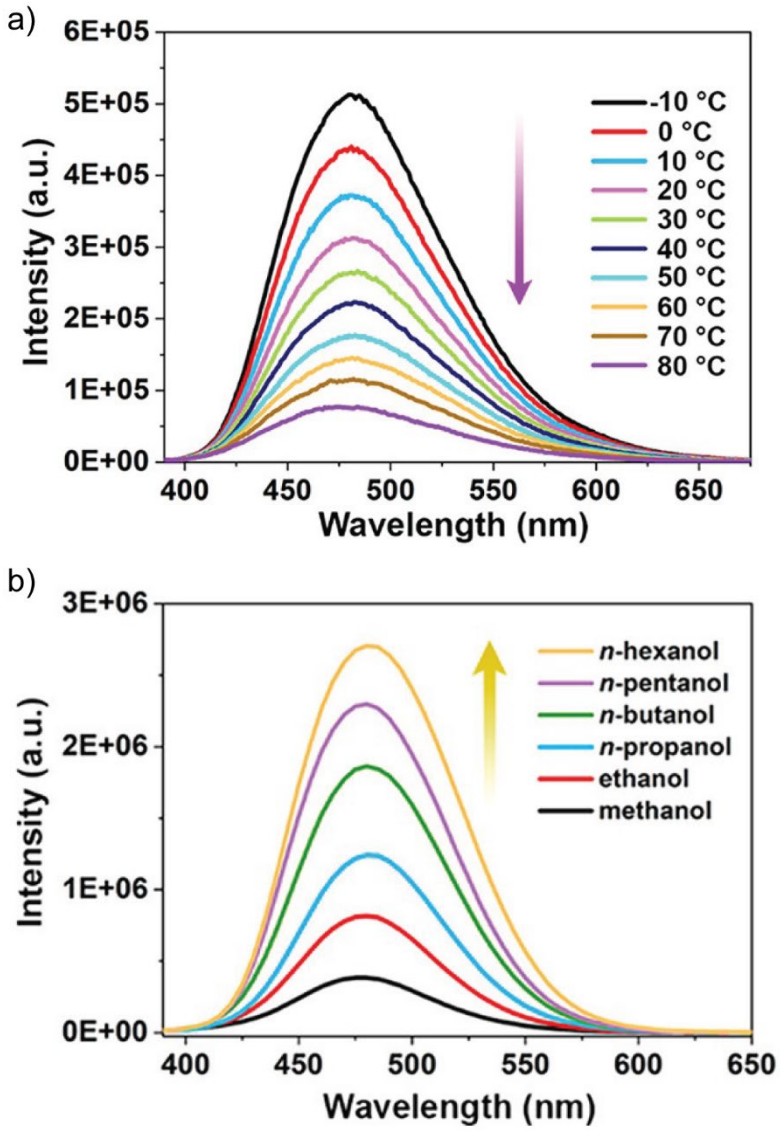

Figure 4.4. (a) Temperature-responsive emission of NUS-13-TPE in DMF solutions recorded between −10 and 80 °C. (b) Fluorescence emission spectra of NUS-13-TPE in various alkyl alcohol solutions at room temperature. Reproduced from ref [64]. Copyright 2020 American Chemical Society.

4.2 Brief Summary of Paper III

To demonstrate the feasibility of the AIE@MOF concept, Paper III selected the most basic AIE material, tetraphenylethene (TPE), and encapsulated it into ZIF-71 pores. One of the reasons for choosing ZIF-71 is by considering the relative

size of the ZIF-71 pores and the TPE molecules. It can be seen from Section 4.1 that when AIE materials themselves are close to each other, there will be a π-π interaction to affect their fluorescence. To give the nanoconfinement effect within the AIE@MOF systems a dominant role in controlling sensing properties, one idea is to fully disperse the AIE guests and encapsulate the monomers into the pores. The size of the TPE dimers was found to be ~ 18.06 Å by density functional theory (DFT) simulation (including the van der Waals surface, see Figure 4.5), while the ZIF-71 pore size is 16.5 Å. Thereby, most TPE guests can only exist as a monomer in the pores of the ZIF-71 host. Additionally, from Papers I and II, it is known that ZIF-71 is straightforward to synthesise and can be scaled up. Therefore, Paper III starts with TPE and ZIF-71 for the follow-up research.

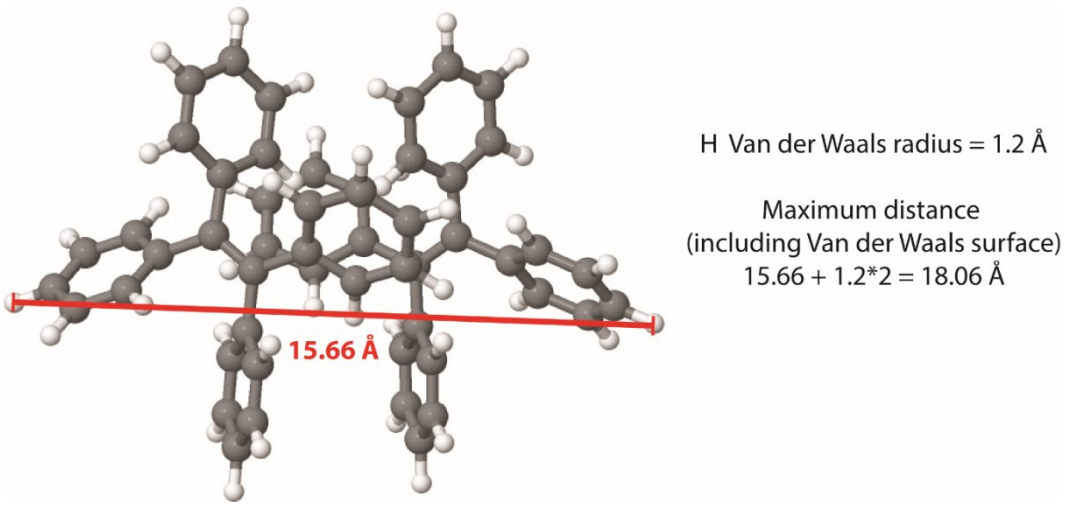

Figure 4.5. The configuration of the TPE dimer calculated from DFT simulation and its maximum molecular size. The structure was obtained through geometrical optimisation employing the B3LYP-D3/6-311G* level of theory (B3LYP = Becke, 3 parameter, Lee Yang Parr).

Like Paper I, Paper III also used the one-pot method to synthesise TPE@ZIF-71. PXRD was first used to confirm the successful formation of the crystal structure (see Fig. 1 in Paper III). Although no trace of TPE was detected in the PXRD pattern, the TGA result (Figure 4.6) demonstrates that TPE does exist in the system with a mass ratio of 0.237 : 96.944. NanoFTIR (Nanoscale Fourier transform infrared spectroscopy) characterisation was conducted to examine the location of TPE, which proves that TPE is encapsulated within the pores rather than absorbed on the crystal surfaces (Fig. 1 in Paper III). ATR-FTIR also shows similar results. As shown in Figure 4.7, the main vibrations of the TPE molecules were not detected in the TPE@ZIF samples. The above characterisation results make it reasonable to infer that the TPE@ZIF-71 system has effectively formed.

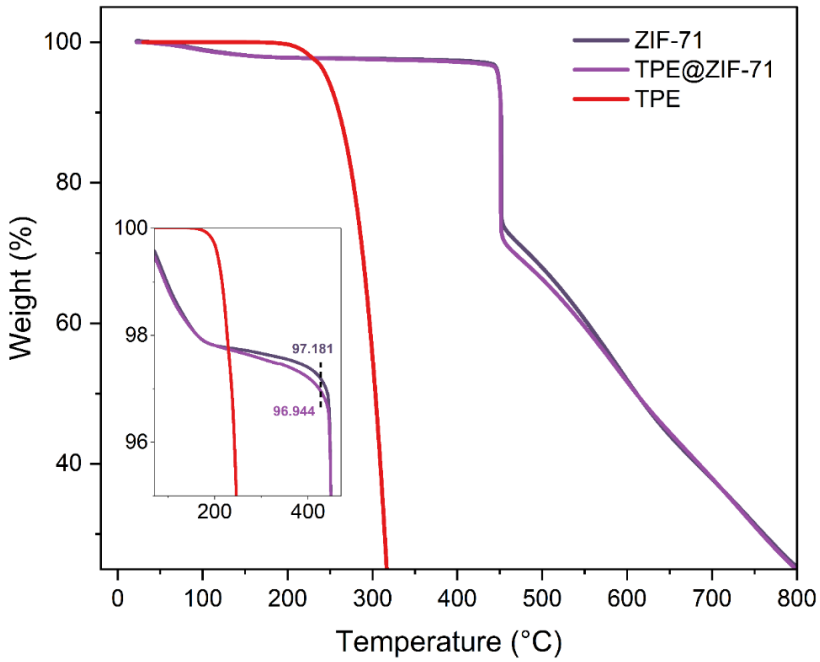

Figure 4.6. TGA results of TPE, TPE@ZIF-71 and ZIF-71. The wt.% of TPE : ZIF-71 = (97.181 – 96.944) : 96.944 = 0.237 : 96.944.

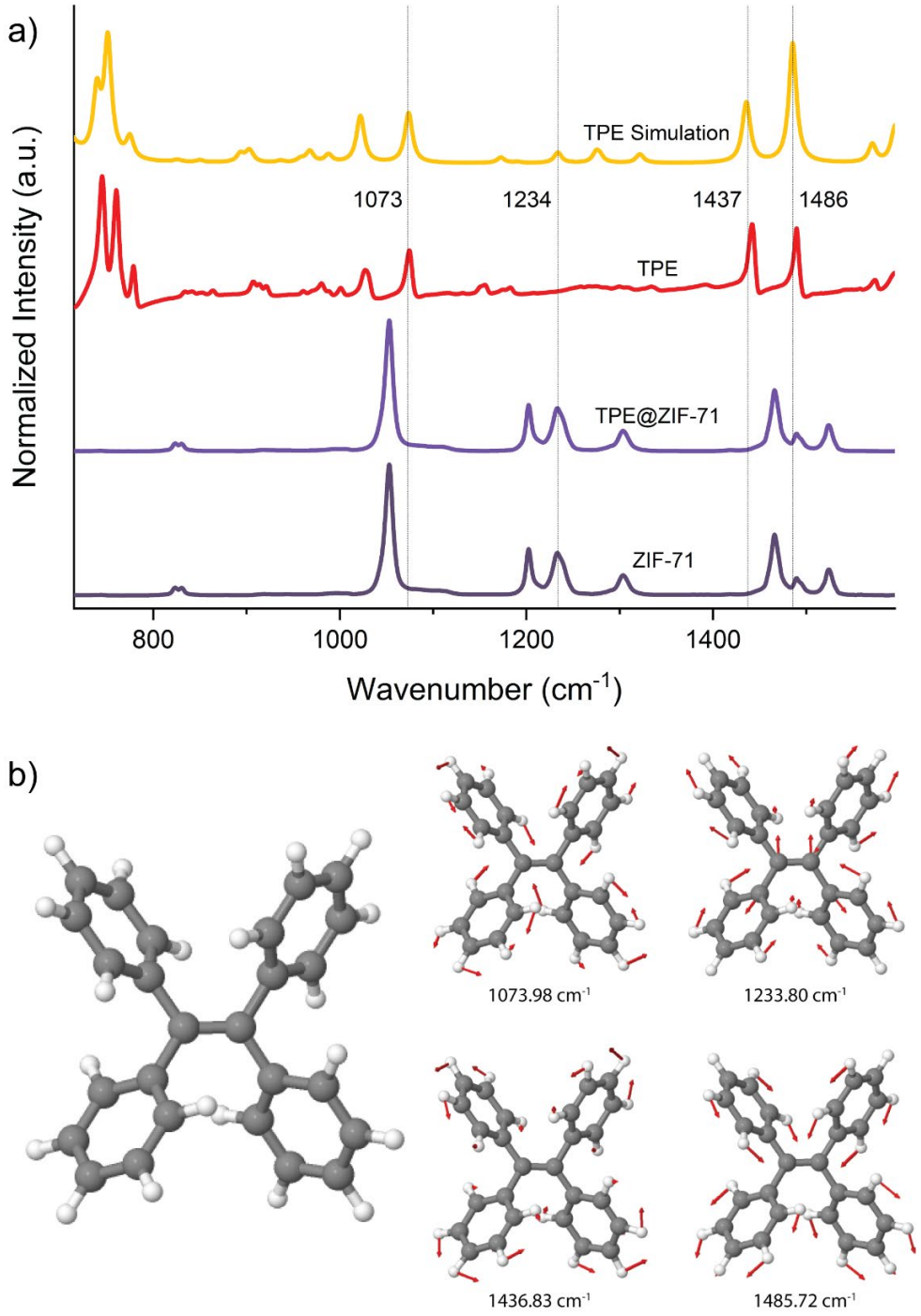

Figure 4.7. (a) ATR-FTIR spectra of TPE, TPE@ZIF-71 and ZIF-71. The predicted TPE spectrum was obtained from DFT calculations at the B3LYP/6-311G* level of theory and implementing an empirical scaling factor of 0.97. (b) DFT simulation results of TPE monomer and its vibrations at 1073.98 cm^{-1}, 1233.80 cm^{-1}, 1436.83 cm^{-1}, and 1485.72 cm^{-1}. The infrared vibrational frequencies are obtained at the B3LYP/6-311G* level of theory and implementing an empirical scaling factor of 0.97. The disappearance of the TPE peaks in (a) is mainly due to the low concentration of the TPE molecules.

The fluorescent properties of the pristine TPE@ZIF-71 powder were subsequently characterised in detail. Its excitation spectra, emission spectra, and lifetime data all confirmed that the fluorescence of the powder comes from the ZIF-71 alone, while the TPE is in a quenching state (Fig. 2 in Paper III). Moreover, due to the existence of the LMCT emission peak in the TPE@ZIF-71 system, it can be reasoned that there is no strong interaction between the TPE and ZIF-71, and the intramolecular vibration of TPE is not affected by ZIF-71 in the pristine powder state.

Subsequently, Paper III has investigated the fluorescent performance of TPE@ZIF-71 under stress. By using a hydraulic press, the TPE@ZIF-71 powder was prepared into different pellets under different pressures. These pellets exhibit a turn-on type red-shifted fluorescence sensing behaviour with increasing pressure (Fig. 3 in Paper III). Interestingly, this is in stark contrast to the pressure-induced response of pure TPE reported (Figure 4.8).

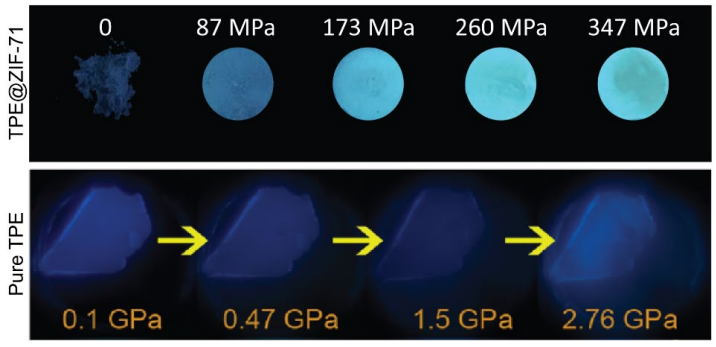

Figure 4.8. Comparison of TPE@ZIF-71 and pure TPE mechanofluorochromism. The result of pure TPE molecules is reproduced from ref [68]. Copyright 2014 American Chemical Society.

Combining terahertz (far-infrared) characterisation, PXRD patterns, and photophysics, the mechanism of the mechanofluorochromism is proposed and demonstrated. In simple terms, in the powder state, the TPE has no emission due to the unrestricted intramolecular rotation, and when pressure is applied, the linker of ZIF-71 (dcIm) will interact with the TPE molecule, exerting a caging effect, and preventing its intramolecular rotation, so leading to enhanced fluorescence. By further increasing the pressure, the crystal structure of ZIF-71 will be partially amorphised, which may cause the formation of aggregates by adjacent TPEs. In that case, the emission will have a more red-shifted and higher intense peak under the stronger caging effect.

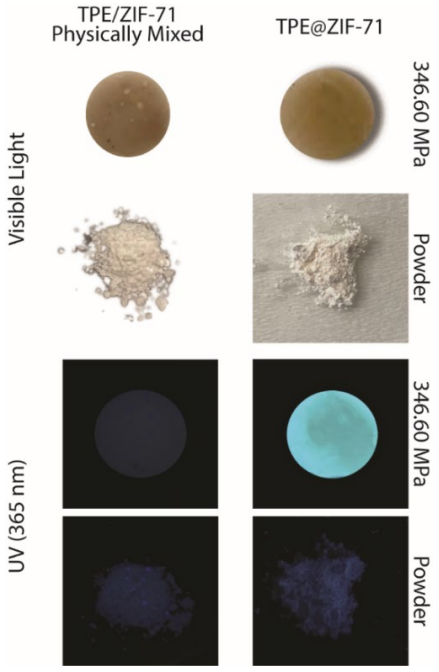

Figure 4.9. TPE/ZIF-71 pellet prepared using a physically mixed powder of TPE and ZIF-71, and TPE@ZIF-71 pellet prepared under a nominal pressure of 346.6 MPa, their colours observed in ambient light, and their fluorescence observed under a 365-nm UV lamp.

To further verify the above mechanism, Paper III compared the properties of physically mixed TPE/ZIF-71 with the TPE@ZIF-71. It is evident from Figure 4.9 that the physically-mixed TPE/ZIF-71 sample is not mechanofluorochromic at all. As a comparison, more TPE@MOF systems composed of other MOF structures were also prepared. Due to their mechanically harder crystal structure, the TPE within these systems does not receive a strong caging effect, resulting in a much weaker mechanofluorochromism than the TPE@ZIF-71 (Figure 4.10). These all increase the credibility of the proposed mechanism.

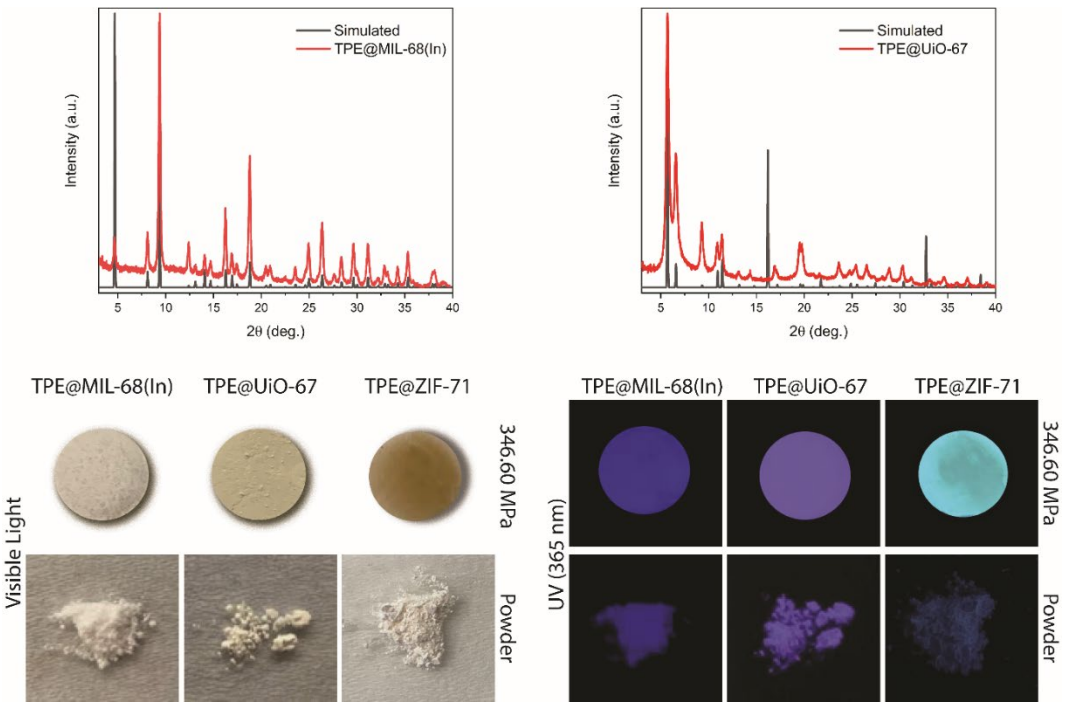

Figure 4.10. Upper row: XRD patterns of TPE@MIL-68(In) and TPE@UiO-67; Lower row: TPE@MIL-68(In), TPE@UiO-67, and TPE@ZIF-71 pellets prepared under a nominal pressure of 346.6 MPa, their colours viewed in ambient light (left), and their fluorescence under a 365 nm UV lamp (right). UiO-67 consists of $Zr_6(OH)_4O_4^{12+}$ clusters connected by 4,4′-biphenyl dicarboxylate linkers forming a framework with fcc structure. MIL-68(In) is introduced in detail in Section 5.2. The reasons why UiO-67 and MIL-68(In) were chosen are described in Paper III (UiO = University of Oslo, MIL = Materials of Institute Lavoisier).

Moreover, the TPE@ZIF-71 can be further processed when combined with some engineering-grade polymers to yield more robust applications. TPE@ZIF-71/PVDF and TPE@ZIF-71/PU (PU = polyurethane) were shown in Paper III, and they were then processed into membranes and fibres using doctor-blade and electrospinning techniques (Figure 4.11). It can be seen that the polymer-based composites not only retain the sensitivity for stress sensing but also have gained improved mechanical stability for better handling compared with the starting powdered material.

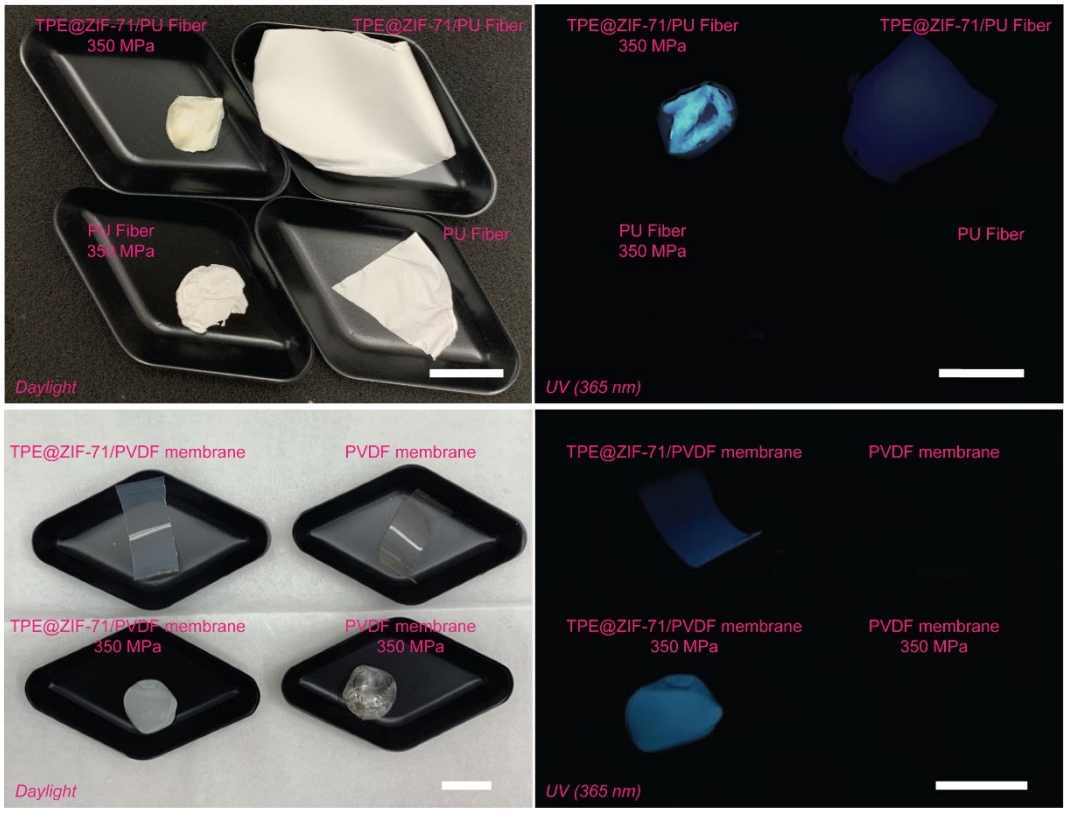

Figure 4.11. Turn-on type mechanofluorochromic behaviour of TPE@ZIF-71/PU fibres and TPE@ZIF-71/PVDF membranes. Note: the samples here are to demonstrate its sensing properties and engineering application potential. Scale bar: 12 mm.

5

Excimers@MOF

5.1 Background and Motivations

Self-trapping excitation is a phenomenon in which excitons interact strongly with phonons (strong electron-phonon coupling) during excitation [69]. It will emit a broad spectrum with a large Stokes shift and commonly exists in halide crystals [70], condensed rare gases [71], and organic molecular crystals [72]. When self-trapping excitation is two-centred, it can be recognised as an 'excimer'. In other words, excimer refers to the dimeric structure formed by two molecules in the excited state but dissociate in the ground state [73].

The fluorescence of excimers is easily affected by the surrounding environment, which makes them good candidates for designing sensing materials [73, 74]. Some scientists have already introduced excimer-related research in the field of fluorescence MOFs by using ligands or analyte-ligand to form excimers [75, 76]. For example, Gutiérrez *et al.* [75] reported a Zr-naphthalene dicarboxylic acid (Zr-NDC) MOF and found the excimer formation between adjacent naphthalene linkers. They also demonstrated that when the Zr-NDC MOF came in contact with polar solvents, the pores of the MOF would be filled, modifying the linker-linker distance, resulting in the blue shift of excimer emission (Figure 5.1). However, it can be seen from Figure 5.1 that this kind of sensing effect is not very noticeable

(peak wavelengths are too similar and there is no intensity change information), probably having limited practical application potential.

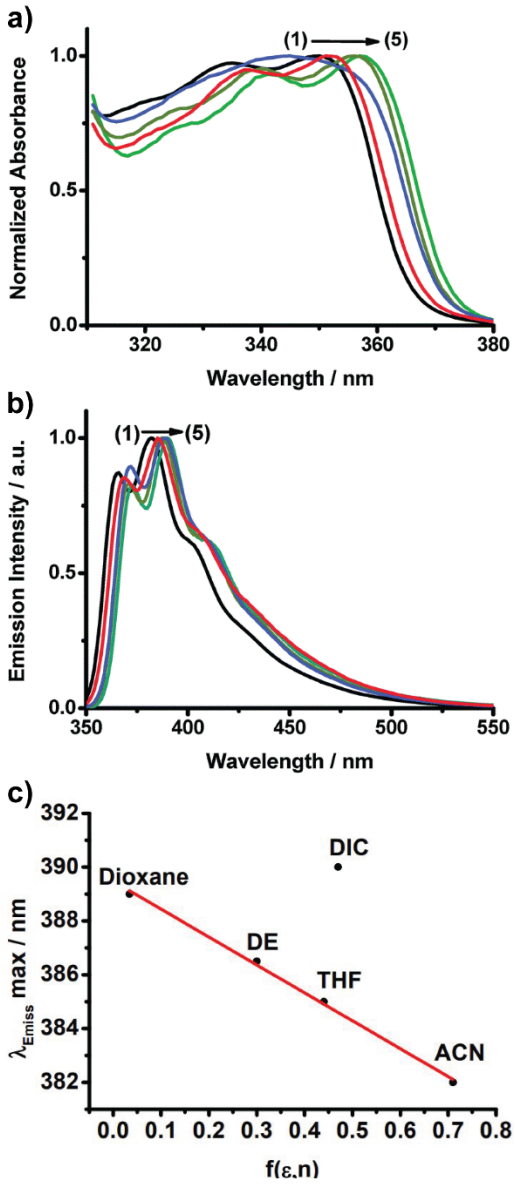

Figure 5.1. a) Normalized UV-vis (a) absorption and (b) fluorescence spectra of Zr-NDC in (1) ACN (black line), (2) THF (red line), (3) DE (dark yellow line), (4) DO (blue line) and (5) DIC (green line) suspensions. For emission, the excitation wavelength was 335 nm. (ACN = acetonitrile, DE = diethyl ether, DO = dioxane, DIC = dichloromethane) (c) Change of the wavelength of the emission intensity maximum of Zr-NDC with the solvent polarity function [f (ε, n), where ε and n are the dielectric constant and the refractive index, respectively]. Reproduced from ref [75]. Copyright 2016 Royal Society of Chemistry.

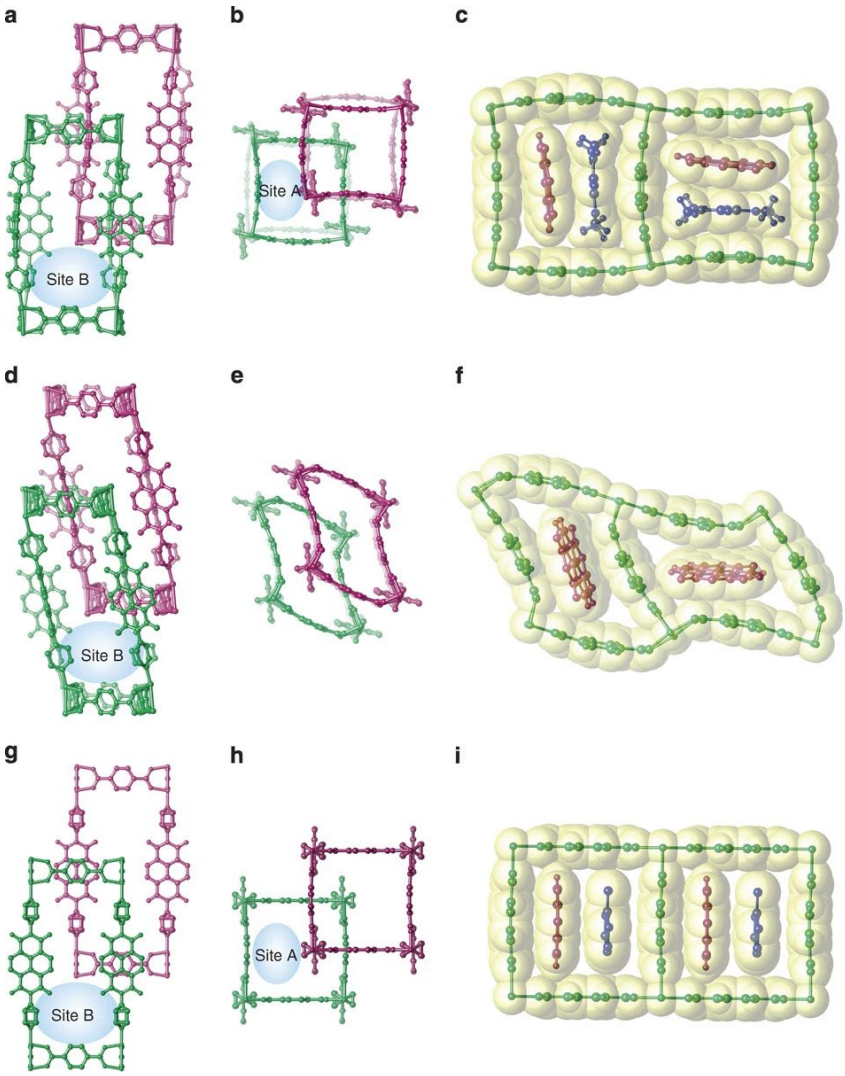

Figure 5.2. (a–i) The crystal structure of the entangled MOF. Site A is defined as the slit-type pore between dpNDI and bdc as shown in (b) and highlighted in (c). Site B illustrated in (a) presents the remaining pore. There are two entangled frameworks as shown, one highlighted in green and the other in purple. The guest DMF and toluene molecules are shown in blue. The van der Waals surface is highlighted in yellow. The exciplex forms between the guest and the NDI moiety embedded in the framework scaffolds (dpNDI = N,N′-di(4-pyridyl)-1,4,5,8-naphthalenediimide, bdc = benzenedicarboxylate). Reproduced from ref [76]. Copyright 2011 Nature Publishing Group.

Another example in the literature is using analytes to form exciplexes with MOF linkers to generate sensing performance (an exciplex is similar to an excimer but with a heterodimeric structure; heterodimeric structure is a dimeric structure

formed by two different monomers). Based on this idea, Takashima *et al.* [76] prepared an entangled MOF and realised turn-on type sensing of several VOCs. The structure and mechanism of this entangled MOF are shown in Figure 5.2. Although the sensing performance of this MOF is promising (Figure 5.3), the synthesis of this MOF is complicated as it requires high temperature and takes about 3 – 4 days. Moreover, in order to test for sensing properties, the MOF needs to be placed in the VOCs for one week because the entangled MOF structure is relatively complex, requiring more time for VOCs to infiltrate. In addition, the long-term stability of this MOF is questionable. These shortcomings will perhaps limit the further development of this material for practical use.

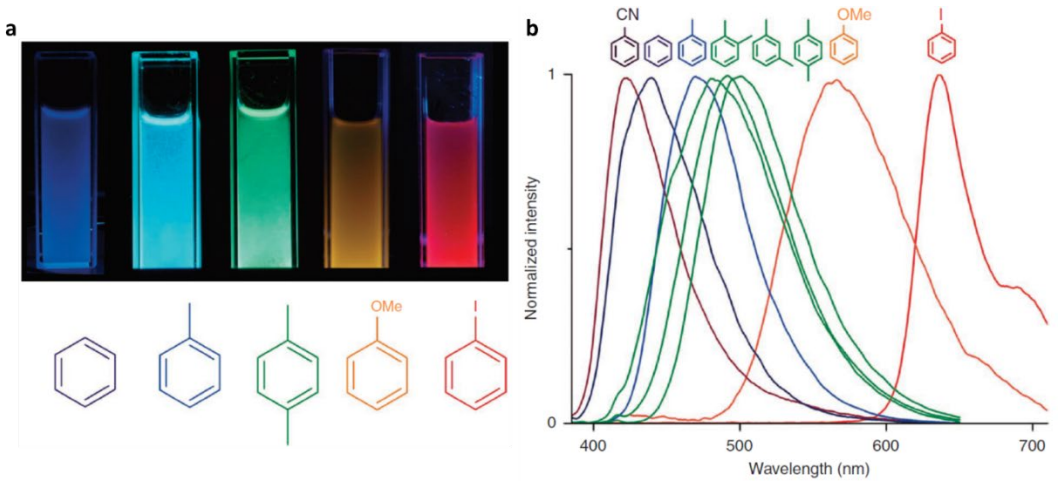

Figure 5.3. (a) The resulting luminescence of crystal powders of the entangled MOF, suspended in each VOC liquid after excitation at 365 nm under a UV lamp. (b) Height-normalised luminescent spectra of VOCs@MOF after excitation at 370 nm. Reproduced from ref [76]. Copyright 2011 Nature Publishing Group.

Currently, studies are scarce on the encapsulation of fluorescent excimers as a guest into MOF structure to form a guest@MOF system for producing sensing

performance. In theory, excimer@MOF has a bright future for sensory applications, as the porous ordered structure of MOF can provide a favourable condition for excimer emission, and MOF is high tuneable, which may enable the excimer to interact with the MOF host, affecting the electron-phonon coupling effect and generating different fluorescent properties. Furthermore, based on the excimer@MOF design concept, excimers and MOFs which are easy-to-synthesis and stable can be selected to improve the overall applicability.

5.2 Brief Summary of Paper IV

According to the above motivation, Paper IV selected perylene as the luminescent guest and prepared the perylene@MIL-68(In) system using the in-situ HCR synthesis method. MIL-68(In) structure consists of the indium octahedrons connected by bdc ligands forming a Kagome lattice in the *ab* plane and cornered along the zigzag chain in the *c* direction [77]. Both PXRD and ATR-FTIR results (Fig. 1 in Paper IV) demonstrated the successful synthesis of the system. It is worth mentioning that this is the first method reported for the rapid synthesis of MIL-68(In) at room temperature. Moreover, the SEM images in Paper IV show that the morphology of crystals obtained is similar to the MIL-68(In) synthesised by the traditional hydrothermal method in the literature.

Unlike other previous studies, Paper IV characterised the mechanical properties of MIL-68(In) and perylene@MIL-68(In) with nanoindentation (Figure 5.4). It can be seen that the hardness of the crystal increases after encapsulating

perylenes, which may also serve as evidence for the successful formation of perylene@MIL-68(In), because the introduction of perylenes may give rise to interstitial hardening, as illustrated in the inset of Figure 5.4.

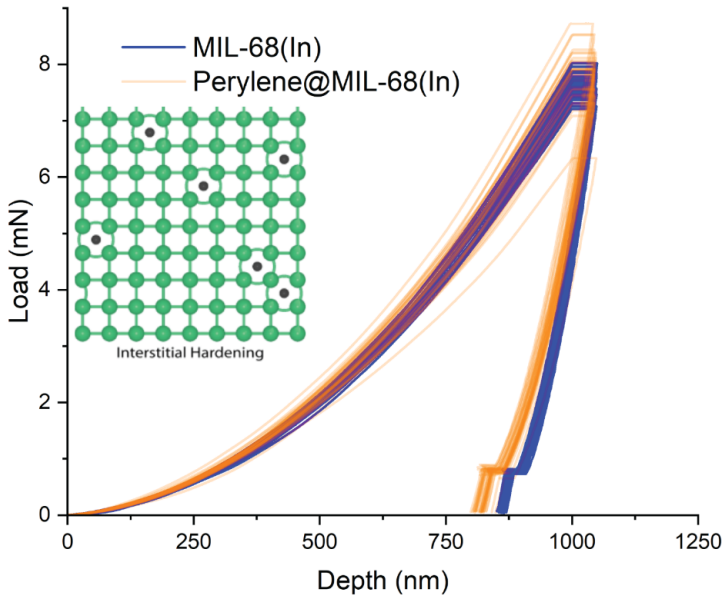

Sample	# of indents	Indentation modulus, *E* (GPa)	Hardness, *H* (MPa)
MIL-68(In)	32	13.24±0.52	402±13
P@MIL-68(In)	32	11.74±0.66	486±32

Figure 5.4. Load-depth curves resulting from nanoindentation tests of MIL-68(In) and perylene@MIL-68(In) with a Berkovich indenter. Young's modulus and hardness measurements obtained using the continuous stiffness measurement (CSM) method. Mean values and standard deviations from this work were calculated from an indentation depth range of 200 – 1000 nm.

Afterwards, Paper IV examined the fluorescent properties of the obtained perylene@MIL-68(In). This material possesses two emission peaks (Fig. 2 in Paper IV). Combined with the analysis of fluorescent lifetime data and excitation-emission spectra, it is reasonable to speculate that the emission peak at around

475 nm comes from the emission of free excitons, while the prominent emission peak at around 600 nm belongs to the E-state excimer emission.

Previous studies supported our hypothesis as well. For example, Ma *et al.* [78] researched the fluorescent properties of pure perylene excimer (Figure 5.5), where the emission of which is almost identical to the ~ 600 nm emission peak of perylene@MIL-68(In). Another relevant example is the perylene@SWCNTs system prepared by Tange *et al.* [79] (SWCNTs = single-walled carbon nanotubes). This composite also exhibits similar excimer emission (Figure 5.6a). More importantly, the diameter of the carbon nanotubes they reported is 1.2 – 1.6 nm, which is similar to the MIL-68(In) channel diameter (16 Å). Therefore, it is reasonable to propose that the structure of perylene excimer in the MIL-68(In) is reminiscent of that observed in perylene@SWCNTs using high-resolution TEM in ref [79]. It is speculated that the perylene molecules exist as disordered dimeric structures, and the longest axis of the perylene molecules tilts in the radial direction of the MIL-68(In) channels (akin to Figure 5.6b for nanotubes).

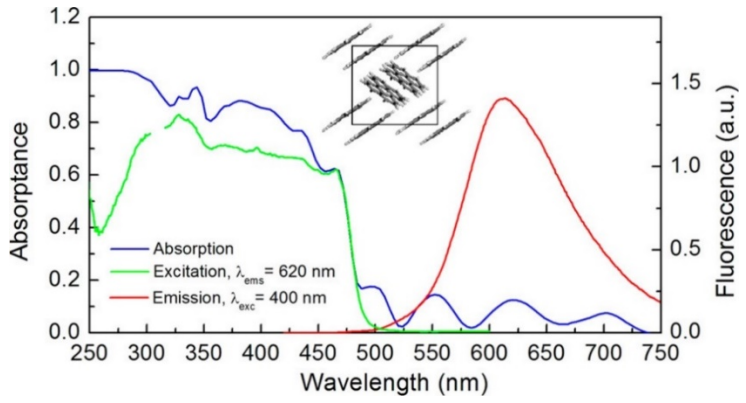

Figure 5.5. Steady-state absorption, fluorescence, and excitation spectra of perylene excimers. Reproduced from ref [78]. Copyright 2014 American Chemical Society.

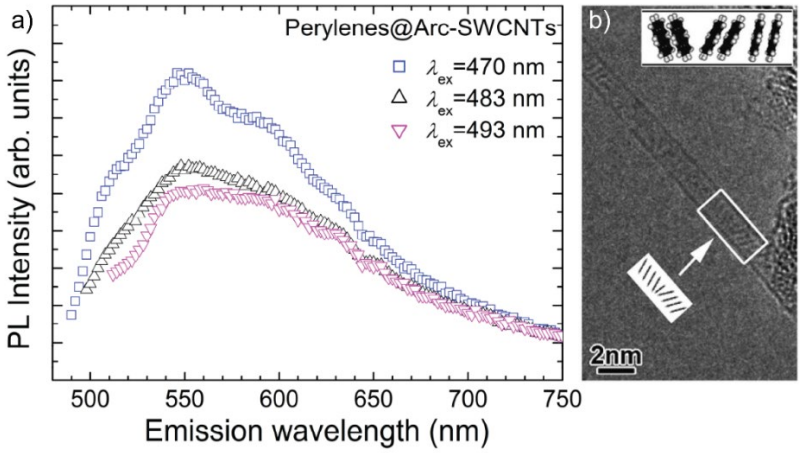

Figure 5.6. a) Emission spectra of perylenes@SWCNTs at different excitation wavelengths. b) The disordered dimeric structure corresponding to perylene molecules encapsulated within SWCNTs. The insets show the configurations of the perylene molecules. Reproduced from ref [79]. Copyright 2016 Royal Society of Chemistry.

Paper IV then demonstrated the solvatochromism of perylene@MIL-68(In) and found it could exhibit a turn-on type sensing response for benzene, toluene, and xylene, namely BTX. When exposed to BTX, the emission peak of perylene@MIL-68(In) showed a slight blue-shift, intensity increase, and peak splitting (Fig. 3b in Paper IV).

The reason for the turn-on sensing behaviour is due to the transformation from the E-state perylene excimer to the Y-state excimer. When BTX enters the channel of MIL-68(In), a π-π interaction bridge (Scheme 1 in Paper IV) will form between the linker (bdc), BTX, and perylene excimer, which may affect the electron – phonon coupling and transform the E-excimers to Y-excimers. Because Y-type excimers themselves have higher emission intensity, multiple emission peaks, and smaller wavelengths (Figure 5.7), the whole system shows the turn-on sensitivity.

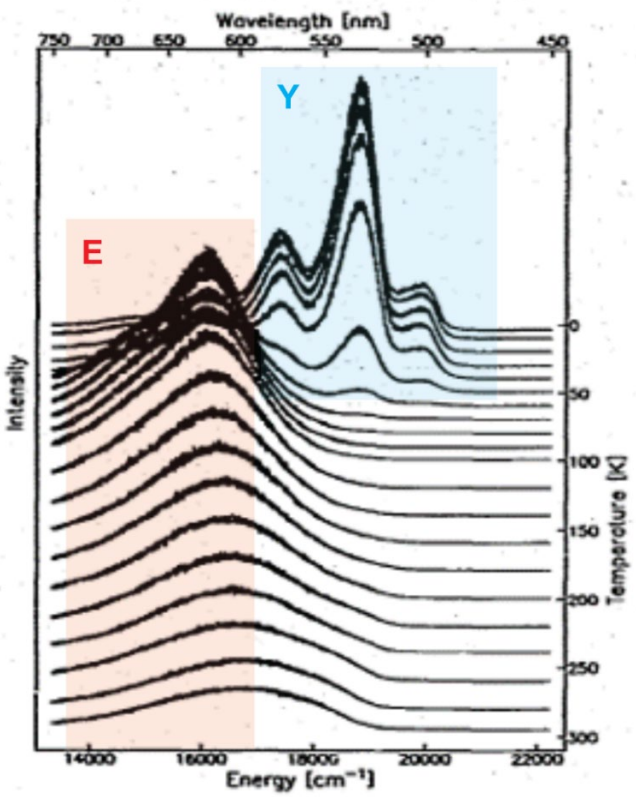

Figure 5.7. Temperature-dependent fluorescence spectra of perylene excimers. Regions marked E and Y denote the two different excimers of perylene observed as a function of temperature. Reproduced from ref [80]. Copyright 1985 Elsevier.

This kind of E- to Y-excimers transformation *via* the π-π interaction bridge was achieved for the first time. Previously, Y-type excimer fluorescence could only be realised by lowering the temperature since the lattice vibration (phonons) would be limited at low temperatures. It is generally accepted that when the temperature is below 50 K, the perylene excimer will change from the E-state to Y-state, as shown in Figure 5.7.

In-depth analysis of Figure 5.7 and our deconvolution result for perylene@MIL-68(In) in xylene (Figure 5.8) reveals that the relative intensity and peak position of the deconvoluted peak can be assigned to the fluorescence of

Y-type excimer in Figure 5.7, which further confirms the validity of the proposed theory. This study shows that the idea of excimers@MOF does provide a novel platform for developing unconventional fluorescence sensing materials with a unique turn-on capability.

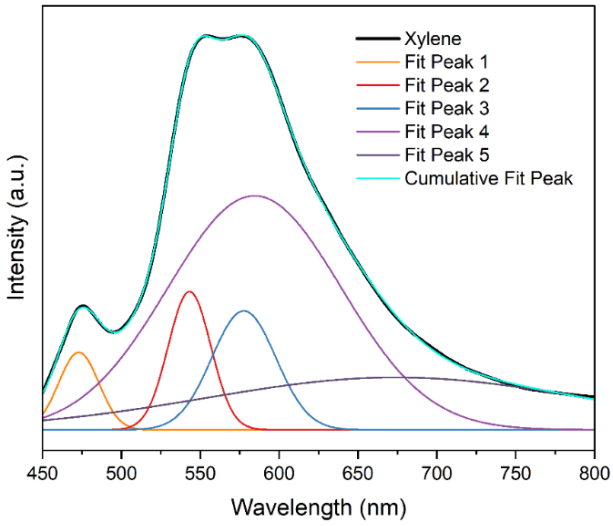

Model	Gaussian curve fit				
Equation	$y = y_0 + \frac{A}{w * \sqrt{\frac{\pi}{4 * \ln(2)}}} * e^{\frac{-4*\ln(2)*(x-x_c)^2}{w^2}}$				
Plot	Peak1 (Intensity)	Peak2 (Intensity)	Peak3 (Intensity)	Peak4 (Intensity)	Peak5 (Intensity)
y_0	-26932.8 ± 33059.8	-26932.8 ± 33059.8	-26932.8 ± 33059.8	-26932.8 ± 33059.8	-26932.8 ± 33059.8
x_c	473. 0 ± 0.1	543.2 ± 0.1	577.6 ± 0.3	584.4 ± 2.7	674.0 ± 58.2
A	2777278.4 ± 167134.3	5263344.9 ± 182305.5	6808557.9 ± 285976.7	36278100.0 ± 6350215.6	17824000.0 ± 25039400.0
w	30.0 ± 0.6	31.8 ± 0.3	47.9 ± 0.7	129.5 ± 4.9	284.2 ± 187.2
Reduced Chi-Sqr	1551025.018				
R-Square (COD)	0.99992				
Adj. R-Square	0.99992				

Figure 5.8. Deconvolution of the emission spectrum of perylene@MIL-68(In) in xylene by using the Gaussian method implemented in OriginPro [81].

6

Conclusions and Future Outlook

This work designs, fabricates, and investigates guest@MOF fluorescent sensing materials with practical engineering potential, and explores the complex underlying sensing mechanism in detail. Three novel fluorescence sensing guest@MOF systems have been developed: Aggregates@MOF, AIE@MOF, and Excimer@MOF. A systematic characterisation was carried out to study the mechanisms, host-guest interactions, and structures of each system from the perspective of photophysics. Some polymers and industrial processing techniques have been combined with the developed guest@MOF composites to improve their engineering robustness further. Main conclusions can be drawn in the following areas.

6.1 Aggregates@MOF

- The idea of aggregates@MOF systems is proving to be a feasible method for designing fluorescence sensing materials. In particular, it offers unique advantages for preparing multi-stimuli responsive smart sensors.
- The aggregates@MOF system synthesised by the simple one-pot method in Paper I (RhB@ZIF-71) exhibits mechanochromism, thermochromism, and solvatochromism (~ tens of nanometres). By applying photophysical

analysis, a core sensing mechanism has been established from these multi-chromic behaviours: aggregates of different sizes will receive different caging effects offered by the (host) MOF structure under certain conditions (e.g., temperature, pressure, chemicals), thus showing different fluorescent properties for use as luminescent sensors.

- The aggregates@MOF system has excellent processibility. Paper II reports the preparation of the first aggregates@MOF/polymer electrospun fibres. These fibres not only retain the sensing performance but also exhibit high quantum yield (>90%) and excellent thermal stability. These characteristics are promising for engineering applications.

6.2 AIE@MOF

- Unlike traditional ACQ materials, the emergence of AIE materials provides a new pathway to design turn-on type fluorescence sensors. The AIE@MOF systems encapsulating AIE materials into MOFs can generate an enhanced sensing performance (~ tenfold) as demonstrated in Paper III for the TPE@ZIF-71 system.
- Terahertz infrared spectroscopic characterisation and photophysical results show that the nanoconfinement effect offered by MOFs can effectively restrict the intramolecular rotation and spontaneous recrystallisation of AIE materials. This methodology is useful for

optimising the fluorescent properties of AIE@MOF systems and broadening their future development.

- AIE@MOF has been shown to be compatible with engineering-grade polymers and can be further processed into photoluminescent sensing fibres or membranes, possessing commercial potential.

6.3 Excimer@MOF

- A new sensing mechanism has been established based on the excimer@MOF system. The porous ordered and tuneable lattice of MOF allows the possibility of controlling the electron-phonon coupling effect of excimers and thus modifying their fluorescent properties, which provides a novel approach for developing new fluorescence sensing materials.
- Paper IV demonstrates the feasibility and superiority of excimer@MOF fluorescence sensing by taking perylene@MIL-68(In) as an example. For benzene, toluene, and xylene, which are difficult to be detected with traditional materials, perylene@MIL-68(In) could achieve unique turn-on sensing. In this study, the transformation of perylene E-excimer to Y-excimer was discovered for the first time at room temperature.

6.4 Future Outlook

The idea involved in this work of establishing novel sensing mechanisms by considering the guest type/guest configuration/guest-MOF interaction and proving them by photophysics analysis will undoubtedly stimulate more future research into the fluorescent sensing field. Furthermore, the approach of combining with robust polymers will also drive more practical engineering applications of LG@MOF systems. These can be:

- Aggregates@MOF, AIE@MOF, and excimer@MOF all have broad prospects, so it is reasonable to design and perform more related guest@MOF materials in the future. For example, pyrene can be used to prepare a new excimer@MOF system.
- The three systems developed can be cross-combined or modified to generate more exciting fluorescence sensing composites. For example, aggregates of AIE materials or excimers can be encapsulated into MOF. Two or more types of aggregates, AIE, or excimer in the guest@MOF system may also help to create unusual sensing behaviours.
- Guest@MOF/polymer composites need more research to improve the sensitivity of guest@MOF materials and the stability of polymers. For example, in Paper II, after RhB@ZIF-71 was made into electrospun fibres, its solvatochromism became very weak. The reason is that the PVDF prevents direct contact between the RhB and analyte solvents. The fibres may need to be porous to overcome this problem.

- The sensing systems prepared in this work are all irreversible (the fluorescent properties do not return after removal of the stimulus), which is beneficial to produce some sensors for recording stimulus history. However, reversible sensing systems should also be given more attention to meet more practical engineering applications.
- More advanced analytical equipment should be used to help characterise complex guest@MOF systems. For example, the NMR technique can be used to estimate the number of guests within one MOF pore. NanoFTIR is useful to detect whether the guest is within the MOF structure or attached to the MOF crystal surface.

References

[1] Dincer, C.; Bruch, R.; Costa-Rama, E.; Fernandez-Abedul, M. T.; Merkoci, A.; Manz, A.; Urban, G. A.; Guder, F., Disposable Sensors in Diagnostics, Food, and Environmental Monitoring. *Adv. Mater.* **2019,** 31, 1806739.

[2] Silva, A. P. d.; Eilers, J.; Zlokarnik, G., Emerging Fluorescence Sensing Technologies: From Photophysical Principles to Cellular Applications. *Proc. Natl. Acad. Sci. U.S.A* **1999,** 96, 8336-8337.

[3] Sabri, N.; Aljunid, S. A.; Salim, M. S.; Ahmad, R. B.; Kamaruddin, R., Toward Optical Sensors: Review and Applications. *J. Phys. Conf. Ser.* **2013,** 423, 012064.

[4] Babal, A. S.; Donà, L.; Ryder, M. R.; Titov, K.; Chaudhari, A. K.; Zeng, Z.; Kelley, C. S.; Frogley, M. D.; Cinque, G.; Civalleri, B.; Tan, J.-C., Impact of Pressure and Temperature on the Broadband Dielectric Response of the HKUST-1 Metal–Organic Framework. *J. Phys. Chem. C* **2019,** 123, 29427-29435.

[5] Moreno, I.; Davis, J. A.; Ruiz, I.; Cottrell, D. M., Decomposition of Radially and Azimuthally Polarized Beams Using a Circular-Polarization and Vortex-Sensing Diffraction Grating. *Opt. Express* **2010,** 18, 7173-7183.

[6] Park, T. S.; Yoon, J.-Y., Smartphone Detection of *Escherichia coli* From Field Water Samples on Paper Microfluidics. *IEEE Sens. J.* **2015,** 15, 1902-1907.

[7] Shaked, N. T., Quantitative Phase Microscopy of Biological Samples Using a Portable Interferometer. *Opt. Lett.* **2012,** 37, 2016-2018.

[8] Wu, D.; Sedgwick, A. C.; Gunnlaugsson, T.; Akkaya, E. U.; Yoon, J.; James, T. D., Fluorescent Chemosensors: the Past, Present and Future. *Chem. Soc. Rev.* **2017,** 46, 7105-7123.

[9] Shin, Y.-H.; Teresa Gutierrez-Wing, M.; Choi, J.-W., Review—Recent Progress in Portable Fluorescence Sensors. *J. Electrochem. Soc.* **2021,** 168, 017502.

[10] Cui, Y.; Yue, Y.; Qian, G.; Chen, B., Luminescent Functional Metal-Organic Frameworks. *Chem. Rev.* **2012,** 112, 1126-1162.

[11] Allendorf, M. D.; Bauer, C. A.; Bhakta, R. K.; Houk, R. J., Luminescent Metal-Organic Frameworks. *Chem. Soc. Rev.* **2009,** 38, 1330-1352.

[12] Heine, J.; Muller-Buschbaum, K., Engineering Metal-Based Luminescence in Coordination Polymers and Metal-Organic Frameworks. *Chem. Soc. Rev.* **2013,** 42, 9232-9242.

[13] Hao, J.; Xu, X.; Fei, H.; Li, L.; Yan, B., Functionalization of Metal-Organic Frameworks for Photoactive Materials. *Adv. Mater.* **2018,** 30, 1705634.

[14] Furukawa, H.; Go, Y. B.; Ko, N.; Park, Y. K.; Uribe-Romo, F. J.; Kim, J.; O'Keeffe, M.; Yaghi, O. M., Isoreticular Expansion of Metal-Organic Frameworks with Triangular and Square Building Units and the Lowest Calculated Density for Porous Crystals. *Inorg. Chem.* **2011,** 50, 9147-9152.

[15] Jiang, J.; Zhao, Y.; Yaghi, O. M., Covalent Chemistry beyond Molecules. *J. Am. Chem. Soc.* **2016,** 138, 3255-3265.

[16] Ryder, M. R.; Civalleri, B.; Cinque, G.; Tan, J. C., Discovering Connections between Terahertz Vibrations and Elasticity Underpinning the Collective Dynamics of the HKUST-1 Metal–Organic Framework. *CrystEngComm* **2016,** 18, 4303-4312.

[17] Yuan, S.; Feng, L.; Wang, K.; Pang, J.; Bosch, M.; Lollar, C.; Sun, Y.; Qin, J.; Yang, X.; Zhang, P.; Wang, Q.; Zou, L.; Zhang, Y.; Zhang, L.; Fang, Y.; Li, J.; Zhou, H. C., Stable Metal-Organic Frameworks: Design, Synthesis, and Applications. *Adv. Mater.* **2018,** 30, 1704303.

[18] Allendorf, M. D.; Medishetty, R.; Fischer, R. A., Guest Molecules as a Design Element for Metal–Organic Frameworks. *MRS Bull.* **2016,** 41, 865-869.

[19] Cui, Y.; Li, B.; He, H.; Zhou, W.; Chen, B.; Qian, G., Metal-Organic Frameworks as Platforms for Functional Materials. *Acc. Chem. Res.* **2016,** 49, 483-93.

[20] Lustig, W. P.; Mukherjee, S.; Rudd, N. D.; Desai, A. V.; Li, J.; Ghosh, S. K., Metal-Organic Frameworks: Functional Luminescent and Photonic Materials for Sensing Applications. *Chem. Soc. Rev.* **2017,** 46, 3242-3285.

[21] Diamantis, S. A.; Margariti, A.; Pournara, A. D.; Papaefstathiou, G. S.; Manos, M. J.; Lazarides, T., Luminescent Metal–Organic Frameworks as Chemical Sensors: Common Pitfalls and Proposed Best Practices. *Inorg. Chem. Front.* **2018,** 5, 1493-1511.

[22] Chaudhari, A. K.; Ryder, M. R.; Tan, J. C., Photonic Hybrid Crystals Constructed from *In Situ* Host-Guest Nanoconfinement of a Light-Emitting Complex in Metal-Organic Framework Pores. *Nanoscale* **2016,** 8, 6851-6859.

[23] Lu, G.; Li, S.; Guo, Z.; Farha, O. K.; Hauser, B. G.; Qi, X.; Wang, Y.; Wang, X.; Han, S.; Liu, X.; DuChene, J. S.; Zhang, H.; Zhang, Q.; Chen, X.; Ma, J.; Loo, S. C.; Wei, W. D.; Yang, Y.; Hupp, J. T.; Huo, F., Imparting Functionality to a Metal-Organic Framework Material by Controlled Nanoparticle Encapsulation. *Nat. Chem.* **2012,** 4, 310-316.

[24] Xiong, T.; Zhang, Y.; Donà, L.; Gutiérrez, M.; Möslein, A. F.; Babal, A. S.; Amin, N.; Civalleri, B.; Tan, J.-C., Tunable Fluorescein-Encapsulated Zeolitic Imidazolate Framework-8 Nanoparticles for Solid-State Lighting. *ACS Appl. Nano Mater.* **2021,** 4, 10321-10333.

[25] Zhang, Y.; Gutiérrez, M.; Chaudhari, A. K.; Tan, J. C., Dye-Encapsulated Zeolitic Imidazolate Framework (ZIF-71) for Fluorochromic Sensing of Pressure, Temperature, and Volatile Solvents. *ACS Appl. Mater. Interfaces* **2020,** 12, 37477-37488.

[26] Chaudhari, A. K.; Kim, H. J.; Han, I.; Tan, J. C., Optochemically Responsive 2D Nanosheets of a 3D Metal-Organic Framework Material. *Adv. Mater.* **2017,** 29, 1701463.

[27] Juan-Alcañiz, J.; Gascon, J.; Kapteijn, F., Metal–Organic Frameworks as Scaffolds for the Encapsulation of Active Species: State of the Art and Future Perspectives. *J. Mater. Chem.* **2012,** 22, 10102-10118.

[28] Hester, P.; Xu, S.; Liang, W.; Al-Janabi, N.; Vakili, R.; Hill, P.; Muryn, C. A.; Chen, X.; Martin, P. A.; Fan, X., On Thermal Stability and Catalytic Reactivity of Zr-Based Metal–Organic Framework (UiO-67) Encapsulated Pt Catalysts. *J. Catal* **2016,** 340, 85-94.

[29] Yan, D.; Tang, Y.; Lin, H.; Wang, D., Tunable Two-Color Luminescence and Host-guest Energy Transfer of Fluorescent Chromophores Encapsulated in Metal-Organic Frameworks. *Sci. Rep.* **2014,** 4, 4337.

[30] Muller, M.; Devaux, A.; Yang, C. H.; De Cola, L.; Fischer, R. A., Highly Emissive Metal-Organic Framework Composites by Host-Guest Chemistry. *Photochem. Photobiol. Sci.* **2010,** 9, 846-853.

[31] Tu, M.; Reinsch, H.; Rodriguez-Hermida, S.; Verbeke, R.; Stassin, T.; Egger, W.; Dickmann, M.; Dieu, B.; Hofkens, J.; Vankelecom, I. F. J.; Stock, N.; Ameloot, R., Reversible Optical Writing and Data Storage in an Anthracene-Loaded Metal-Organic Framework. *Angew. Chem. Int. Ed.* **2019,** 58, 2423-2427.

[32] Asadi, F.; Azizi, S. N.; Chaichi, M. J., Green Synthesis of Fluorescent PEG-ZnS QDs Encapsulated into Co-MOFs as an Effective Sensor for Ultrasensitive Detection of Copper Ions in Tap Water. *Mater. Sci. Eng. C Mater. Biol. Appl.* **2019,** 105, 110058.

[33] Zhang, D. S.; Gao, Q.; Chang, Z.; Liu, X. T.; Zhao, B.; Xuan, Z. H.; Hu, T. L.; Zhang, Y. H.; Zhu, J.; Bu, X. H., Rational Construction of Highly Tunable Donor-Acceptor Materials Based on a Crystalline Host-Guest Platform. *Adv. Mater.* **2018,** 30, 1804715.

[34] Gutiérrez, M.; Martín, C.; Van der Auweraer, M.; Hofkens, J.; Tan, J. C., Electroluminescent Guest@MOF Nanoparticles for Thin Film Optoelectronics and Solid-State Lighting. *Adv. Opt. Mater.* **2020,** 8, 2000670.

[35] Lee, Y.-R.; Jang, M.-S.; Cho, H.-Y.; Kwon, H.-J.; Kim, S.; Ahn, W.-S., ZIF-8: A Comparison of Synthesis Methods. *Chem. Eng. J.* **2015,** 271, 276-280.

[36] Zhang, Y.; Tan, J. C., Electrospun Rhodamine@MOF/Polymer Luminescent Fibers with a Quantum Yield of Over 90%. *iScience* **2021,** 24, 103035.

[37] Ji, G.; Zheng, T.; Gao, X.; Liu, Z., A Highly Selective Turn-on Luminescent Logic Gates Probe Based on Post-Synthetic MOF for Aspartic Acid Detection. *Sens. Actuators B Chem.* **2019,** 284, 91-95.

[38] Xie, W.; Qin, J.-S.; He, W.-W.; Shao, K.-Z.; Su, Z.-M.; Du, D.-Y.; Li, S.-L.; Lan, Y.-Q., Encapsulation of an Iridium Complex in a Metal–Organic Framework to Give a Composite with Efficient White Light Emission. *Inorg. Chem. Front.* **2017,** 4, 547-552.

[39] Gao, Q.; Xu, S.; Guo, C.; Chen, Y.; Wang, L., Embedding Nanocluster in MOF via Crystalline Ion-Triggered Growth Strategy for Improved Emission and Selective Sensing. *ACS Appl. Mater. Interfaces* **2018,** 10, 16059-16065.

[40] Lin, X.; Gao, G.; Zheng, L.; Chi, Y.; Chen, G., Encapsulation of Strongly Fluorescent Carbon Quantum Dots in Metal-Organic Frameworks for Enhancing Chemical Sensing. *Anal. Chem.* **2014,** 86, 1223-1228.

[41] Mollick, S.; Mandal, T. N.; Jana, A.; Fajal, S.; Desai, A. V.; Ghosh, S. K., Ultrastable Luminescent Hybrid Bromide Perovskite@MOF Nanocomposites for the Degradation of Organic Pollutants in Water. *ACS Appl. Nano Mater.* **2019,** 2, 1333-1340.

[42] Hu, X. L.; Qin, C.; Wang, X. L.; Shao, K. Z.; Su, Z. M., A Luminescent Dye@MOF as a Dual-Emitting Platform for Sensing Explosives. *Chem. Commun.* **2015,** 51, 17521-17524.

[43] Chaudhari, A. K.; Tan, J. C., Mechanochromic MOF Nanoplates: Spatial Molecular Isolation of Light-Emitting Guests in a Sodalite Framework Structure. *Nanoscale* **2018,** 10, 3953-3960.

[44] Liu, J.; Zhao, Y.; Li, X.; Wu, J.; Han, Y.; Zhang, X.; Xu, Y., Dual-Emissive $CsPbBr_3$@Eu-BTC Composite for Self-Calibrating Temperature Sensing Application. *Cryst. Growth Des.* **2020,** 20, 454-459.

[45] Deng, J.; Wang, K.; Wang, M.; Yu, P.; Mao, L., Mitochondria Targeted Nanoscale Zeolitic Imidazole Framework-90 for ATP Imaging in Live Cells. *J. Am. Chem. Soc.* **2017,** 139, 5877-5882.

[46] Zhang, Y.; Yuan, S.; Day, G.; Wang, X.; Yang, X.; Zhou, H.-C., Luminescent Sensors Based on Metal-Organic Frameworks. *Coord. Chem. Rev.* **2018,** 354, 28-45.

[47] Dong, M. J.; Zhao, M.; Ou, S.; Zou, C.; Wu, C. D., A Luminescent Dye@MOF Platform: Emission Fingerprint Relationships of Volatile Organic Molecules. *Angew. Chem. Int. Ed.* **2014,** 53, 1575-1579.

[48] Jin, H.-G.; Zong, W.; Yuan, L.; Zhang, X.-B., Nanoscale Zeolitic Imidazole Framework-90: Selective, Sensitive and Dual-Excitation Ratiometric Fluorescent Detection of Hazardous Cr(VI) Anions in Aqueous Media. *New J. Chem.* **2018,** 42, 12549-12556.

[49] Karmakar, A.; Joarder, B.; Mallick, A.; Samanta, P.; Desai, A. V.; Basu, S.; Ghosh, S. K., Aqueous Phase Sensing of Cyanide Ions Using a Hydrolytically Stable Metal-Organic Framework. *Chem. Commun.* **2017,** 53, 1253-1256.

[50] Gutierrez, M.; Zhang, Y.; Tan, J. C., Confinement of Luminescent Guests in Metal-Organic Frameworks: Understanding Pathways from Synthesis and Multimodal Characterization to Potential Applications of LG@MOF Systems. *Chem. Rev.* **2022**.

[51] Li, B.; Wen, H. M.; Cui, Y.; Zhou, W.; Qian, G.; Chen, B., Emerging Multifunctional Metal-Organic Framework Materials. *Adv. Mater.* **2016,** 28, 8819-8860.

[52] Chen, D. M.; Zhang, N. N.; Liu, C. S.; Du, M., Dual-Emitting Dye@MOF Composite as a Self-Calibrating Sensor for 2,4,6-Trinitrophenol. *ACS Appl. Mater. Interfaces* **2017,** 9, 24671-24677.

[53] Su, Z.; Miao, Y. R.; Mao, S. M.; Zhang, G. H.; Dillon, S.; Miller, J. T.; Suslick, K. S., Compression-Induced Deformation of Individual Metal-Organic Framework Microcrystals. *J. Am. Chem. Soc.* **2015,** 137, 1750-1753.

[54] Phan, A.; Doonan, C. J.; Uribe-Romo, F. J.; Knobler, C. B.; O'Keeffe, M.; Yaghi, O. M., Synthesis, Structure, and Carbon Dioxide Capture Properties of Zeolitic Imidazolate Frameworks. *Acc. Chem. Res.* **2010,** 43, 58-67.

[55] Ahmed, R. M.; Saif, M., Optical Properties of Rhodamine B Dye Doped in Transparent Polymers for Sensor Application. *Chin. J. Phys.* **2013,** 51, 511-521.

[56] Stobiecka, M.; Hepel, M., Multimodal Coupling of Optical Transitions and Plasmonic Oscillations in Rhodamine B Modified Gold Nanoparticles. *Phys. Chem. Chem. Phys.* **2011,** 13, 1131-1139.

[57] Khader, M. A., Lasing Characteristics of Rhodamine B and Rhodamine 6G as a Sensitizer in Sol–Gel Silica. *Opt. Laser Technol.* **2008,** 40, 445-452.

[58] Sagoo, S. K.; Jockusch, R. A., The Fluorescence Properties of Cationic Rhodamine B in the Gas Phase. *J. Photochem. Photobiol. A* **2011,** 220, 173-178.

[59] Ma, L.; Feng, X.; Wang, S.; Wang, B., Recent Advances in AIEgen-Based Luminescent Metal–Organic Frameworks and Covalent Organic Frameworks. *Mater. Chem. Front.* **2017,** 1, 2474-2486.

[60] Luo, J.; Xie, Z.; Lam, J. W.; Cheng, L.; Chen, H.; Qiu, C.; Kwok, H. S.; Zhan, X.; Liu, Y.; Zhu, D.; Tang, B. Z., Aggregation-Induced Emission of 1-Methyl-1,2,3,4,5-Pentaphenylsilole. *Chem. Commun.* **2001**, 1740-1741.

[61] Shustova, N. B.; McCarthy, B. D.; Dinca, M., Turn-on Fluorescence in Tetraphenylethylene-Based Metal-Organic Frameworks: an Alternative to Aggregation-Induced Emission. *J. Am. Chem. Soc.* **2011,** 133, 20126-20129.

[62] Shi, J.; Chang, N.; Li, C.; Mei, J.; Deng, C.; Luo, X.; Liu, Z.; Bo, Z.; Dong, Y. Q.; Tang, B. Z., Locking the Phenyl Rings of Tetraphenylethene Step by Step: Understanding the Mechanism of Aggregation-Induced Emission. *Chem. Commun.* **2012,** 48, 10675-10677.

[63] Zhao, Z.; Lam, J. W. Y.; Tang, B. Z., Tetraphenylethene: a Versatile AIE Building Block for the Construction of Efficient Luminescent Materials for Organic Light-Emitting Diodes. *J. Mater. Chem.* **2012,** 22, 23726–23740.

[64] Dong, J.; Shen, P.; Ying, S.; Li, Z.-J.; Yuan, Y. D.; Wang, Y.; Zheng, X.; Peh, S. B.; Yuan, H.; Liu, G.; Cheng, Y.; Pan, Y.; Shi, L.; Zhang, J.; Yuan, D.; Liu, B.; Zhao, Z.; Tang, B. Z.; Zhao, D., Aggregation-Induced Emission-Responsive Metal–Organic Frameworks. *Chem. Mater.* **2020,** 32, 6706–6720.

[65] Li, Q. Y.; Ma, Z.; Zhang, W. Q.; Xu, J. L.; Wei, W.; Lu, H.; Zhao, X.; Wang, X. J., AIE-Active Tetraphenylethene Functionalized Metal-Organic Framework for Selective Detection of Nitroaromatic Explosives and Organic Photocatalysis. *Chem. Commun.* **2016,** 52, 11284-11287.

[66] Yu, L.; Wang, H.; Liu, W.; Teat, S. J.; Li, J., Blue-Light-Excitable, Quantum Yield Enhanced, Yellow-Emitting, Zirconium-Based Metal–Organic Framework Phosphors Formed by Immobilizing Organic Chromophores. *Cryst. Growth Des.* **2019,** 19, 6850-6854.

[67] Zhang, Q.; Su, J.; Feng, D.; Wei, Z.; Zou, X.; Zhou, H. C., Piezofluorochromic Metal-Organic Framework: A Microscissor Lift. *J. Am. Chem. Soc.* **2015,** 137, 10064-10067.

[68] Yuan, H.; Wang, K.; Yang, K.; Liu, B.; Zou, B., Luminescence Properties of Compressed Tetraphenylethene: The Role of Intermolecular Interactions. *J. Phys. Chem. Lett.* **2014,** 5, 2968-2973.

[69] Li, S.; Luo, J.; Liu, J.; Tang, J., Self-Trapped Excitons in All-Inorganic Halide Perovskites: Fundamentals, Status, and Potential Applications. *J. Phys. Chem. Lett.* **2019,** 10, 1999-2007.

[70] Williams, R. T.; Song, K. S.; Faust, W. L.; Leung, C. H., Off-Center Self-Trapped Excitons and Creation of Lattice Defects in Alkali Halide Crystals. *Phys. Rev. B* **1986,** 33, 7232-7240.

[71] Menzel, D., Valence and Core Excitations in Rare Gas Mono- and Multilayers: Production, Decay, and Desorption of Neutrals and Ions. *Appl. Phys. A: Solids Surf.* **1990,** 51, 163-171.

[72] Scholz, R.; Kobitski, A. Y.; Zahn, D. R. T.; Schreiber, M., Investigation of Molecular Dimers in α-PTCDA by Ab Initio Methods: Binding Energies, Gas-to-Crystal Shift, and Self-Trapped Excitons. *Phys. Rev. B* **2005,** 72, 245208.

[73] Samanta, P.; Dutta, S.; Ghosh, S. K., Metal-Organic Frameworks for Detection and Desensitization of Environmentally Hazardous Nitro-Explosives and Related High Energy Materials. In *Metal-Organic Frameworks (MOFs) for Environmental Applications*, Ghosh, S. K., Ed. Elsevier, 2019, 231-283.

[74] Vullev, V. I.; Jiang, H.; JonesII, G., Excimer Sensing. In *Advanced Concepts in Fluorescence Sensing*, Geddes, C. D.; Lakowicz, J. R., Eds. Springer, 2005, 211-239.

[75] Gutierrez, M.; Sanchez, F.; Douhal, A., Spectral and Dynamical Properties of a Zr-Based MOF. *Phys. Chem. Chem. Phys.* **2016,** 18, 5112-5120.

[76] Takashima, Y.; Martinez, V. M.; Furukawa, S.; Kondo, M.; Shimomura, S.; Uehara, H.; Nakahama, M.; Sugimoto, K.; Kitagawa, S., Molecular

Decoding Using Luminescence from an Entangled Porous Framework. *Nat. Commun.* **2011,** 2, 1-8.

[77] Liu, Z.; Li, Q.; Zhu, H.; Lin, K.; Deng, J.; Chen, J.; Xing, X., 3D Negative Thermal Expansion in Orthorhombic MIL-68(In). *Chem. Commun.* **2018,** 54, 5712-5715.

[78] Ma, L.; Tan, K. J.; Jiang, H.; Kloc, C.; Michel-Beyerle, M. E.; Gurzadyan, G. G., Excited-State Dynamics in an Alpha-Perylene Single Crystal: Two-Photon- and Consecutive Two-Quantum-Induced Singlet Fission. *J. Phys. Chem. A* **2014,** 118, 838-843.

[79] Tange, M.; Okazaki, T.; Liu, Z.; Suenaga, K.; Iijima, S., Room-Temperature Y-type Emission of Perylenes by Encapsulation within Single-Walled Carbon Nanotubes. *Nanoscale* **2016,** 8, 7834-7839.

[80] Walker, B.; Port, H.; Wolf, H. C., The Two-Step Excimer Formation in Perylene Crystals. *Chem. Phys.* **1985,** 92, 177-185.

[81] Djikanovic, D.; Kalauzi, A.; Jeremic, M.; Micic, M.; Radotic, K., Deconvolution of Fluorescence Spectra: Contribution to the Structural Analysis of Complex Molecules. *Colloids Surf. B: Biointerfaces* **2007,** 54, 188-192.

Paper I: Dye-Encapsulated Zeolitic Imidazolate Framework (ZIF-71) for Fluorochromic Sensing of Pressure, Temperature, and Volatile Solvents

(Author contribution: Conceptualization - Y.Z. and J.-C.T.; methodology – Y.Z., A.K.C. and M.G.; investigation – Y.Z.; writing original draft – Y.Z.; writing review & editing – Y.Z., M.G., A.K.C., J.-C.T.; supervision – J.-C.T.)

ACS APPLIED MATERIALS & INTERFACES

www.acsami.org

Research Article

Dye-Encapsulated Zeolitic Imidazolate Framework (ZIF-71) for Fluorochromic Sensing of Pressure, Temperature, and Volatile Solvents

Yang Zhang, Mario Gutiérrez, Abhijeet K. Chaudhari, and Jin-Chong Tan*

Cite This: *ACS Appl. Mater. Interfaces* 2020, 12, 37477−37488

Read Online

ACCESS | Metrics & More | Article Recommendations | Supporting Information

ABSTRACT: Luminescent metal−organic frameworks (MOFs) offer a multifunctional platform for creating noninvasive sensors and tunable optoelectronics. However, fluorochromic materials that are photophysically resilient and show high sensitivity toward different physical and chemical stimuli are scarce. We report a facile host−guest nanoconfinement strategy to construct a fluorescent hybrid material with multiple sensing capabilities. We design and fabricate a new Guest@MOF material: comprising a zeolitic MOF (ZIF-71) as a nanoporous host for encapsulating rhodamine B (RhB dye) guest molecules, resulting in an RhB@ZIF-71 system with mechanochromic, thermochromic, and solvatochromic sensing response. The fluorochromic sensing properties stem from the nanoconfinement effect that ZIF-71 imposes on RhB monomers, yielding the H- or J-type aggregates with tunable photophysical and photochemical properties. For mechanochromism, the external pressure causes an emission red shift in a linear fashion, switching RhB guests from H-type to J-type aggregates through a shear deformation. For thermochromism, we demonstrate a linear scaling as a function of temperature due to the spatial restriction imposed on J-type aggregates incarcerated in ZIF-71 pores. Harnessing the solvatochromism of RhB@ZIF-71, we interrogated its photochemical response by employing three diverse groups of volatile organic compounds. The multimodal sensing response paved the way to smart applications like photonic pressure sensors, noninvasive thermometers, and ultrasensitive chemosensors.

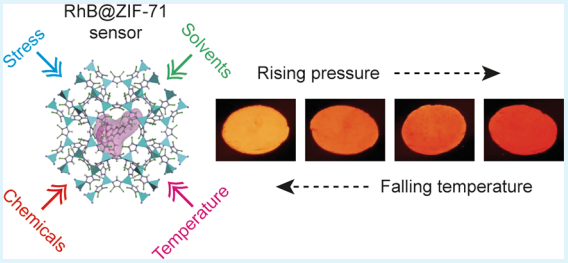

KEYWORDS: *hybrid materials, metal−organic frameworks, luminescence, guest−host interactions, photonic sensors*

1. INTRODUCTION

Research on the luminescent sensing abilities of metal−organic framework (MOF) materials and their composite systems is rapidly expanding because of their wide range of technological applications in nanophotonics, bio-imaging, and smart sensors.[1−4] Compared to other luminescent sensing materials such as metal complexes[5] and dye-based fluorescent probes,[6] crystalline MOF exhibits long-range periodicity, nanosized pores, combined with diverse chemical and structural versatility for tuning its vast physicochemical properties.[7] Among the many reported luminescent MOFs,[8] the study of Guest@MOF systems[9−14] composed of an MOF structure (the "host") to afford the encapsulation of luminescent molecules (the "guest") has attracted considerable attention. This is because the Guest@MOF composite can be achieved by an easy-to-synthesize or "off-the-shelf" MOF structure and commonly available fluorophores (luminescent dyes) to yield bespoke luminescent properties.[15−17] Additionally, the MOF hosts will act as a shield, protecting the guest against possible sources of degradation, like in the case of the encapsulation of the unstable fluorescent perovskite nanocrystals, which enhanced their robustness when confined within MOFs, paving the way to their integration into functional photonic devices.[18−20] Notably, the aforementioned approach could circumvent the need to rely on complex chemical designs to yield luminescent MOFs or to incorporate expensive rare-earth elements widely deployed in inorganic phosphors.[21]

The existing Guest@MOF approach faces a number of challenges. For example, the vast majority of Guest@MOF sensing mechanisms are based on the luminescence quenching effect where the analytes "switch off" the emission of the guest.[22−24] However, this mechanism might be susceptible to moisture exposure or temperature fluctuation in the environment, giving inaccurate readouts.[15,25] There are other Guest@MOF materials exhibiting luminescent sensing through a "turn-on" sensing[26] or luminescence color (fluorochromic) switching mechanism, but they often require very specific chemical interactions to function,[15] thus limiting multimodal applica-

Received: June 5, 2020
Accepted: July 23, 2020
Published: July 23, 2020

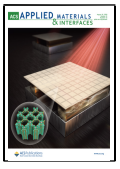

https://dx.doi.org/10.1021/acsami.0c10257
ACS Appl. Mater. Interfaces 2020, 12, 37477−37488

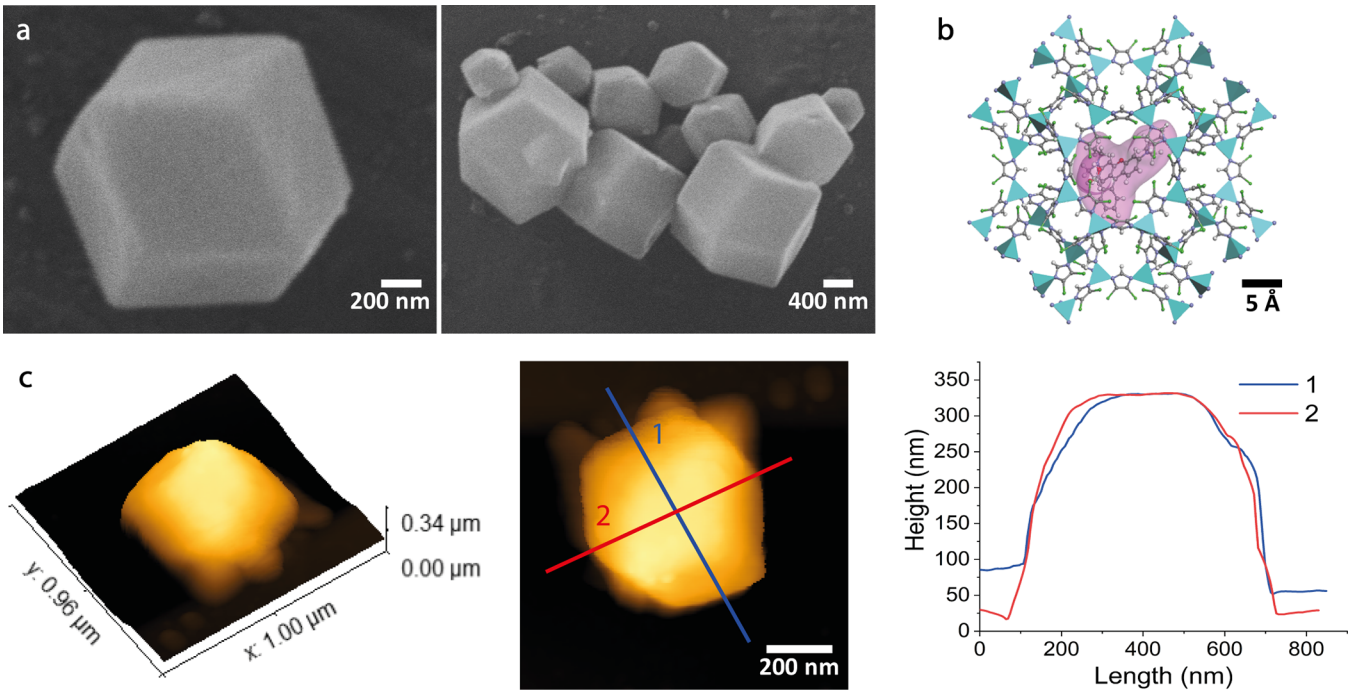

Figure 1. (a) SEM micrographs of the submicron-sized crystals of RhB@ZIF-71 exhibiting a rhombic dodecahedron habit. (b) Illustration of the Guest@MOF framework structure of RhB@ZIF-71 where the pore of the ZIF-71 host is used to confine the luminescent RhB guest (represented by the molecule with a red surface). From the pore spatial constraint, it can be deduced that two RhB molecules could occupy a unit cell of ZIF-71. Color scheme: ZnN_4 tetrahedron in cyan, nitrogen in dark blue, carbon in gray, hydrogen in white, chlorine in green, and oxygen in red. (c) AFM height topography and the corresponding cross-sectional profiles of a representative RhB@ZIF-71 crystal.

tions. To address some of the foregoing challenges, we propose that fluorochromic sensing can be achieved by using MOF pores to induce different caging effects on luminescent dye monomers and their aggregates, thereby producing a distinctive fluorescent behavior when subject to different physical and chemical stimuli.

In this study, we demonstrate a facile method to synthesize a multi-stimuli responsive Guest@MOF luminescent material by embedding the well-known fluorescent dye rhodamine B (RhB) into zeolitic imidazolate framework-71 (ZIF-71). Although a number of RhB@MOF systems have been reported,[27−34] there are certain limitations, such as the need to use complex synthesis steps, no control of RhB aggregates, inadequate understanding of the underlying mechanisms, and single-mode sensing functionality (basically, only solvatochromism). In contrast, our RhB@ZIF-71 not only shows solvatochromic response with its described mechanism far surpassing all reported examples[27−34] but also exhibits intriguing mechanochromic and thermochromic sensing properties that are unknown to date. We employed detailed photophysical characterization techniques to unravel the underpinning guest−host mechanisms controlling the performance of this new composite system. Our results also demonstrate proof-of-concept RhB@ZIF-71 applications, opening new pathways for the realization of multimodal fluorochromic sensing platforms.

2. RESULT AND DISCUSSION

2.1. Synthesis and Structure of the RhB@ZIF-71 System. The RhB@ZIF-71 system was synthesized through rapid mixing of a solution of zinc acetate with a solution of 4,5-dichloroimidazole (dcIm) and RhB at room temperature; the full details are given in the Experimental Section. Through this straightforward one-step reaction, we observe that the mixed solution was immediately converted from a transparent pink color to turbid, indicating the rapid formation of RhB@ZIF-71. As shown in Figure 1, the crystal size of RhB@ZIF-71 was found to be ∼800 nm by scanning electron microscopy (SEM) and atomic force microscopy (AFM). We also characterized the morphology of RhB@ZIF-71 at different reaction times (Figure S1, Supporting Information) and found that, after ∼10 min, a crystal size of ∼800 nm has formed. The rapid formation of such submicron-sized crystals is consistent with the previous reports on pure ZIF-71.[35]

Powder X-ray diffraction (PXRD) was carried out to verify the crystal structure. As shown in Figure 2a and Figure S2, the PXRD patterns of RhB@ZIF-71 with different RhB concentrations and pure ZIF-71 were consistent with the simulated XRD pattern of ZIF-71, indicating that the introduced guest (RhB) does not affect the structure of ZIF-71 significantly. However, when a very high concentration of RhB (0.5 mmol) was used, we observed the appearance of the (001) peak at $2\theta = 3.1°$ (Figure 2a, inset), while this peak was not obvious in the samples whose RhB concentrations are relatively low (0.01 and 0.05 mmol). Although the peak at $2\theta = 3.1°$ exists in the simulated pattern, its relative intensity is typically too low to be observed by XRD. Since a smaller 2θ value represents a larger crystal plane separation, the appearance of the (001) peak suggests that many ZIF-71 pores may contain more than one RhB molecule, thereby affecting the preferred orientation during crystal growth. Because the size of one RhB molecule is around 16.19 × 12.83 × 6.97 Å (including the van der Waals surface) and the minimum/maximum distance inside the ZIF-71 pore is 16.58/22.59 Å, it is conceivable that the crystal growth preference will be influenced when more than one RhB molecule is stacked together. This is further supported by the

https://dx.doi.org/10.1021/acsami.0c10257
ACS Appl. Mater. Interfaces 2020, 12, 37477−37488

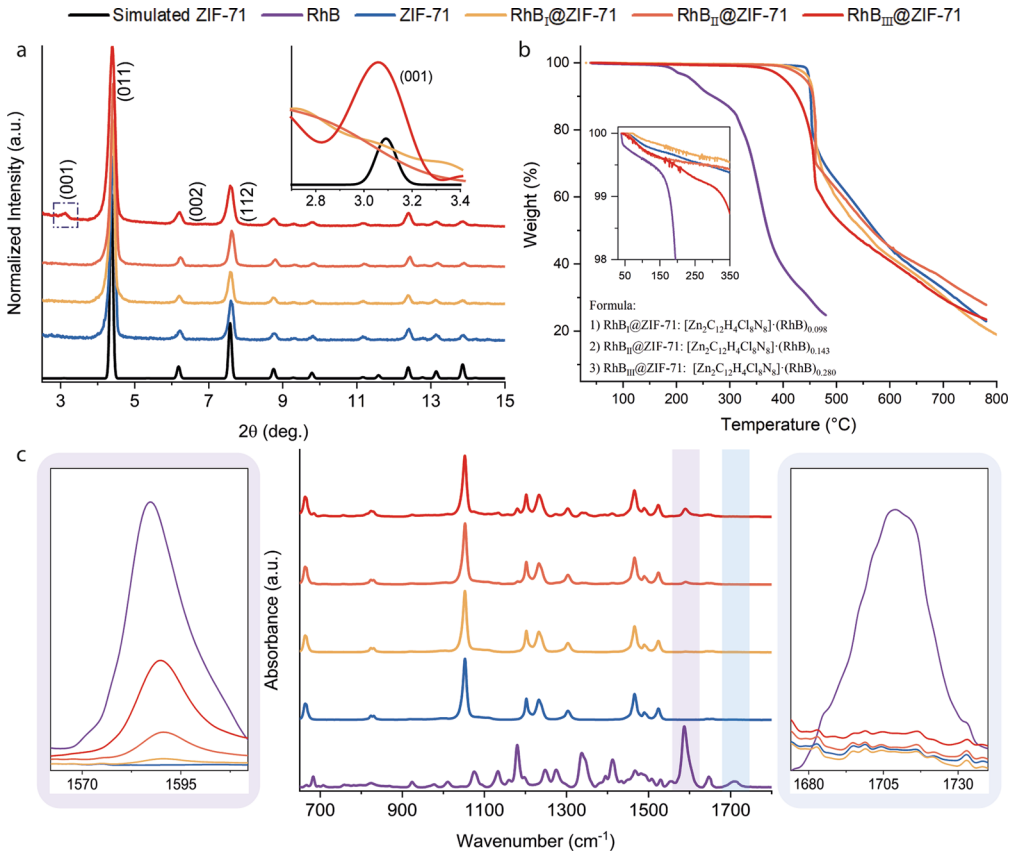

Figure 2. (a) Comparison of the XRD patterns of the simulated/synthesized ZIF-71 and RhB@ZIF-71 featuring three RhB concentrations. Inset: the (001) peak of simulated ZIF-71 is enlarged to compare with RhB$_{III}$@ZIF-71, while this peak is absent for both RhB$_I$@ZIF-71 and RhB$_{II}$@ZIF-71. The simulated pattern of ZIF-71 was generated from the crystallographic information file (CIF) obtained from the Cambridge Structural Database (CCDC code: GITVIP). (b) TGA and (c) ATR-FTIR results for ZIF-71, RhB, and RhB@ZIF-71. Subscripts I, II, and III designate the concentration of RhB used in the synthesis to be 0.01, 0.05, and 0.5 mmol, respectively. The method to determine the chemical formulae derived from TGA data is presented in Section S1.

results of thermogravimetric analysis (TGA) (Figure 2b) from which the determined chemical formula shows there was on average more than one RhB per pore.

Although we did not see the trace of RhB in the PXRD patterns (Figure S2), it was successfully detected by Fourier transform infrared spectroscopy with attenuated total reflection (ATR-FTIR) (Figure 2c), TGA (Figure 2b), and Raman vibrational spectroscopy (Figure S3). Figure 2b,c demonstrates that the concentration of RhB inside the RhB@ZIF-71 system gradually increases as the amount of RhB used in the synthesis was increased, as evidenced in the systematic rise of the ∼1590 cm^{-1} mode shown in the left inset of Figure 2c. Intriguingly, from the right inset of Figure 2c, we established that the peak at ∼1710 cm^{-1} attributing to the C═O vibrational mode of RhB has completely disappeared after confinement. Likewise, we detected similar phenomena in the Raman spectra (Figure S3). Vibrational spectroscopic data revealed that the C═O of RhB could interact with the zinc atoms of ZIF-71 or with its dcIm linkers. The TGA results (Figure 2b) not only enabled us to derive the chemical formula of RhB@ZIF-71 but also revealed the enhanced thermal stability of RhB when confined in the system; this finding supports the notion that RhB guests are residing in the pores of ZIF-71.

2.2. Luminescent Properties of the RhB@ZIF-71 System and Its Constituents. We begin by investigating the emission properties of the pristine crystals of ZIF-71 and its dcIm linker under room temperature, as depicted in Figure 3a,b. It can be seen in Figure S4 that the dcIm linker displays an intense and broadband emission in the solid state with an emission maximum at ∼468 nm (under a 360 nm UV excitation), which can be attributed to the $\pi^*-\pi$ transition.[36] From the emission map (Figure 3c) and the emission spectra (Figure S4) of ZIF-71, we established that ZIF-71 exhibits two emission peaks at around 456 and 559 nm. Because neither dcIm nor Zn(II) has an emission at 559 nm, the 559 nm emission of ZIF-71 could be from the ligand−metal charge transfer (LMCT), and the 456 nm emission comes from the linker itself in ZIF-71. Previous literature[37] mentioned that the LMCT process is usually expressed in MOF containing Zn(II), especially when the linker contains benzene derivatives, and MOFs often emit a green color fluorescence (500−565 nm) when LMCT occurs. Clearly, the structure and performance of ZIF-71 almost completely conform to this commonality, which supports our reasoning.

To confirm the aforementioned phenomena, we measured the emission lifetimes of dcIm (Table 1) and ZIF-71 (Table 2) employing the time-correlated single-photon-counting (TCSPC) technique. The most noticeable variation is when the observed wavelength changed from 450 to 558 nm (in Table 2); the c_3 of ZIF-71 dramatically increased, which we attribute to the effect of LMCT. However, it is not certain that τ_3 is the lifetime of LMCT because the τ_3 of dcIm itself is 4.44 ns (in Table 1), and after forming the ZIF-71 framework structure, theoretically, it will increase due to the caging

https://dx.doi.org/10.1021/acsami.0c10257
ACS Appl. Mater. Interfaces 2020, 12, 37477−37488

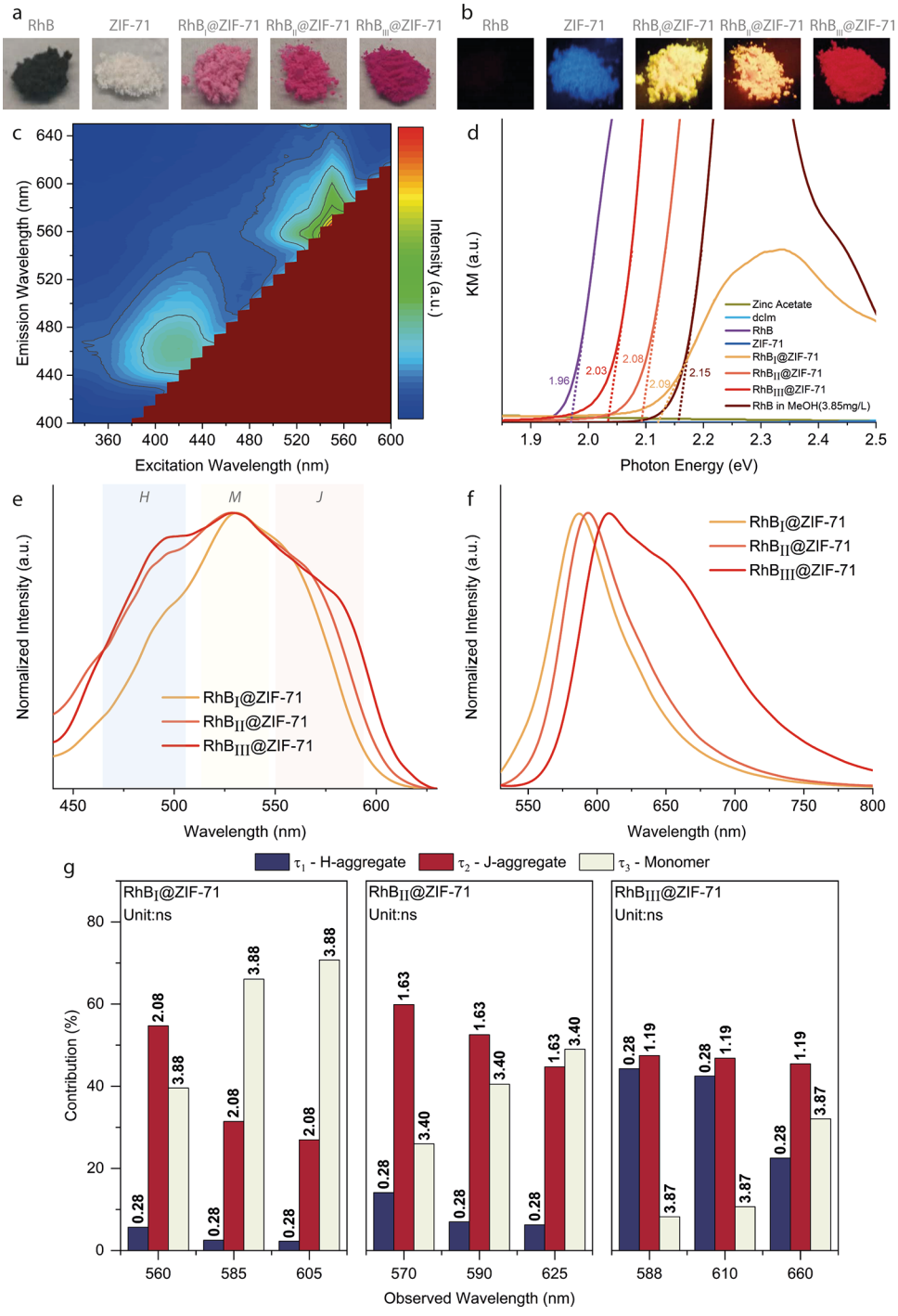

Figure 3. (a) RhB, ZIF-71, and RhB@ZIF-71 with different RhB concentrations seen in the visible light and (b) their luminescence under the 365 nm UV excitation. (c) Emission map of the ZIF-71 powder. (d) Kubelka−Munk (KM) function for estimating the band gaps based on the photon energy intercepts. (e) Normalized excitation spectra (measured under em@650 nm) and (f) the normalized emission spectra (measured under ex@515 nm). (g) Lifetime data of RhB@ZIF-71 obtained using three different RhB concentrations.

effect.[38] The increase in τ_3 of dcIm itself may be very close to the lifetime of the LMCT, which may cause the two to become indistinguishable. Thus, we consider that the τ_3 of dcIm itself and the lifetime of LMCT together constitute the τ_3 of ZIF-71.

Subsequently, we characterized the band gap (Figure 3d), solid-state excitation and emission spectra (Figure 3e,f), absorption (Figure S5) of RhB@ZIF-71, and the emission spectra (Figure S6) of pure RhB solution with different concentrations at room temperature. However, the emission of all the RhB@ZIF-71 powders is dominated by the guest itself (rather than simultaneously manifested by emissions of the guest and the LMCT of ZIF-71). The other possible interactions involving C═O with the zinc atoms or the linkers or the possible interaction between nitrogen atoms/the xanthene ring of RhB and the open metal sites/linker[39] may interrupt the LMCT process causing the single emission peak of RhB@ZIF-71. Of course, we do not rule out the possibility

https://dx.doi.org/10.1021/acsami.0c10257
ACS Appl. Mater. Interfaces 2020, 12, 37477−37488

Table 1. Values of Time Constants (τ_i), Normalized Pre-Exponential Factors (a_i), and Fractional Contributions ($c_i = \tau_i \cdot a_i$) of the Emission Decay of the Pristine dcIm Linker in a Solid State and in Methanol Solutions upon Excitation at 362.5 nm ($R_t = \Sigma a_i e^{(-t/\tau_i)}$, R_t is the Quantity/Counts at Time t)

dcIm	λ_{obs} [nm]	τ_1[ns]	a_1	c_1[%]	τ_2[ns]	a_2	c_2[%]	τ_3[ns]	a_3	c_3[%]	χ^2
solid state	470	0.36	0.041	11.89	1.76	0.038	53.95	4.44	0.010	34.16	1.052
0.0365 M	442	0.36	0.057	17.57	1.76	0.033	49.49	4.44	0.009	32.94	1.115
0.5 M	423	0.36	0.061	20.28	1.76	0.034	55.09	4.44	0.006	24.63	1.258
	443	0.36	0.060	18.80	1.76	0.037	55.64	4.44	0.007	25.55	1.082
	463	0.36	0.058	18.26	1.76	0.036	54.73	4.44	0.007	27.02	1.168

Table 2. Values of Time Constants (τ_i), Normalized Pre-Exponential Factors (a_i), and Fractional Contributions ($c_i = \tau_i \cdot a_i$) of the Emission Decay of the Pristine ZIF-71 Powder upon Excitation at 362.5 nm

ZIF-71	λ_{obs} [nm]	τ_1[ns]	a_1	c_1[%]	τ_2[ns]	a_2	c_2[%]	τ_3[ns]	a_3	c_3[%]	χ^2
solid state	450	0.58	0.049	26.43	2.11	0.029	57.24	5.61	0.003	16.32	1.150
	558	0.58	0.041	14.74	2.11	0.026	34.50	5.61	0.015	50.76	1.215

that the emission of the ZIF-71 host could not be observed due to its relatively low quantum yield (Table S1).

In terms of their emission spectra (Figure 3f), it is shown that the bathochromic (red) shift was detected when the concentration of RhB increased. We propose that one of the reasons for this red shift is related to the formation of more RhB aggregates. Because of the relative dimensions of RhB molecules and ZIF-71 pores, the XRD results (Figure 2a) and the chemical composition derived from TGA results (Figure 2b) suggest that more than one RhB molecule may occupy the pore of ZIF-71. It follows that more RhB introduced during synthesis will lead to more aggregates. In principle, both of H-type (head-to-head) and J-type (head-to-tail) aggregates of RhB are able to form during the synthesis.[40,41] Since the emission of H-type aggregates is theoretically forbidden and the emission of J-type aggregates is allowed but with a longer wavelength,[42] we could observe the red shift. This idea is confirmed by the excitation spectra in Figure 3e. It can be seen that there are three excitation areas: humps at around 495 nm, peaks at 531 nm, and shoulders located between 552 and 590 nm. Using Kasha's exciton model,[42] we assigned the humps to H-type aggregates, peaks to RhB monomers, and the shoulders to J-type aggregates. Compared with the peaks (~531 nm), the intensity of the humps (~495 nm) increased so it follows that the amount of aggregates increased when a higher concentration of RhB was used during synthesis. The reason why the shoulders (552−590 nm) did not increase is explained below.

Comparing the variation of H-type and J-type aggregates, we found that the excitation peaks of the J-type aggregates showed a red shift as the concentration of RhB increases, while the H-type did not show a blue shift. This difference arises because the J-type aggregates have a longer spatial dimension than the H-type aggregates,[41] which might allow the J-type aggregates to interact with another J-type aggregate in adjacent pores. Our group has reported that perylene@ZIF-8 also showed a similar phenomenon in which perylene and 2-methylimidazole can form an energy transfer pathway through the adjacent pores.[43] Likewise, other researchers have demonstrated the preparation of long-range crystalline MOFs by mechanochemistry under solid conditions,[44,45] which means that chemical reactions can occur between solid crystals. On this basis, weak interactions involving J-aggregate interaction across the pores are plausible. Moreover, because the maximum size of the ZIF-71 window aperture is 5.08 Å, which is spatially larger than some parts of the RhB molecules (e.g., the distance of C−C on the xanthene ring is 4.79 Å), we suggest that part of the J-type aggregates may protrude out of the ZIF-71 window, which will strengthen the interaction by bridging the pores. In contrast, the packing of H-type aggregates is tighter, and the occupied space is relatively small,[41] allowing them to be better confined inside the pores and less likely to interact with guests in adjacent pores. Hence, when the concentration of RhB used in the synthesis was increased, it will cause more J-type aggregate-based interactions (bridging the pores) in the RhB@ZIF-71 system, which leads to a smaller band gap (Figure 3d). This is another reason for the observed red shift in the emission and the reason behind the declining intensity of the emission shoulders (552−590 nm in Figure 3e).

To further study the formation of aggregates and analyze their luminescent properties, the emission lifetimes of pure RhB and RhB@ZIF-71 were measured by the TCSPC technique. For pure RhB in MeOH solution (0.0001 M), the lifetime is 2.93 ns, and for all the RhB@ZIF-71 powders, we obtained three decay times, as summarized in Figure 3g (see also Table S2 and Figure S7). We propose that τ_1 can be assigned to the H-type aggregates, τ_2 corresponds to the J-type aggregates, and τ_3 is due to the RhB monomers. First, it can be seen that τ_3 is greater than 2.93 ns, which also is evidence that RhB is residing inside the pore because the vibration of RhB monomers confined in the pore becomes restricted (i.e., caging effect), greatly reducing their nonradiative decay and thus increasing the lifetime. Second, it can also be seen that, as the RhB concentration increases, the values of a_1 and c_1 rose, while a_3 and c_3 fell (Table S2), which indicates an increase in the content of H-type aggregates and a relative decrease in the monomer content. Third, τ_2 was found to decrease as the RhB concentration increases; this supports the notion that the J-type aggregates could interact with each other across the adjacent pores. This kind of interaction can also be proven by comparing a_2 and c_2 (Table S2). As the observed wavelength (λ_{obs}) increases, the magnitude of the change in a_2 and c_2 decreases, which results in more interactions and hence broadening of the emission component of the J-type aggregation. However, comparing the changes in a_1, c_1, a_2, and c_2, we can see that the increase of J-type aggregates is not as high as the H-type aggregates. Given the space limitation of the ZIF-71 pore, the larger J-type aggregates are harder to form than the H-type. Herein, the lifetime data have substantiated the previous inferences obtained from the emission and excitation spectrum.

https://dx.doi.org/10.1021/acsami.0c10257
ACS Appl. Mater. Interfaces 2020, 12, 37477−37488

The quantum yields of RhB_I@ZIF-71, RhB_{II}@ZIF-71, and RhB_{III}@ZIF-71 were characterized, and the results are summarized in Table 3.

Table 3. Quantum Yield of RhB@ZIF-71 with Different RhB Concentrations

	QY[a] [%]		QY[b] [%]	
sample	ex@485 nm	ex@525 nm	ex@485 nm	ex@525 nm
RhB_I@ZIF-71	23.99	28.25	35.43	39.53
RhB_{II}@ZIF-71	13.74	14.15	17.51	18.30
RhB_{III}@ZIF-71	1.68	1.85	2.32	3.31

[a]Samples were directly measured. [b]Samples (10 wt %) were first mixed with $BaSO_4$ (90 wt %) and then measured.

2.3. Mechanochromic Sensing Response. To study the mechanochromism of the RhB@ZIF-71 system, the RhB_{II}@ZIF-71 material was chosen and compressed into pellets under different pressures. Figure 4a,b depicts the color of the pellets viewed under daylight and their emissions when subject to a 365 nm UV excitation, respectively. Here, we focus on the RhB_{II}@ZIF-71 pellets because the RhB_{III}@ZIF-71 has a relatively low quantum yield (Table 3), while the emission of the RhB_I@ZIF-71 pellets (Figure S8) is not as linear as RhB_{II}@ZIF-71. Figure 4d and Figure S9b reveal that the emission spectra of these pellets red-shifted as the pressure was systematically increased up to ~350 MPa, demonstrating a very linear relationship that is highly desirable for stress sensing applications (Figure 4f).

Combined with the excitation spectra (Figure 4c and Figure S9a), the lifetime data (Figure 4g and Figure S10 and Table S3), and the PXRD patterns (Figure 4e and Figure S11) of the pellets, we investigate the reason for the observed red shift in the emission. On the one hand, it can be seen that the excitation peaks of J-type aggregates (575−590 nm) showed a red shift with increasing pressure, and in the PXRD pattern (Figure 4e and Figure S11), it can be seen that the pressure has caused some amorphization of the ZIF-71 structure. These results suggest that the pelleting pressure leads to the mechanical deformation of the ZIF-71 structure where framework distortion will cause the tighter packing of aggregates and make the adjacent pores to come closer, causing stronger interactions inside the pores and promoting stronger interactions between the J-type aggregates across adjacent pores. Together, these factors result in a red shift. In principle, the stronger the interaction, the shorter the luminescent lifetime becomes,[46] but the τ_2 in Figure 4g did not decrease. This is because RhB aggregates are present in the pores of ZIF-71, and hence, the pore shrinkage from mechanical stress introduces a stronger caging effect, suppressing the nonradiative decay and preventing the decrease of lifetime. Based on this hypothesis, it is easy to understand the increase of the monomer's lifetime inside the pores (τ_3), which is dependent only upon the caging effect.

On the other hand, we consider that the red shift of the emission is also related to the increase in the relative content of the J-type aggregates. Table S4 shows that the RhB@ZIF-71 pellets had a smaller FWHM (full width at half-maximum) than the ZIF-71 pellets under pressure, which means that the RhB@ZIF-71 pellets possess a higher crystallinity than ZIF-71 (Figure S12) and reveals that the encapsulated guests can mechanically enhance the structural stability of the overall framework under stress. Therefore, we propose the reason why a_3 and c_3 in Table S3 started to drop significantly at a relatively low pressure, a_1 and c_1 rose first and then fell, and a_2 and c_2 continuously increased is that the pores containing monomers are initially destroyed to form new H-type and J-type aggregates at a relatively low pressure. Subsequently, as the pressure keeps rising, the ZIF-71 crystals continue to deform under shear deformation,[47] causing the aggregates to transform from H-type to J-type (Scheme 1). Moreover, in the excitation spectra of the RhB_{II}@ZIF-71 pellets (Figure 4c), the intensity of the H-type aggregates first rose and then fell, but the peak position of H-type aggregates (450−506 nm) is always blue-shifted with increasing pressure, which also supports this hypothesis.

2.4. Thermochromic Sensing Response. RhB@ZIF-71 exhibits thermochromic behavior as a function of temperature; here, we use RhB_{II}@ZIF-71 as an example to explain the underlying mechanism. Figure 5a,b shows the excitation and emission spectra from room temperature to 200 °C, respectively. As shown in Figure 5 and Figure S13, the luminescent intensity of RhB@ZIF-71 decreases, accompanied by a red shift with increasing temperature. The decrease in intensity is very similar to the performance of pure RhB itself in solution at different temperatures,[48,49] which is due to the increase in a nonradiative decay rate. In the previous research,[48] the temperature range of this kind of intensity decrease of RhB was generally from 5 to 80 °C. Above this temperature range, the luminescent intensity of RhB was too low to be detected accurately. Remarkably, we demonstrate that the nonradiative decay of RhB was greatly reduced due to the caging effect of ZIF-71; not only overcoming the restriction that thermochromism of RhB can only be achieved in solutions, but our solid-state system also significantly extends the operational temperature range by at least a factor of 2 (Figure 5d). Figure S13d shows that, when the temperature rises from 200 to 250 °C, RhB@ZIF-71 experienced a relatively large red shift, which can be attributed to the thermal decomposition of RhB itself beyond 200 °C (consistent with TGA results in Figure 2b).

By analyzing the temperature range from room temperature to 200 °C, we established that there is a linear scaling relationship between the red shift of the emission peak and the temperature increment (Figure 5d); this effect is highly attractive for photonics-based thermometry applications. Note that the red shift of RhB in the solid state observed here is as yet unreported in the literature, unlike for pure RhB solutions in which the increase in temperature has produced no red shift.[48] The normalized excitation spectra (Figure 5a) reveal that, in this linearly changing region (room temperature to 200 °C), the relative intensity of H-type aggregates and monomers did not change much with the increase of temperature, while the J-type aggregates showed a relatively large intensity enhancement at high temperatures (i.e., 150 and 200 °C). Since the crystal structure of RhB@ZIF-71 can withstand a temperature of up to 250 °C (evidenced from the XRD patterns in Figure 5c and Figure S13e), we reason that the different spatial sizes between the H- and J-type aggregates and its monomers determine the trend of their intensity and wavelength change.

As discussed above, H-type aggregates and monomers possess smaller size than J-type aggregates, so the J-type aggregates will experience a stronger caging effect, therefore becoming less sensitive to temperature variation. In other

https://dx.doi.org/10.1021/acsami.0c10257
ACS Appl. Mater. Interfaces 2020, 12, 37477−37488

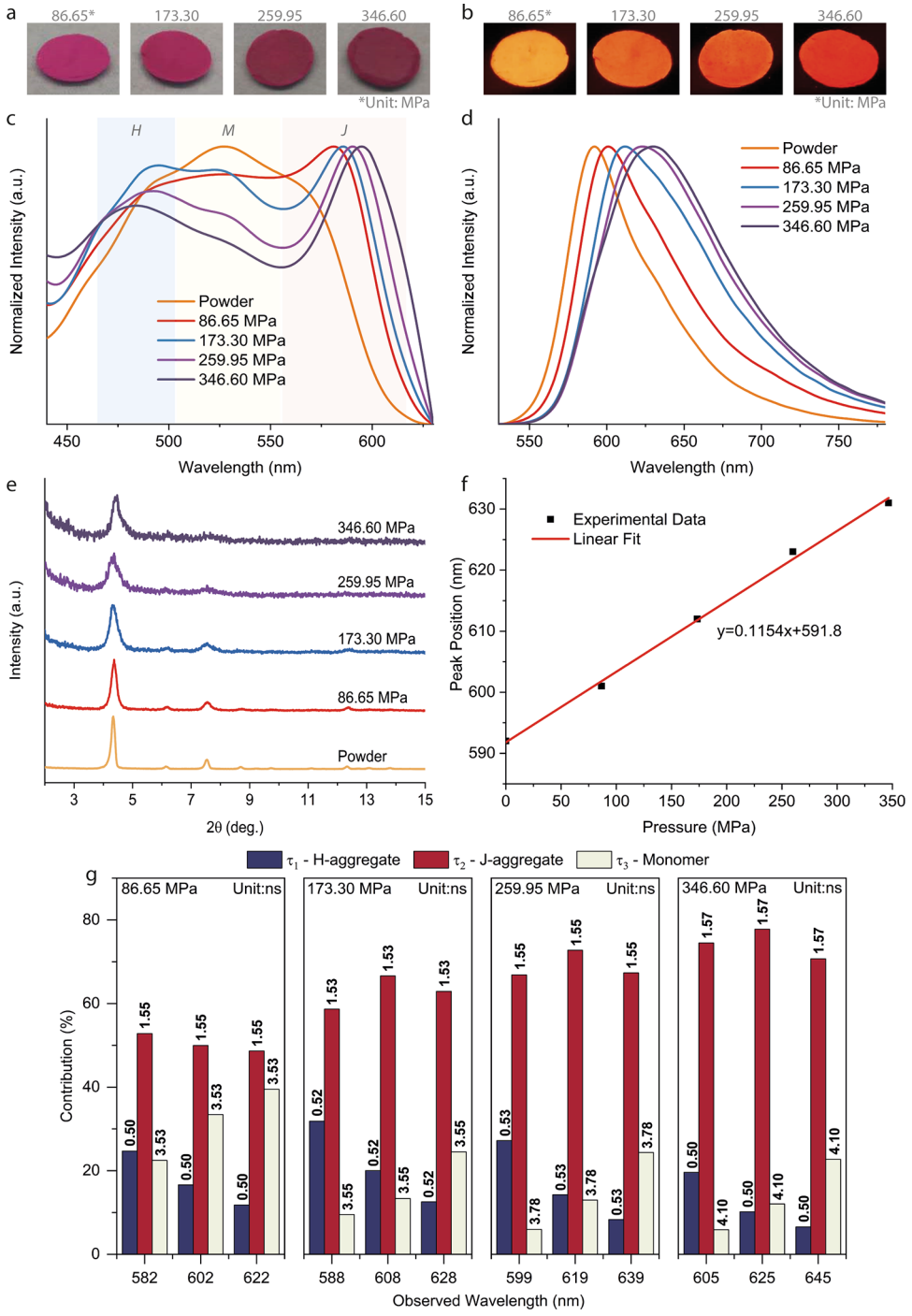

Figure 4. (a) RhB_{II}@ZIF-71 pellets prepared using different pelleting pressures, their colors viewed in visible light, and (b) their luminescence under the 365 nm UV excitation. (c) Normalized excitation spectra (measured under em@650 nm) and (d) normalized emission spectra (measured under ex@515 nm) of the RhB_{II}@ZIF-71 pellets. (e) XRD of the RhB_{II}@ZIF-71 pellets. (f) Linear relationship between the emission peak wavelength and the applied pressure for RhB_{II}@ZIF-71. (g) Lifetime data of RhB_{II}@ZIF-71 pellets showing the contributions from the monomer, H-aggregates, and J-aggregates.

words, when temperature rises, the excitation intensity of J-type aggregates decreases less than that of H-aggregates and monomers. It is this effect that causes the red shift observed in the emission peak. Additionally, at high temperatures, it can be seen that the excitation peaks of the H-type and J-type aggregates showed a very small degree of red and blue shifts, respectively, but the peaks associated with the monomers remain unchanged. This indicates that both H-type and J-type aggregates slightly expand at high temperatures, thereby weakening the interactions within themselves. The absence of any variation to the excitation peaks of monomers reveals that the interactions between RhB and ZIF-71 are weak or negligible. Likewise, in the mechanochromism studies, we note that the peak wavelength of the monomer also did not change when subject to mechanical stress (Figure 4c), which also indicates that the interactions are weak or negligible.

2.5. Solvatochromic Sensing Response. Another promising property of RhB@ZIF-71 is its solvatochromic

https://dx.doi.org/10.1021/acsami.0c10257
ACS Appl. Mater. Interfaces 2020, 12, 37477−37488

Scheme 1. Proposed Deformation of the RhB@ZIF-71 Subject to a Mechanical Pressure[a]

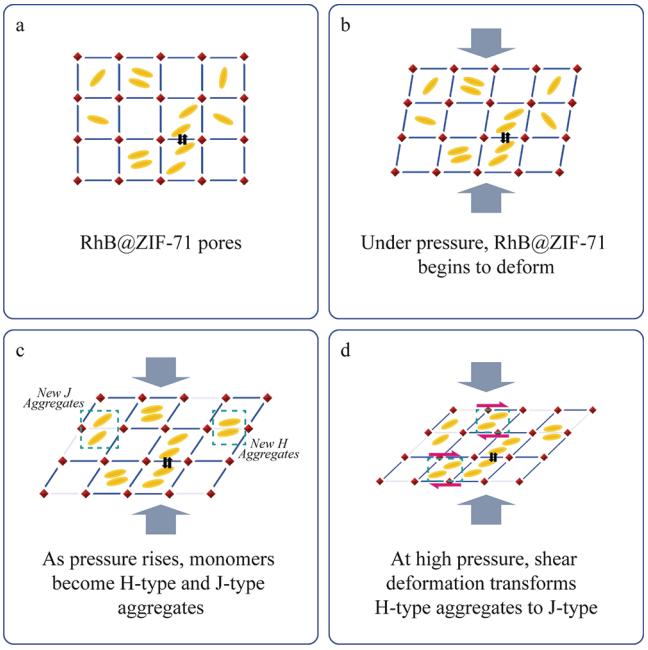

[a]Red nodes and blue rods represent the ZnN_4 coordination environment and the dcIm linker, respectively. Yellow ellipses represent the RhB guest molecules within the pore of the ZIF-71 host. (a) Possible interactions between J-aggregates are denoted by a pair of black arrows. (b, c) Illustration of how the structural distortion under pressure causes the formation of new H- and J-type aggregates. The gray rods represent the broken linkers under pressure. (d) Due to shear deformation (denoted by antiparallel pink arrows), the majority of the H-type aggregates transform into the J-type.

response, as shown in Figure 6 and Figure S14. To understand the subtle changes of emission due to solvatochromism, we chose the RhB_1@ZIF-71 system, which has the lowest RhB concentration. We observed that the peak intensity and peak position of RhB_1@ZIF-71 were distinctively different when exposed to different solvents. To explain this phenomenon, we propose that this solvatochromic response is linked to the nature of RhB itself. Because RhB can exist in three different forms in the solution state (i.e., lactone, zwitterion, and cation),[48] the lactone has no color under visible light or UV, while the zwitterion and cation have luminescence but their emission wavelength and intensity are different. Generally, polar protic solvents can stabilize the zwitterion[48] and therefore will give an intense luminescence. Meanwhile, in highly polar aprotic solvents, such as dimethylformamide (DMF), RhB has no luminescence due to the complete conversion to lactone, and in less polar aprotic solvents, such as acetonitrile (ACN), it can show luminescence.[49] Thereby, RhB is solvatochromic,[48,50] and we propose that this is also the basis for the solvatochromism observed in the RhB@ZIF-71 system.

However, after confinement within ZIF-71, we found that the luminescence of RhB@ZIF-71 is greatly enhanced compared with the pure RhB (Figure S14). Notably, pure RhB has poor solubility or it is simply insoluble in many nonpolar solvents. For example, in this study, we tested toluene, hexane, and cyclohexane and confirmed that there was no luminescence in these hydrocarbons due to the aforementioned limitations. Conversely, we discovered that the RhB@ZIF-71 crystals exhibit good dispersion and luminescence (Figure S14 and Figure 6) in hexane and also in cyclic hydrocarbons (e.g., toluene and cyclohexane), thereby demonstrating a sensing property previously not achievable by pure RhB alone. To date, most of the RhB@MOF studies[27−34] have focused on the field of solvatochromism, and many of these systems possess a similar sensing behavior. However, almost all the authors attributed this kind of sensing to different solvents that affect the energy transfer between the MOF they used and RhB and lack of in-depth understanding of the emission wavelength change. Moreover, their theory is also unable to satisfactorily explain the luminescence of RhB@MOF systems in some highly polar aprotic solvents because no matter how the energy transfer occurs, when RhB turns into the lactone in strong polar aprotic solvents, in principle, the luminescence of the systems will be largely deteriorated.

Here, our systematic analysis of RhB@ZIF-71 based on the new confinement strategy provides new insight into the complex solvatochromism of RhB@MOF systems, as can be seen in Figure 6d. All RhB@ZIF-71 samples in polar aprotic solvents exhibit a longer wavelength accompanied by a reduced intensity than in polar protic solvents. Remarkably, compared with the poor luminescence of RhB in highly polar aprotic solvents, the introduction of ZIF-71 greatly improves the luminescence of RhB (Figure S14). This phenomenon can be explained *via* the concept of aggregates we introduced above. When the pores of ZIF-71 contain monomers, there is enough room for the monomers to contact the aprotic solvent molecules to convert to lactone; when the pores contain aggregates (especially the J-type), it is likely that the remaining space in the pores cannot accommodate the solvent molecules. In other words, the ZIF-71 (host) can protect or shield the aggregates from direct exposure to the solvent molecules. On this basis, compared with the protic solvents, much more monomers inside the ZIF-71 pores converts to the colorless lactone in aprotic solvents, but the luminescence of aggregates is better protected. Consequently, RhB@ZIF-71 in polar aprotic solvents can exhibit luminescence with a longer wavelength and relatively lower intensity. This is the reason why RhB@ZIF-71 can show a better luminescence and sensing performance than pure RhB alone. Additionally, our interpretation can also be confirmed by observing the luminescent response of the RhB@ZIF-71 subject to polar protic solvents (Figure S14c), e.g., methanol (MeOH), ethanol (EtOH), and isopropanol (IPA) because Figure S14c reveals that the emission wavelength of RhB@ZIF-71 changes less than pure RhB, especially for IPA, which again can be attributed to the ZIF-71's protection of the RhB aggregates.

3. CONCLUSIONS

In summary, through a facile guest−host nanoconfinement strategy performed under ambient conditions, we demonstrate the encapsulation of fluorescent RhB monomers (or switchable aggregates) caged within the pores of ZIF-71. The new RhB@ZIF-71 system not only allows RhB to easily yield luminescence in the solid state but also provides remarkable mechanochromism, thermochromism, and solvatochromism properties that are not achievable to date by a traditional use of RhB dispersion in the liquid state or indeed by any other means of RhB@MOF systems known thus far. Above all, in the process of analyzing mechanochromism, thermochromism, and solvatochromism, we found several unique mechanisms

https://dx.doi.org/10.1021/acsami.0c10257
ACS Appl. Mater. Interfaces 2020, 12, 37477−37488

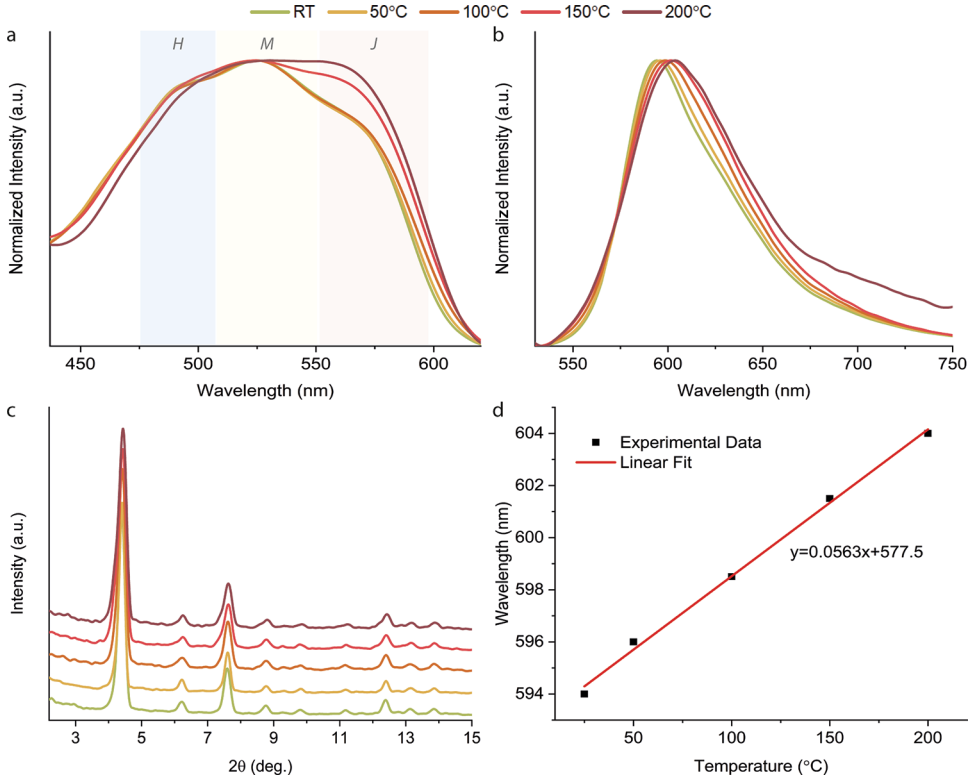

Figure 5. (a) Normalized excitation spectra (measured under em@650 nm) and (b) normalized emission spectra (measured under ex@365 nm) of RhB@ZIF-71 at different temperatures. (c) XRD patterns of RhB@ZIF-71 pellets after being tested at different temperatures. (d) Linear relationship of the emission peak wavelength as a function of temperature for RhB@ZIF-71.

summarized below. (i) Under mechanical stress, the RhB@ZIF-71 crystals deform by shear causing the conversion of H-type aggregates into J-type aggregates inside the MOF pores, giving rise to pressure sensing. (ii) The J-type aggregates are less affected by temperature due to the strong caging effect provided by the ZIF-71 pores, resulting in the red shift of emission in a very linear fashion, giving rise to noninvasive temperature sensing. (iii) The protective effect of ZIF-71 pores reduces the influence that solvents have on the RhB aggregates, leading to solvatochromic sensing of volatile organic compounds—previously undetected by unconfined RhB dyes alone.

Our RhB@ZIF-71 nanoconfinement strategy demonstrates the concept of a Guest@MOF system with multimodal fluorescent sensing response, presenting a new platform for the design of smart luminescent sensors. Moreover, we show that the exploitation of luminescent aggregates confined in MOF pores studied through the characterization of excitation spectrum combined with the luminescent lifetime data is a powerful approach for understanding the mechanisms of novel fluorochromic materials like the dye-encapsulated composite exemplified in this study.

4. EXPERIMENTAL SECTION

4.1. Synthesis of RhB@ZIF-71. A 90 mL methanol clear solution of 2.40 mmol of zinc acetate was rapidly poured into a 90 mL methanol solution of 9.60 mmol of dcIm and different amounts of RhB (I, 0.01 mmol; II, 0.05 mmol; III, 0.5 mmol) under stirring. The mixed solution immediately changed from clear to turbid. After 24 h of stirring at room temperature, the sample was centrifuged at 8000 rpm to remove the excess reactants and subsequently washed twice with methanol (the sample was first put into methanol followed by sonication for 10 min, and then, the product was separated by centrifugation) to remove the excess reactants and any RhB adhered on the surface of ZIF-71. We observed that, for the RhB_I@ZIF-71 (0.01 mmol) and RhB_{II}@ZIF-71 (0.05 mmol) samples, the methanol became clear after the second washing cycle, indicating the negligible loss of RhB guest molecules from the ZIF-71 host. Conversely, the RhB_{III}@ZIF-71 (0.5 mmol) sample has RhB molecules that remained on the surface after two or more washing cycles, as evidenced from the pink color of the methanol solvent after multiple washes. The latter indicates surface adhesion of RhB molecules when a high concentration of the guest was being introduced during the synthesis step.

The procedure for preparing ZIF-71 was the same, except no RhB was added during the synthesis process.

4.2. Sample Preparation for Fluorochromic Characterization. For mechanochromism, the powders were pressed into pellets by using manual hydraulic pressure equipment with a 1 cm diameter die under forces of 1, 2, 3, and 4 tonnes. For thermochromism, no extra preparation was required. For solvatochromism, a concentration of 1 mg of RhB@ZIF-71 in 20 mL of solvents was chosen to avoid the negative influence of too intense emission. Then, to compare the performance of pure RhB and RhB@ZIF-71 in different solvents, several different concentrations of RhB-MeOH solutions were tested, and a concentration of 7.5×10^{-6} M was selected at which the emission peak wavelength of pure RhB was identical to that of 1 mg of RhB@ZIF-71 in 20 mL of MeOH. Subsequently, the solutions of pure RhB in different solvents were also formulated at this concentration.

4.3. Materials Characterization. The structures and morphologies were examined under scanning electron microscopy (SEM; Carl Zeiss EVO LS15) and atomic force microscopy (AFM; Veeco Dimension 3100). An FS-5 spectrofluorometer (Edinburgh Instruments) was used to characterize the steady-state emission, excitation spectra, QY, CIE 1931, and lifetime measurements (more details are described in the Supporting Information). FTIR and Raman results were recorded by using a Nicolet iS10 FTIR spectrometer and a MultiRam FT-Raman spectrometer (Bruker), respectively. A UV-

https://dx.doi.org/10.1021/acsami.0c10257
ACS Appl. Mater. Interfaces 2020, 12, 37477−37488

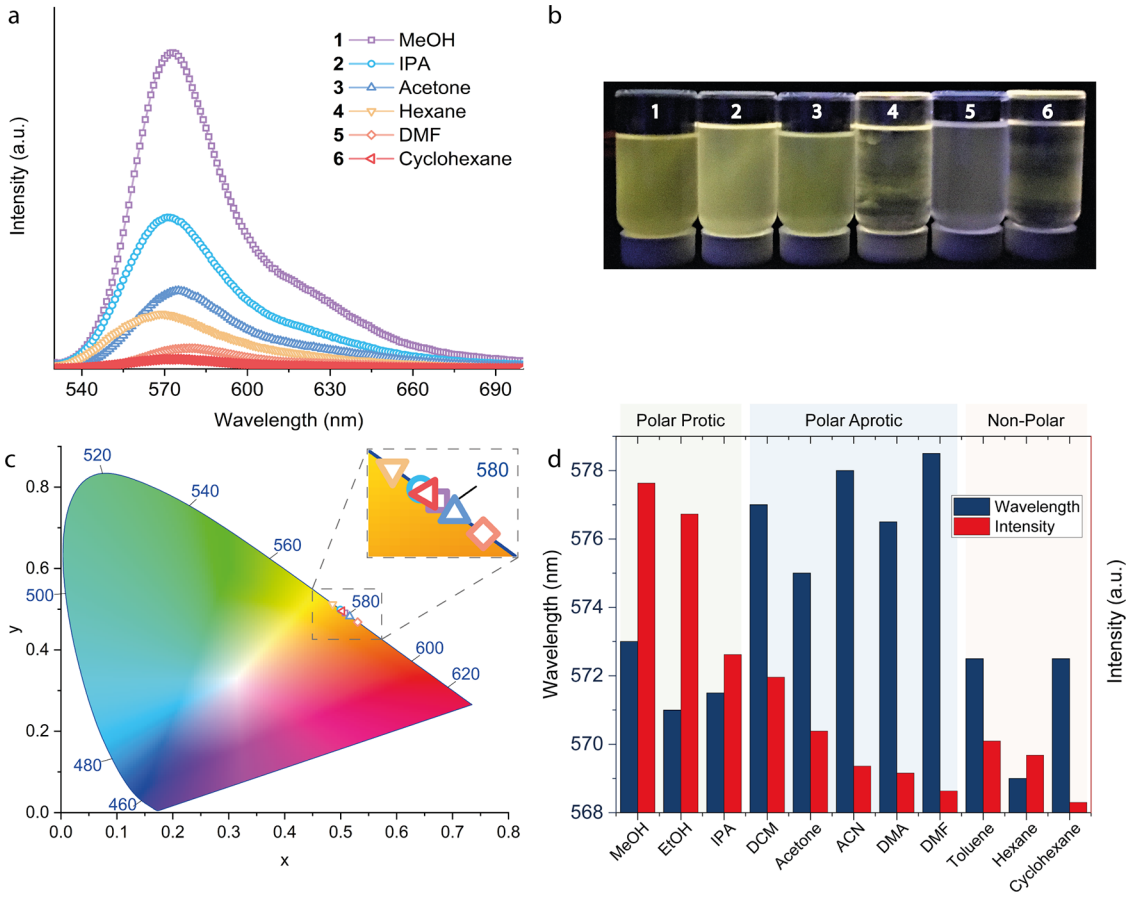

Figure 6. (a) Emission spectra (ex@525 nm) of RhB_1@ZIF-71 when exposed to different volatile organic compounds (VOCs). (b) Solvatochromism observed under the 365 nm UV excitation where the concentration ratio used was 1 mg of RhB_1@ZIF-71 dispersed in 20 mL of the solvent. (c) Color variation presented on the CIE 1931 chromaticity diagram. (d) Change in the emission wavelength and peak intensity of RhB@ZIF-71 when tested in a wide range of polar protic, polar aprotic, and nonpolar solvents.

2600 UV−vis spectrophotometer (Shimadzu) was used to measure the absorption spectra and calculate the Kubelka−Munk (KM) function. The PXRD pattern was recorded using a Rigaku MiniFlex with a Cu Kα source (1.541 Å). TGA was performed using a TGA-Q50 machine (TA Instruments) equipped with a platinum sample holder under an N_2 inert atmosphere at a heating rate of 10 °C/min from 50 to 800 °C.

■ ASSOCIATED CONTENT

Supporting Information

The Supporting Information is available free of charge at https://pubs.acs.org/doi/10.1021/acsami.0c10257.

Analysis to estimate the chemical formula of RhB@ZIF-71, SEM images, X-ray diffraction patterns and crystallinity analysis, Raman spectra, excitation−emission spectra, lifetime emission spectra, spectrofluorometer characterization techniques, and a physically mixed sample of {RhB + ZIF-71} (PDF)

■ AUTHOR INFORMATION

Corresponding Author

Jin-Chong Tan − *Multifunctional Materials & Composites (MMC) Laboratory, Department of Engineering Science, University of Oxford, Oxford OX1 3PJ, U.K.;* orcid.org/0000-0002-5770-408X; Email: jin-chong.tan@eng.ox.ac.uk

Authors

Yang Zhang − *Multifunctional Materials & Composites (MMC) Laboratory, Department of Engineering Science, University of Oxford, Oxford OX1 3PJ, U.K.;* orcid.org/0000-0002-6433-3643

Mario Gutiérrez − *Multifunctional Materials & Composites (MMC) Laboratory, Department of Engineering Science, University of Oxford, Oxford OX1 3PJ, U.K.*

Abhijeet K. Chaudhari − *Multifunctional Materials & Composites (MMC) Laboratory, Department of Engineering Science, University of Oxford, Oxford OX1 3PJ, U.K.*

Complete contact information is available at: https://pubs.acs.org/10.1021/acsami.0c10257

Notes

The authors declare no competing financial interest.

■ ACKNOWLEDGMENTS

We thank the Research Complex at Harwell (RCaH) for access to advanced materials characterization facilities. J.-C.T., M.G., and A.K.C. thank the ERC Consolidator Grant under the grant agreement 771575 (PROMOFS) for supporting the research.

■ REFERENCES

(1) Stassen, I.; Burtch, N.; Talin, A.; Falcaro, P.; Allendorf, M.; Ameloot, R. An Updated Roadmap for the Integration of Metal-

Organic Frameworks with Electronic Devices and Chemical Sensors. *Chem. Soc. Rev.* **2017**, *46*, 3185−3241.
(2) Lustig, W. P.; Mukherjee, S.; Rudd, N. D.; Desai, A. V.; Li, J.; Ghosh, S. K. Metal-Organic Frameworks: Functional Luminescent and Photonic Materials for Sensing Applications. *Chem. Soc. Rev.* **2017**, *46*, 3242−3285.
(3) Dolgopolova, E. A.; Rice, A. M.; Martin, C. R.; Shustova, N. B. Photochemistry and Photophysics of MOFs: Steps towards MOF-Based Sensing Enhancements. *Chem. Soc. Rev.* **2018**, *47*, 4710−4728.
(4) Gutiérrez, M.; Martín, C.; Van der Auweraer, M.; Hofkens, J.; Tan, J.-C. Electroluminescent Guest@MOF Nanoparticles for Thin Film Optoelectronics and Solid-State Lighting. *Adv. Opt. Mater.* **2020**, 2000670.
(5) Yam, V. W. W.; Lo, K. K. W. Luminescent Polynuclear d10 Metal Complexes. *Chem. Soc. Rev.* **1999**, *28*, 323−334.
(6) Kaur, M.; Choi, D. H. Diketopyrrolopyrrole: Brilliant Red Pigment Dye-Based Fluorescent Probes and Their Applications. *Chem. Soc. Rev.* **2015**, *44*, 58−77.
(7) Easun, T. L.; Moreau, F.; Yan, Y.; Yang, S.; Schröder, M. Structural and Dynamic Studies of Substrate Binding in Porous Metal-Organic Frameworks. *Chem. Soc. Rev.* **2017**, *46*, 239−274.
(8) Lustig, W. P.; Li, J. Luminescent Metal−Organic Frameworks and Coordination Polymers as Alternative Phosphors for Energy Efficient Lighting Devices. *Coord. Chem. Rev.* **2018**, *373*, 116−147.
(9) Allendorf, M. D.; Foster, M. E.; Léonard, F.; Stavila, V.; Feng, P. L.; Patrick Doty, F.; Leong, K.; Ma, E. Y.; Johnston, S. R.; Alec Talin, A. Guest-Induced Emergent Properties in Metal-Organic Frameworks. *J. Phys. Chem. Lett.* **2015**, *6*, 1182−1195.
(10) Ye, J.-W.; Zhou, H.-L.; Liu, S.-Y.; Cheng, X.-N.; Lin, R.-B.; Qi, X.-L.; Zhang, J.-P.; Chen, X.-M. Encapsulating Pyrene in a Metal−Organic Zeolite for Optical Sensing of Molecular Oxygen. *Chem. Mater.* **2015**, *27*, 8255−8260.
(11) Wang, Z.; Zhu, C. Y.; Mo, J. T.; Fu, P. Y.; Zhao, Y. W.; Yin, S. Y.; Jiang, J. J.; Pan, M.; Su, C. Y. White-Light Emission from Dual-Way Photon Energy Conversion in a Dye-Encapsulated Metal-Organic Framework. *Angew. Chem., Int. Ed.* **2019**, *58*, 9752−9757.
(12) Gutiérrez, M.; Sánchez, F.; Douhal, A. Efficient Multicolor and White Light Emission from Zr-Based MOF Composites: Spectral and Dynamic Properties. *J. Mater. Chem. C* **2015**, *3*, 11300−11310.
(13) Chaudhari, A. K.; Tan, J.-C. Dual-Guest Functionalized Zeolitic Imidazolate Framework-8 for 3D Printing White Light-Emitting Composites. *Adv. Opt. Mater.* **2020**, *8*, 1901912.
(14) Mieno, H.; Kabe, R.; Notsuka, N.; Allendorf, M. D.; Adachi, C. Long-Lived Room-Temperature Phosphorescence of Coronene in Zeolitic Imidazolate Framework ZIF-8. *Adv. Opt. Mater.* **2016**, *4*, 1015−1021.
(15) Chaudhari, A. K.; Kim, H. J.; Han, I.; Tan, J. C. Optochemically Responsive 2D Nanosheets of a 3D Metal-Organic Framework Material. *Adv. Mater.* **2017**, *29*, 1701463.
(16) Xie, W.; He, W. W.; Du, D. Y.; Li, S. L.; Qin, J. S.; Su, Z. M.; Sun, C. Y.; Lan, Y. Q. A Stable Alq3@MOF Composite for White-Light Emission. *Chem. Commun.* **2016**, *52*, 3288−3291.
(17) Yang, X.; Yan, D. Direct White-Light-Emitting and Near-Infrared Phosphorescence of Zeolitic Imidazolate Framework-8. *Chem. Commun.* **2017**, *53*, 1801−1804.
(18) Mollick, S.; Mandal, T. N.; Jana, A.; Fajal, S.; Desai, A. V.; Ghosh, S. K. Ultrastable Luminescent Hybrid Bromide Perovskite@MOF Nanocomposites for the Degradation of Organic Pollutants in Water. *ACS Appl. Nano Mater.* **2019**, *2*, 1333−1340.
(19) Cha, J.-H.; Noh, K.; Yin, W.; Lee, Y.; Park, Y.; Ahn, T. K.; Mayoral, A.; Kim, J.; Jung, D.-Y.; Terasaki, O. Formation and Encapsulation of All-Inorganic Lead Halide Perovskites at Room Temperature in Metal−Organic Frameworks. *J. Phys. Chem. Lett.* **2019**, *10*, 2270−2277.
(20) He, H.; Cui, Y.; Li, B.; Wang, B.; Jin, C.; Yu, J.; Yao, L.; Yang, Y.; Chen, B.; Qian, G. Confinement of Perovskite-QDs within a Single MOF Crystal for Significantly Enhanced Multiphoton Excited Luminescence. *Adv. Mater.* **2018**, *31*, 1806897.
(21) Liu, J.; Zhuang, Y.; Wang, L.; Zhou, T.; Hirosaki, N.; Xie, R. J. Achieving Multicolor Long-Lived Luminescence in Dye-Encapsulated Metal-Organic Frameworks and Its Application to Anticounterfeiting Stamps. *ACS Appl. Mater. Interfaces* **2018**, *10*, 1802−1809.
(22) Wang, B.; Lv, X.-L.; Feng, D.; Xie, L.-H.; Zhang, J.; Li, M.; Xie, Y.; Li, J.-R.; Zhou, H.-C. Highly Stable Zr(IV)-Based Metal−Organic Frameworks for the Detection and Removal of Antibiotics and Organic Explosives in Water. *J. Am. Chem. Soc.* **2016**, *138*, 6204−6216.
(23) Gutiérrez, M.; Navarro, R.; Sánchez, F.; Douhal, A. Photodynamics of Zr-Based MOFs: Effect of Explosive Nitroaromatics. *Phys. Chem. Chem. Phys.* **2017**, *19*, 16337−16347.
(24) Wang, B.; Wang, P.; Xie, L.-H.; Lin, R.-B.; Lv, J.; Li, J.-R.; Chen, B. A Stable Zirconium Based Metal-Organic Framework for Specific Recognition of Representative Polychlorinated Dibenzo-p-dioxin Molecules. *Nat. Commun.* **2019**, *10*, 3861.
(25) Müller-Buschbaum, K.; Beuerle, F.; Feldmann, C. MOF Based Luminescence Tuning and Chemical/Physical Sensing. *Microporous Mesoporous Mater* **2015**, *216*, 171−199.
(26) Karmakar, A.; Samanta, P.; Dutta, S.; Ghosh, S. K. Fluorescent "Turn-on" Sensing Based on Metal-Organic Frameworks (MOFs). *Chem. − Asian J.* **2019**, *14*, 4506−4519.
(27) Yu, M.; Xie, Y.; Wang, X.; Li, Y.; Li, G. Highly Water-Stable Dye@Ln-MOFs for Sensitive and Selective Detection toward Antibiotics in Water. *ACS Appl. Mater. Interfaces* **2019**, *11*, 21201−21210.
(28) Dong, M. J.; Zhao, M.; Ou, S.; Zou, C.; Wu, C. D. A Luminescent Dye@MOF Platform: Emission Fingerprint Relationships of Volatile Organic Molecules. *Angew. Chem., Int. Ed.* **2014**, *53*, 1575−1579.
(29) Zheng, J.-P.; Ou, S.; Zhao, M.; Wu, C.-D. A Highly Sensitive Luminescent Dye@MOF Composite for Probing Different Volatile Organic Compounds. *ChemPlusChem* **2016**, *81*, 758−763.
(30) Gao, X.; Wang, Y.; Ji, G.; Cui, R.; Liu, Z. One-pot Synthesis of Hierarchical-Pore Metal−Organic Frameworks for Drug Delivery and Fluorescent Imaging. *CrystEngComm* **2018**, *20*, 1087−1093.
(31) Cao, L. H.; Li, H. Y.; Xu, H.; Wei, Y. L.; Zang, S. Q. Diverse Dissolution-Recrystallization Structural Transformations and Sequential Förster Resonance Energy Transfer Behavior of a Luminescent Porous Cd-MOF. *Dalton Trans* **2017**, *46*, 11656−11663.
(32) Liu, N.; Hao, J.; Chen, L.; Song, Y.; Wang, L. Ratiometric Fluorescent Detection of Cu^{2+} Based on Dual-Emission ZIF-8@Rhodamine-B Nanocomposites. *Luminescence* **2019**, *34*, 1−7.
(33) Jin, H.-G.; Zong, W.; Yuan, L.; Zhang, X.-B. Nanoscale Zeolitic Imidazole Framework-90: Selective, Sensitive and Dual-Excitation Ratiometric Fluorescent Detection of Hazardous Cr(VI) Anions in Aqueous Media. *New J. Chem.* **2018**, *42*, 12549−12556.
(34) Shen, X.; Yan, B. Anionic Metal−Organic Framework Hybrids: Functionalization with Lanthanide Ions or Cationic Dyes and Fluorescence Sensing of Small Molecules. *RSC Adv.* **2016**, *6*, 28165−28170.
(35) Yin, H.; Khosravi, A.; O'Connor, L.; Tagaban, A. Q.; Wilson, L.; Houck, B.; Liu, Q.; Lind, M. L. Effect of ZIF-71 Particle Size on Free-Standing ZIF-71/PDMS Composite Membrane Performances for Ethanol and 1-Butanol Removal from Water through Pervaporation. *Ind. Eng. Chem. Res.* **2017**, *56*, 9167−9176.
(36) Song, Y.; Hu, D.; Liu, F.; Chen, S.; Wang, L. Fabrication of Fluorescent SiO_2@Zeolitic Imidazolate Framework-8 Nanosensor for Cu^{2+} Detection. *Analyst* **2015**, *140*, 623−629.
(37) Allendorf, M. D.; Bauer, C. A.; Bhakta, R. K.; Houk, R. J. T. Luminescent Metal-Organic Frameworks. *Chem. Soc. Rev.* **2009**, *38*, 1330−1352.
(38) Lakowicz, J. R., *Principles of Fluorescence Spectroscopy*. Third ed.; Springer: Singapore, 2006.
(39) Chin, M.; Cisneros, C.; Araiza, S. M.; Vargas, K. M.; Ishihara, K. M.; Tian, F. Rhodamine B Degradation by Nanosized Zeolitic Imidazolate Framework-8 (ZIF-8). *RSC Adv.* **2018**, *8*, 26987−26997.

https://dx.doi.org/10.1021/acsami.0c10257
ACS Appl. Mater. Interfaces 2020, 12, 37477−37488

(40) Ilich, P.; Mishra, P. K.; Macura, S.; Burghardt, T. P. Direct Observation of Rhodamine Dimer Structures in Water. *Spectrochim. Acta A* **1996**, *52*, 1323−1330.
(41) Setiawan, D.; Kazaryan, A.; Martoprawiro, M. A.; Filatov, M. A First Principles Study of Fluorescence Quenching in Rhodamine B Dimers: How can Quenching Occur in Dimeric Species? *Phys. Chem. Chem. Phys.* **2010**, *12*, 11238−11244.
(42) Kasha, M. Characterization of Electronic Transitions in Complex Molecules. *Discuss. Faraday Soc.* **1950**, *9*, 14−19.
(43) Chaudhari, A. K.; Tan, J. C. Mechanochromic MOF Nanoplates: Spatial Molecular Isolation of Light-Emitting Guests in a Sodalite Framework Structure. *Nanoscale* **2018**, *10*, 3953−3960.
(44) Fujii, K.; Garay, A. L.; Hill, J.; Sbircea, E.; Pan, Z.; Xu, M.; Apperley, D. C.; James, S. L.; Harris, K. D. M. Direct Structure Elucidation by Powder X-ray Diffraction of a Metal-Organic Framework Material Prepared by Solvent-Free Grinding. *Chem. Commun.* **2010**, *46*, 7572−7574.
(45) Hutchings, B. P.; Crawford, D. E.; Gao, L.; Hu, P.; James, S. L. Feedback Kinetics in Mechanochemistry: The Importance of Cohesive States. *Angew. Chem., Int. Ed.* **2017**, *56*, 15252−15256.
(46) Cui, Y.; Yue, Y.; Qian, G.; Chen, B. Luminescent Functional Metal-Organic Frameworks. *Chem. Rev.* **2011**, *112*, 1126−1162.
(47) (a) Su, Z.; Miao, Y. R.; Mao, S. M.; Zhang, G. H.; Dillon, S.; Miller, J. T.; Suslick, K. S. Compression-Induced Deformation of Individual Metal-Organic Framework Microcrystals. *J. Am. Chem. Soc.* **2015**, *137*, 1750−1753. (b) Tan, J. C.; Civalleri, B.; Lin, C. C.; Valenzano, L.; Galvelis, R.; Chen, P. F.; Bennett, T. D.; Mellot-Draznieks, C.; Zicovich-Wilson, C. M.; Cheetham, A. K. Exceptionally Low Shear Modulus in a Prototypical Imidazole-Based Metal-Organic Framework. *Phys. Rev. Lett.* **2012**, *108*, 095502.
(48) Hinckley, D. A.; Seybold, P. G.; Borris, D. P. Solvatochromism and Thermochromism of Rhodamine Solutions. *Spectrochim. Acta* **1986**, *42*, 747−754.
(49) Rosenthal, I.; Peretz, P.; Muszkat, K. A. Thermochromic and Hyperchromic Effects in Rhodamine B Solutions. *J. Phys. Chem.* **1979**, *83*, 350−353.
(50) Xi, G.; Sheng, L.; Zhang, I.; Du, J.; Zhang, T.; Chen, Q.; Li, G.; Zhang, Y.; Song, Y.; Li, J.; Zhang, Y.-M.; Zhang, S. X.-A. Endowing Hydrochromism to Fluorans via Bioinspired Alteration of Molecular Structures and Microenvironments and Expanding Their Potential for Rewritable Paper. *ACS Appl. Mater. Interfaces* **2017**, *9*, 38032−38041.

https://dx.doi.org/10.1021/acsami.0c10257
ACS Appl. Mater. Interfaces 2020, 12, 37477−37488

Paper II: Electrospun Rhodamine@MOF/Polymer Luminescent Fibers with a Quantum Yield of Over 90%

iScience

CellPress
OPEN ACCESS

Article

Electrospun rhodamine@MOF/polymer luminescent fibers with a quantum yield of over 90%

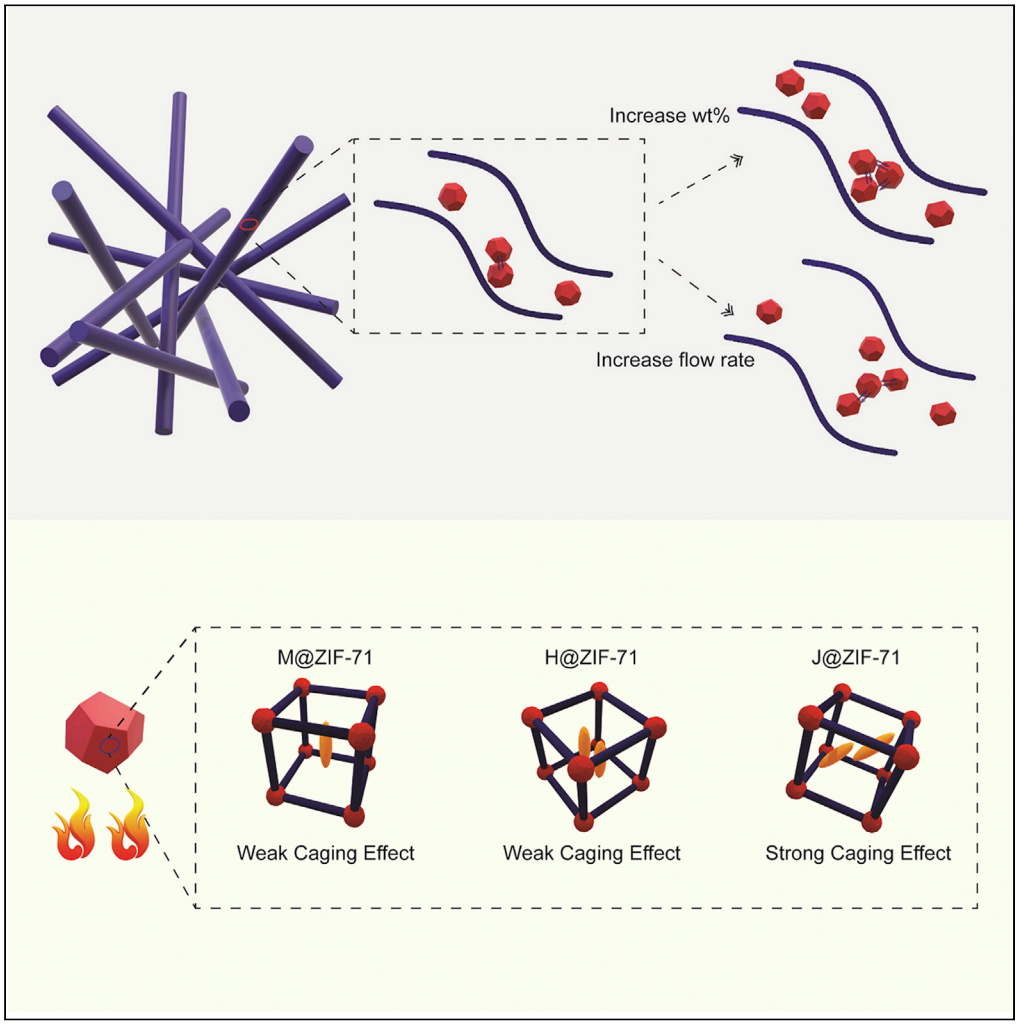

Yang Zhang, Jin-Chong Tan

jin-chong.tan@eng.ox.ac.uk

Highlights

Thermofluorochromic fibers incorporating Guest@MOF engineered by electrospinning

J-aggregates of rhodamine B (RhB) interact through adjacent ZIF-71 nanocrystals

RhB@ZIF-71/PVDF fiber has a quantum yield exceeding 90%

ZIF-71 host enhances the thermal stability of nanoconfined RhB guest

Zhang & Tan, iScience 24, 103035
September 24, 2021
https://doi.org/10.1016/j.isci.2021.103035

iScience

CellPress
OPEN ACCESS

Article

Electrospun rhodamine@MOF/polymer luminescent fibers with a quantum yield of over 90%

Yang Zhang[1] and Jin-Chong Tan[1,2,*]

SUMMARY

Tailored luminescent guest@metal-organic framework (Guest@MOF) materials with outstanding photophysical properties are enabling materials for emergent technologies in smart sensors and optoelectronics. However, the practical utility of Guest@MOF currently is impaired by its poor stability and difficult-to-handle powder form. Here, we combine a luminescent-sensing Guest@MOF system with a non-luminescent polymer matrix and, for the first time, demonstrated the easy-to-apply electrospinning of luminescent fibers comprising nanocrystals of RhB@ZIF-71 (rhodamine B@zeolitic imidazolate framework-71) homogeneously dispersed in a polyvinylidene difluoride (PVDF) matrix. The luminescence of RhB@ZIF-71/PVDF fiber is tunable and exhibits a quantum yield exceeding 90%. Compared with RhB fluorophore in PVDF fiber, the ZIF-71 (host) protects the nanoconfined RhB guest molecules (especially the J-aggregates of RhB), giving the composite fiber its unique thermofluorochromic response and enhanced thermal stability to 200°C. Our results reveal the exciting opportunities for implementing electrospun luminescent fibers functionalized with bespoke Guest@MOF nanocrystals for multifunctional device applications.

INTRODUCTION

Light-emitting materials (LEMs) convert absorbed energy into light; they are therefore central to technological applications and widely integrated into LEDs for lighting and display, fluorescent sensors, bio-imaging, photoswitches, and optoelectronics (Li et al., 2020; Luo et al., 2020; Lustig et al., 2017; Stassen et al., 2017). In recent years, with the advent of device miniaturization, portability, and energy saving requirements of modern optoelectronics, improving the performance of solid-state LEMs has become increasingly demanding (Kamtekar et al., 2010; Kanagaraj et al., 2019). That has stimulated a lot of research on exploring new solid-state LEMs. Among the many new types of solid-state LEMs studied, metal-organic frameworks (MOFs) have been demonstrated as one of the most promising candidate materials for engineering fluorescent optics and sensors because of their porous, ordered, and highly adjustable structure for tunable photophysics and photochemistry (Mollick et al., 2019; Gutiérrez et al., 2021; Chaudhari and Tan, 2020; Aguilera-Sigalat and Bradshaw, 2016; Takashima et al., 2011). In principle, the luminescent properties of MOFs can be designed and controlled by tailoring the molecular building blocks to meet the varied application requirements (Cui et al., 2012; Dolgopolova et al., 2018; Easun et al., 2017; Heine and Muller-Buschbaum, 2013; Yao et al., 2020).

The physical and chemical functions of MOFs can be enhanced further by leveraging the concept of "Guest@MOF" system (Allendorf et al., 2015), yielding luminescent composite materials attractive for solid-state lighting and optical sensing applications (Zhang et al., 2020; Gutiérrez et al., 2020; Chaudhari et al., 2017; Lin et al., 2019). This "guest-host" system takes advantage of the porous nature of MOF (serving as a "host") to confine luminescent molecules (as a "guest") into the nanoscale pores or by trapping them within the extended MOF structures. MOF can apply a caging effect to the nanoconfined guests; this mechanism helps to limit the non-radiative decay of fluorophores and thus improving the guests' luminescent properties (Wang et al., 2019; Tang et al., 2014; Mieno et al., 2016; Hao and Yan, 2015; Asadi et al., 2019). Furthermore, because many MOF structures are themselves also luminescent, the MOF host can form a dual-emission system with the guest or transfer the absorbed energy to the guest, further improving the overall luminescent performance (Dong et al., 2014; Fu et al., 2018; Qin and Yan, 2018; Yoo et al., 2019; Zhao et al., 2018). For example, our research group developed a RhB@ZIF-71 system (i.e., rhodamine B fluorophores confined in zeolitic imidazolate framework-71 host), which not only overcomes the drawback that RhB cannot emit light in the solid-state due to quenching but also endows the material with new

[1]Multifunctional Materials & Composites (MMC) Laboratory, Department of Engineering Science, University of Oxford, Parks Road, Oxford OX1 3PJ, UK

[2]Lead contact

*Correspondence: jin-chong.tan@eng.ox.ac.uk

https://doi.org/10.1016/j.isci.2021.103035

functions, namely mechanochromism, thermochromism, and solvatochromism (Zhang et al., 2020). However, the Guest@MOF materials may suffer from certain shortcomings, especially of poor long-term stability under real-world engineering application conditions. Besides, this material's loose powdery morphology may not be suitable for certain applications, such as optical fibers and precision devices.

To address the outstanding challenges in the field, herein we demonstrate a Guest@MOF material that can be facilely combined with polymers to form a composite, which enables the Guest@MOF material to retain its luminescent properties, enhance thermal stability, and improve its processability so that it can afford practical engineering applications. In this study, we combined RhB@ZIF-71 nanocrystals, as an example, with a PVDF (polyvinylidene difluoride) polymer matrix, which has excellent durability and is non-luminescent, to make easy-to-apply nanofibers by electrospinning technology. Compared with RhB@ZIF-71 powder, we found the composite fibers show a high quantum yield (QY) combined with excellent thermal stability, broadening the application of this Guest@MOF material.

RESULTS AND DISCUSSION

Nanocrystals of RhB@ZIF-71 from high concentration reaction

Recent studies have shown that the nominal size of the RhB@ZIF-71 crystals synthesized by the traditional method is about 800 nm to 1 μm (Yin et al., 2017; Zhang et al., 2020), which is way too large for incorporation into nanofibers (bigger crystals may not to be completely covered by polymer matrix). To reduce the size of the RhB@ZIF-71 crystal, herein we applied the high concentration reaction (HCR) method (see detailed reaction steps in the experimental section). HCR uses a small quantity of solvents to increase the reactants concentration, when coupled with triethylamine (NEt_3) this accelerates the deprotonation of the linkers to enhance nucleation rate and reducing the crystal size (Chaudhari et al., 2017). In contrast to traditional synthesis, which takes many hours to stir the solution during a slow crystallization step, the HCR method yields nanocrystals spontaneously. The Guest@MOF product is formed instantaneously during solution mixing, which considerably shortens the synthesis time and this could benefit future industrial production.

Figure 1 shows the morphology, crystal structure, and the solid-state luminescent properties of the HCR-synthesized RhB@ZIF-71 measured by atomic force microscopy (AFM), powder X-ray diffraction (PXRD), and spectrofluorometry, respectively. From Figures 1A and 1B, it can be seen that the size of the obtained RhB@ZIF-71 nanocrystal is about 50–150 nm. Importantly, the RhB@ZIF-71 retains the crystalline structure of ZIF-71 (Figure 1C) and exhibits the characteristic luminescent properties of the RhB fluorophore (Figure 1D). These unique features of RhB@ZIF-71 provide the opportunity to fabricate nanofibers via electrospinning, as described below.

Morphology and microstructure of electrospun fibers

After dispersing the nanocrystals of RhB@ZIF-71 within the PVDF solution (polymer matrix), we used electrospinning technology to process the composite mixture into RhB@ZIF-71/PVDF nanofibers. SEM images in Figure 2 show that the surface of the obtained fibers exhibits a highly uniform dispersion of nanocrystals coated by the PVDF matrix, and there is no sizable RhB@ZIF-71 aggregate present on the fiber surface. For comparison, the "normal" (without HCR) RhB@ZIF-71/PVDF fibers were made using the same electrospinning technique; the SEM images (Figure S1) revealed that there are many micron-sized crystals and large aggregates prevalent on the fibers.

To confirm that the prepared fibers still retain the functional RhB@ZIF-71 instead of being decomposed or lost during the electrospinning process, we tested the fibers under a UV lamp. Compared to pure PVDF, which is not luminescent, the RhB@ZIF-71 fibers show a distinctive fluorescence (Figures 3A and 3B). This observation proves that the RhB@ZIF-71 is intact in the fiber. Subsequently, we have systematically performed the X-ray diffraction (XRD), ultraviolet-visible (UV-Vis) diffuse reflectance spectroscopy, and attenuated total reflection Fourier-transform infrared spectroscopy (ATR-FTIR) characterization on these fibers (Figure 3). From the XRD patterns in Figure 3C, we can identify the peaks of RhB@ZIF-71/PVDF fibers at 2θ of about 4° and 7.5°; these correspond to the characteristic peaks of the RhB@ZIF-71 nanocrystals. In addition, the appearance of the peaks at ~20° in the PVDF fiber and RhB@ZIF-71/PVDF fiber indicates that the introduction of RhB@ZIF-71 into the polymer matrix has no effect on the transformation of PVDF from α to β phase during electrospinning (Flyagina et al., 2017); this finding suggests that there is no strong interaction between RhB@ZIF-71 and PVDF. From Figures 3D and 3E, we can also get the same inference by observing the similar RhB characteristic absorbance peak between 450 and 600 nm and the FTIR peak of ZIF-71 at 1052 cm^{-1}. We infer that the

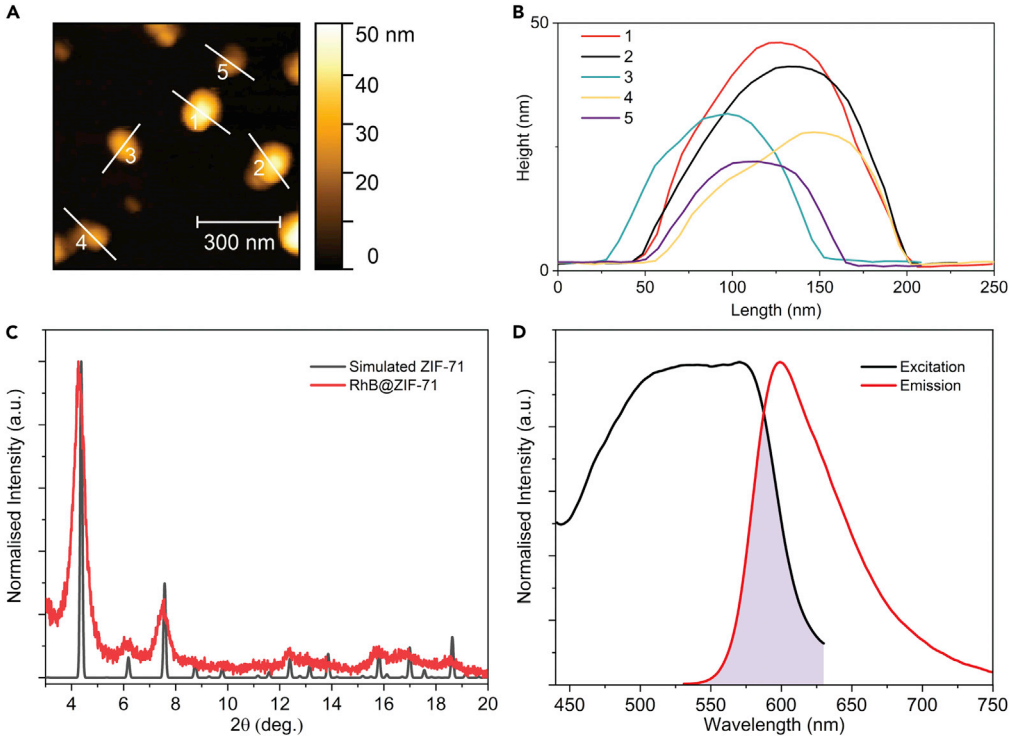

Figure 1. Characterization of RhB@ZIF-71 nanocrystals

(A and B) AFM height topography showing the nominal size of the RhB@ZIF-71 nanocrystals synthesized by the HCR method.

(C) PXRD patterns of RhB@ZIF-71 powder where peak broadening is due to nanocrystals, compared with the simulated pattern of ZIF-71.

(D) Solid-state excitation and emission spectra of the RhB@ZIF-71 powder.

high hydrophobicity originated from the chemical structure of ZIF-71 produces many surface-bound negative charges (Nauruzbayeva et al., 2020), and it is due to this repelling electrostatic effect that RhB@ZIF-71 nanocrystals achieve a relatively uniform dispersion in the PVDF fiber.

Photoluminescent properties of RhB@ZIF-71/PVDF fibers

It is expected that the different processing parameters during electrospinning will modify the fiber properties, which in turn might affect the luminescence behavior of RhB@ZIF-71/PVDF fibers. To investigate this possible effect, we compared the excitation and emission spectra of the electrospun fiber mats containing different mass fractions (wt.%) of RhB@ZIF-71 nanocrystals (Figures 4A and 4B) and those obtained by varying the polymer flow rates (μL/min) through the nozzle (Figures 4C and 4D).

From Figures 4B and 4D, it can be seen that with the increase in the mass fraction and flow rate, the luminescence of RhB@ZIF-71/PVDF fibers yields a redshift. Observing Figures 4A and 4C, we note that the excitation peak became wider and the shoulder to the peak ratio increases, suggesting that with the increase in the mass fraction and flow rate, the number of RhB@ZIF-71 nanocrystals per unit fiber length also rises (Note: for samples with increased flow rate, the reason is due to the larger fiber diameter, see Figure 4D inset and Figures S2–S4). On this basis, the reason for the observed redshift may be associated with more RhB@ZIF-71 crystals causing more interactions between the RhB J-aggregates over the contacting crystal interfaces. This mechanism is similar to the interaction described in the previous literature (Chaudhari and Tan, 2018;Zhang et al., 2020).

Lifetime data determined from time-correlated single-photon counting (TCSPC) measurements (Figure 5, Tables S1 and S2) can help to validate this hypothesis. The time constant τ_2 in Figure 5, Tables S1, and S2, which represents the lifetime of RhB J-aggregates, was found to decrease with the increase of mass fraction and flow rate. This trend indicates a stronger interaction between the J-aggregates. On the other hand, the

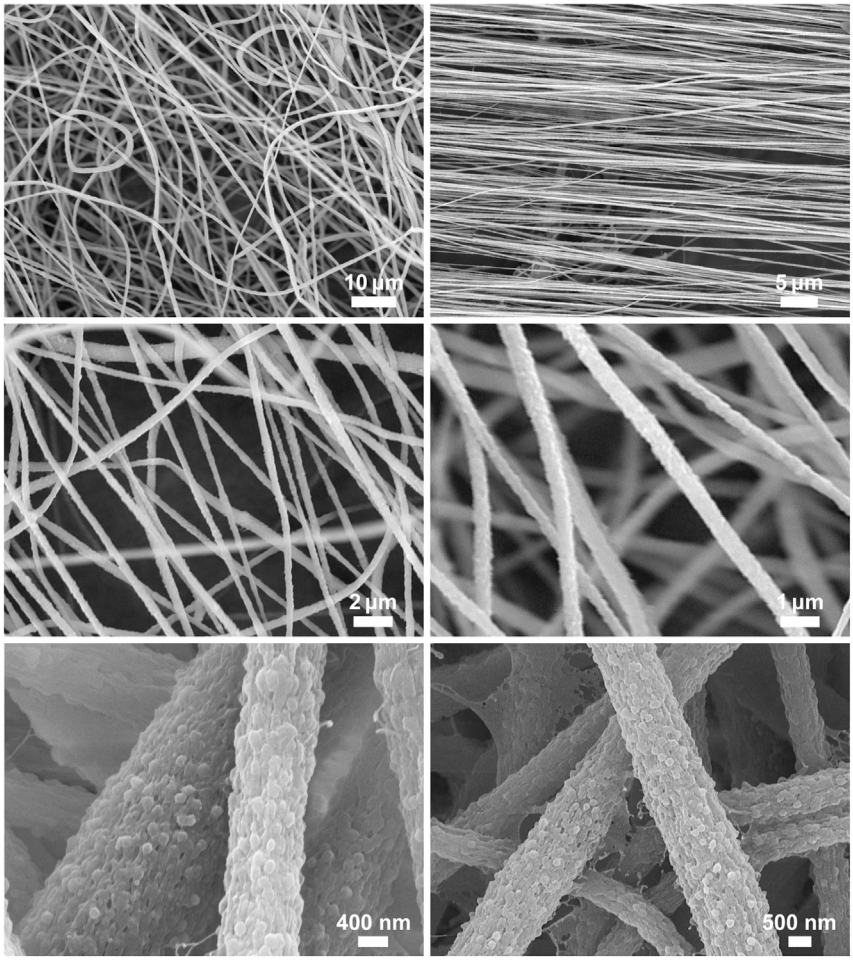

Figure 2. Electron micrographs of electrospun PVDF fibers incorporating RhB@ZIF-71 HCR nanocrystals
The orientation of the individual fibers (random vs aligned) and the overall architecture of fiber mat can be controlled by employing collectors of different geometries. The high-resolution images at the bottom images reveal the uniform dispersion of the HCR nanocrystals coated by the PVDF matrix.

pre-exponential factor and fractional contribution of J-aggregates (a_2 and c_2, respectively) both show higher values as the flow rate increases (Table S2), which we attributed to the stronger caging effect experienced by the J-aggregates. With a faster flow rate, a greater negative impact on RhB luminescence is also anticipated due to the incorporation of residual polar aprotic solvents (i.e. dimethylacetamide (DMA) will turn RhB into the less emissive lactone form) (Zhang et al., 2020; Hinckley et al., 1986). The relatively large J-aggregates will receive a stronger caging effect (Zhang et al., 2020), becoming more difficult to be affected by the solvent molecules (i.e. reducing pore space to accommodate additional solvent molecules) and thus resulting in the increase in the values of a_2 and c_2. The lifetime data therefore enable us to explain why a higher wt.% loading of RhB and/or a higher flow rate will give an emission redshift.

Further to the tunable luminescence elucidated above, another striking feature of RhB@ZIF-71/PVDF fiber is that it exhibits a high QY (Figures 5C and 5D, Tables S3 and S4). Because the caging effect reduces the non-radiative decay of RhB (Zhang et al., 2020; Mieno et al., 2016; Cui et al., 2012) and the introduction of PVDF significantly decreases the self-absorption of well-dispersed RhB@ZIF-71 nanocrystals (ascribed to the overlapping excitation-emission phenomenon, see Figure 1D), we found that the fibers obtained under the conditions of 1 wt.% and 8 µL/min achieve a QY of ~92% (versus QY ~25% in the corresponding bulk powder sample). This value of QY is the highest yet among the MOF-polymer systems reported to date (Zhang et al., 2007; Bai et al., 2018) and when compared against the RhB-based fluorescent materials whose QYs are commonly lying in the relatively lower bound of 30–60% (Table S5) (Ahmed and Saif, 2013;

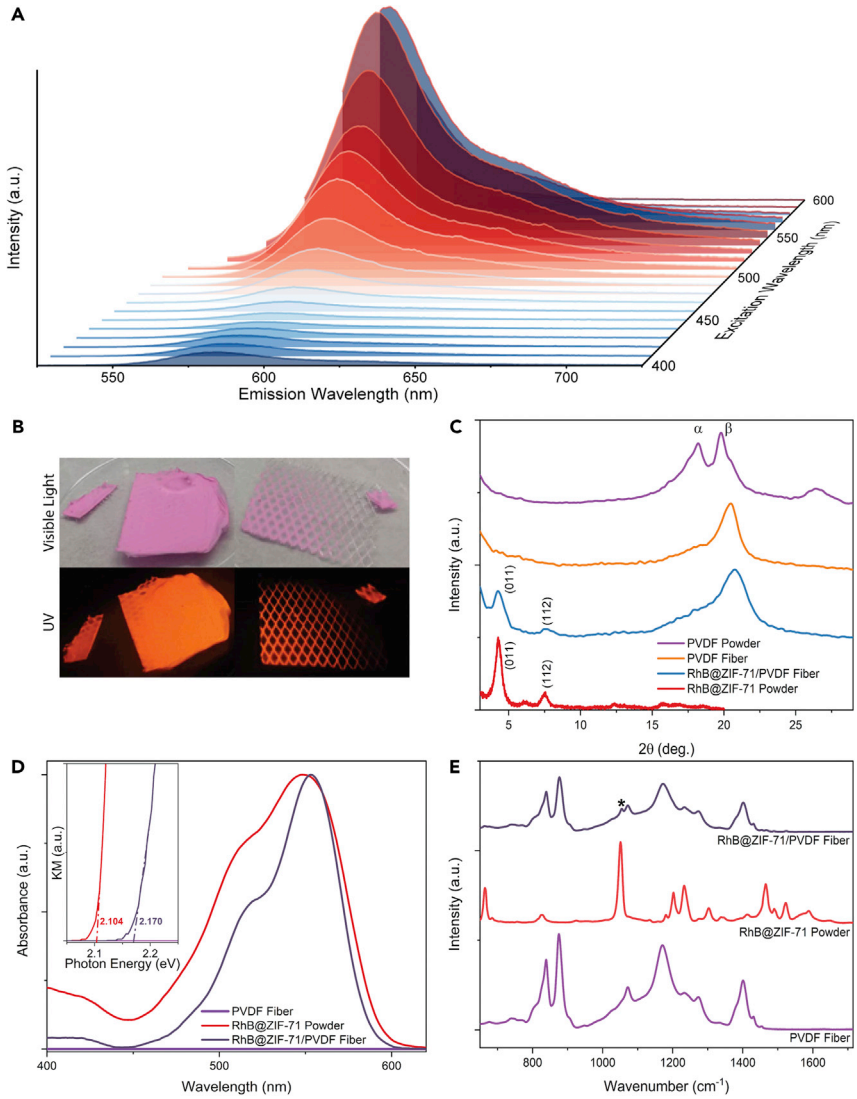

Figure 3. Characterization of RhB@ZIF-71/PVDF fibers

(A and B) (A) Emission map for a range of excitation wavelengths ranging from 400 to 600 nm (B) RhB@ZIF-71/PVDF fiber mats (random and textured) under the visible light and their luminescence under the UV lamp (365 nm excitation). (C–E) (C) XRD, (D) UV-Vis diffuse reflectance spectra (the insert figure is the Kubelka-Munk function for estimating the optical band gaps based on the photon energy intercepts), and (E) ATR-FTIR spectra of RhB@ZIF-71/PVDF fibers, RhB@ZIF-71 HCR powder, and PVDF fibers. The * symbol in (E) denotes the position of the 1052 cm^{-1} peak of ZIF-71.

Khader, 2008; Sagoo and Jockusch, 2011; Stobiecka and Hepel, 2011). Our findings reveal that this high QY fiber can be a promising candidate for optoelectronics and sensing.

Comparison of thermofluorochromic properties between RhB@ZIF-71/PVDF fibers and RhB/PVDF fibers

In order to further study the thermofluorochromic properties of RhB@ZIF-71/PVDF fibers, we focused on the highest QY fiber mat, i.e. RhB@ZIF-71/PVDF prepared under the conditions of 1 wt.% and 8 μL/min, and systematically studied its thermochromism compared with the RhB/PVDF fibers.

From the excitation and emission spectra (Figure S5) of these two kinds of fibers, it is clear that the luminescent properties of the two were similar under ambient conditions. However, under a high-temperature environment, the luminescence of RhB@ZIF-71/PVDF fiber was significantly more stable than the RhB/PVDF

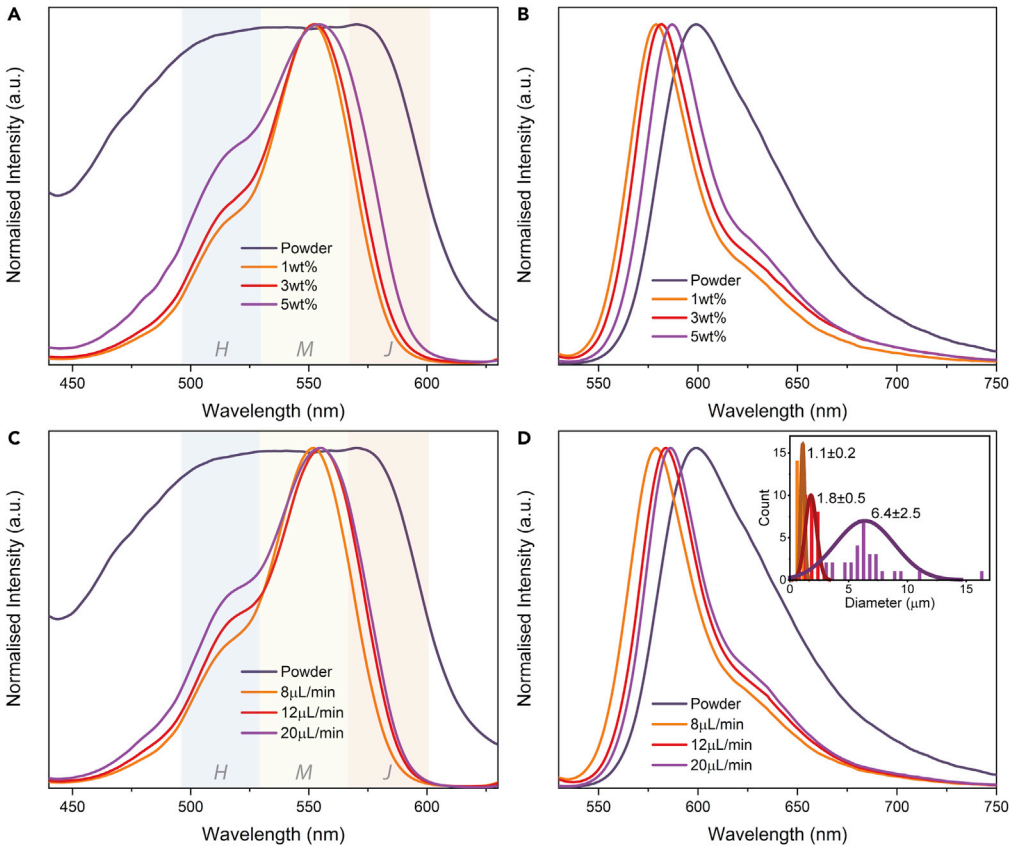

Figure 4. Fluorescent properties of RhB@ZIF-71/PVDF fibers with different processing parameters

Excitation and emission spectra of RhB@ZIF-71/PVDF fibers with different mass fraction of guest loading wt.% (A and B) and by using different PVDF flow rate for electrospinning (C and D), respectively. The spectra of the pristine RhB@ZIF-71 powder are plotted together for contrast. The inset of (D) shows the normal distributions of the fiber diameters associated with the differential flow rates in electrospinning.

fiber. From the excitation and emission spectra measured at different temperatures (Figures 6 and S6), we established that when the temperature was close to 200°C, the RhB@ZIF-71/PVDF fiber still maintains its good RhB luminescence characteristics, but the emission of RhB/PVDF fibers was significantly degraded. This thermally induced material damage can also be seen with the naked eye as depicted in the insets of Figure 6E, showing the luminescent properties of RhB/PVDF are considerably deteriorated after heating to 200°C due to the dramatic increase in non-radiative decay as a function of temperature (Hinckley et al., 1986), and subsequently the molecular decomposition of RhB when approaching 200°C (Zhang et al., 2020).

Moreover, in a gradually heating environment, the RhB@ZIF-71/PVDF fiber showed a systematic redshift (Figures 6B and 6C), and its corresponding excitation (550–600 nm, Figure 6A) exhibited a relative increase in intensity. In contrast, the optical response of RhB/PVDF fiber has no correlation to the temperature at all, see Figure 6D. These phenomena are in line with the conclusions in our previous study: the J-aggregates are subjected to a stronger caging effect in ZIF-71, leading to a relative increase in intensity at high temperature (Zhang et al., 2020), which will result in a luminescent redshift. After cooling, we found that the emission of RhB@ZIF-71/PVDF fiber retained a certain degree of redshift (Figures 6B and 6C), the peak position of its excitation did not change, and the relative intensity of the right shoulder of the excitation (560–580 nm) increased (Figure 6A). These observed characteristics support the notion that the J-aggregates within the RhB@ZIF-71/PVDF fibers are better protected under an elevated temperature. In addition, we observed that the luminescence of RhB@ZIF-71/PVDF fiber was not affected by the melting point of PVDF (Figure S7), notably the luminescence property of RhB is retained after undergoing multicyclic heating (Figure S8). Our results show that the caging effect conferred by the ZIF-71 host framework can greatly enhance the thermal stability of the nanoconfined RhB guest molecules.

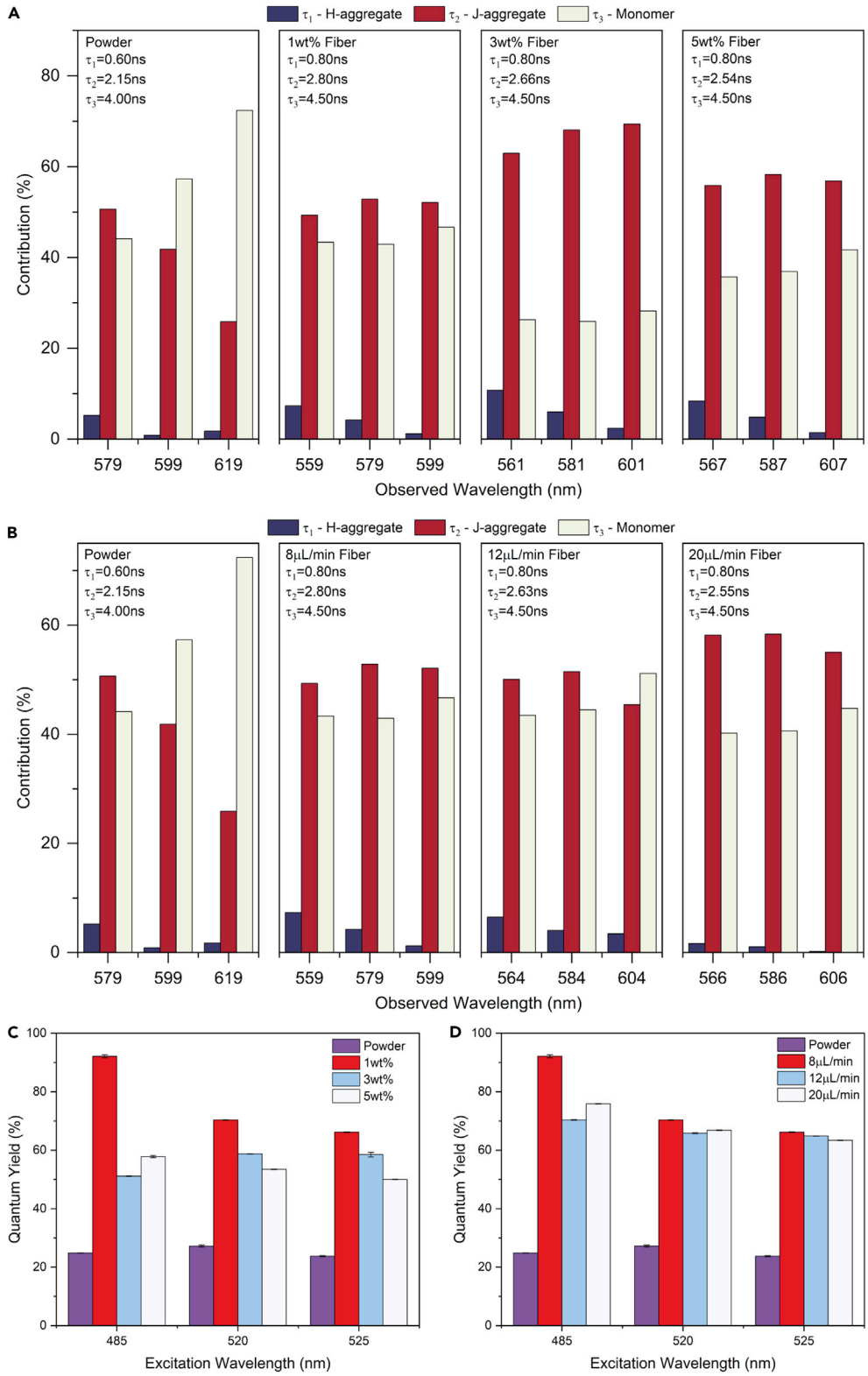

Figure 5. Fluorescent lifetime characteristics and quantum yield of RhB@ZIF-71/PVDF fibers

Contributions = τ_i × normalize pre-exponential factors a_i, $R_t = \Sigma a_i e^{(-t/\tau_i)}$, R_t is the quantity/counts at time t. (A and C) Effects of the different weight percentages and (B and D) the different flow rates.

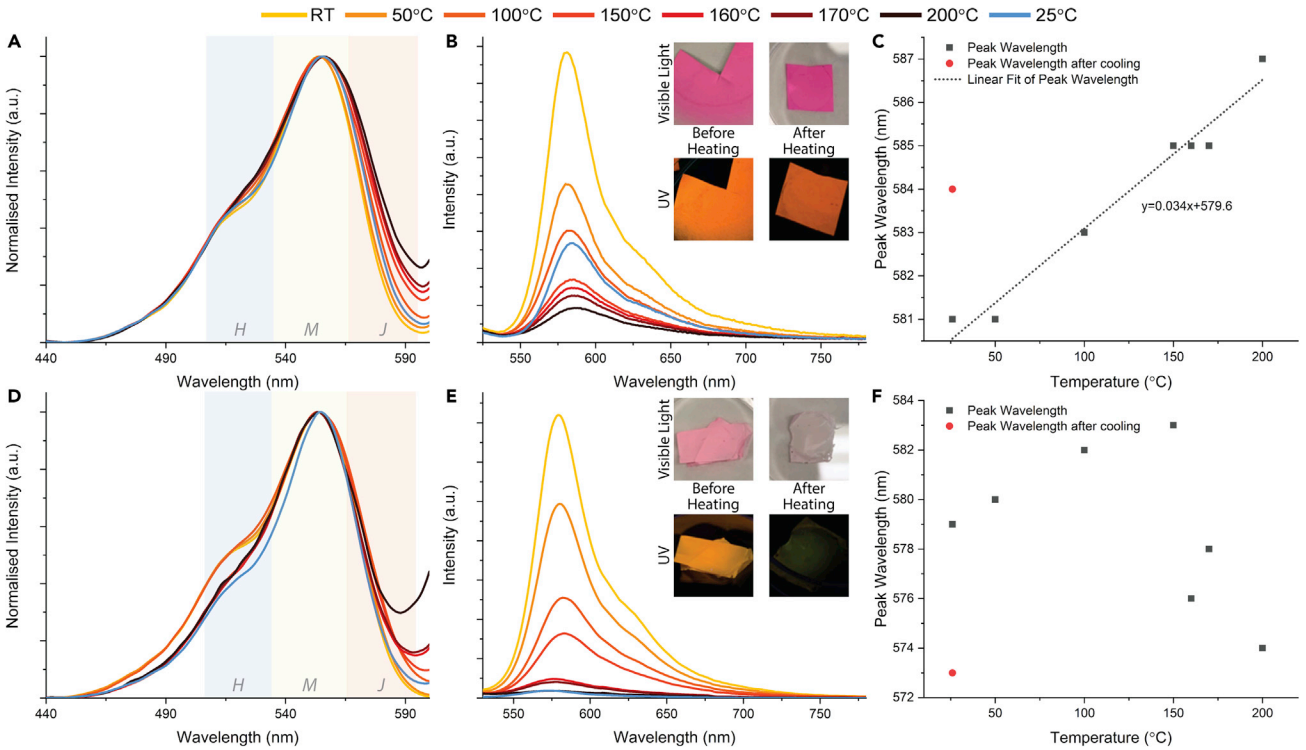

Figure 6. Thermochromism of RhB@ZIF-71/PVDF and RhB/PVDF fibers

Excitation, emission, and peak wavelength changing during heat treatment of (A–C) 1 wt.% RhB@ZIF-71/PVDF fibers and (D–F) RhB/PVDF fibers at different temperatures.

Conclusions

In summary, we report the first example of a thermofluorochromic electrospun fiber comprising a novel Guest@MOF/polymer composite system, termed RhB@ZIF-71/PVDF. We show that it is critical to employ the nanosized crystals of RhB@ZIF-71 (derived from the HCR method) to accomplish a uniform coverage of luminescent crystals dispersed within the polymer matrix. Using fluorescent lifetime spectroscopy, we characterized the interaction of the J-aggregates of RhB between adjacent RhB@ZIF-71 nanocrystals; this mechanism gave the electrospun fiber its luminescence tunability which was subsequently exploited for fluorescent thermometry. Significantly, because the PVDF matrix is helping to greatly reduce the self-absorption effect of RhB@ZIF-71, the composite fiber obtained has a remarkably high QY of ~92%. This value markedly surpasses the typical QY values reported for RhB-based solutions (<66%) and composite solids (<40%). Furthermore, the electrospun composite fibers have achieved enhanced thermal stability under thermal cycling to 200°C and show a notably improved thermochromic performance due to the confinement by the ZIF-71 host. The versatility of electrospinning to tailor composite fiber diameter and architecture combined with the enhanced luminescent sensing properties of the integrated Guest@MOF system bodes well for future engineering applications.

Limitations of the study

RhB@ZIF-71 exhibits multifluorochromic sensing properties which have not been fully investigated in this work apart from its thermofluorochromic effects reported herein. According to the ideas of this article, the fluorescent electrospun fibers with other sensing properties could be further studied.

STAR★METHODS

Detailed methods are provided in the online version of this paper and include the following:

- KEY RESOURCES TABLE
- RESOURCE AVAILABILITY
  - Lead contact

SUPPLEMENTAL INFORMATION

Supplemental information can be found online at https://doi.org/10.1016/j.isci.2021.103035.

ACKNOWLEDGMENTS

This work was supported by the EPSRC Impact Acceleration Account Award (EP/R511742/1) and the ERC Consolidator Grant (PROMOFS grant agreement 771575). We thank the Research Complex at Harwell (RCaH) for the provision of a range of material characterization facilities. We acknowledge Dr. Cyril Besnard and Professor. Alexander M. Korsunsky for the acquisition of the FESEM images.

AUTHOR CONTRIBUTIONS

Conceptualization, Y.Z. and J.-C.T.; methodology, Y.Z. and J.-C.T.; investigation, Y.Z.; writing – original draft, Y.Z.; writing – review & editing, Y.Z. and J.-C.T.; supervision, J.-C.T.

DECLARATION OF INTERESTS

The authors declare no competing interests.

Received: June 23, 2021
Revised: August 3, 2021
Accepted: August 20, 2021
Published: September 24, 2021

REFERENCES

Aguilera-Sigalat, J., and Bradshaw, D. (2016). Synthesis and applications of metal-organic framework–quantum dot (QD@MOF) composites. Coord. Chem. Rev. *307*, 267–291.

Ahmed, R.M., and Saif, M. (2013). Optical properties of rhodamine B dye doped in transparent polymers for sensor application. Chin. J. Phys. *51*, 511–521.

Allendorf, M.D., Foster, M.E., Leonard, F., Stavila, V., Feng, P.L., Doty, F.P., Leong, K., Ma, E.Y., Johnston, S.R., and Talin, A.A. (2015). Guest-induced emergent properties in metal-organic frameworks. J. Phys. Chem. Lett. *6*, 1182–1195.

Asadi, F., Azizi, S.N., and Chaichi, M.J. (2019). Green synthesis of fluorescent PEG-ZnS QDs encapsulated into Co-MOFs as an effective sensor for ultrasensitive detection of copper ions in tap water. Mater. Sci. Eng. C Mater. Biol. Appl. *105*, 110058.

Bai, J.Y., Liu, Y., Hou, Y.J., and Wang, S.H. (2018). Electrospinning preparation and luminescence properties of $Eu_2(PBT)_3(NO_3)_3$/PMMA composite nanofibers. Mater. Chem. Phys. *217*, 486–492.

Chaudhari, A.K., Kim, H.J., Han, I., and Tan, J.C. (2017). Optochemically responsive 2D nanosheets of a 3D metal-organic framework material. Adv. Mater. *29*, 1701463.

Chaudhari, A.K., and Tan, J.C. (2018). Mechanochromic MOF nanoplates: spatial molecular isolation of light-emitting guests in a sodalite framework structure. Nanoscale *10*, 3953–3960.

Chaudhari, A.K., and Tan, J.C. (2020). Dual-guest functionalized zeolitic imidazolate framework-8 for 3D printing white light-emitting composites. Adv. Opt. Mater. *8*, 1901912.

Cui, Y., Yue, Y., Qian, G., and Chen, B. (2012). Luminescent functional metal-organic frameworks. Chem. Rev. *112*, 1126–1162.

Dolgopolova, E.A., Rice, A.M., Martin, C.R., and Shustova, N.B. (2018). Photochemistry and photophysics of MOFs: steps towards MOF-based sensing enhancements. Chem. Soc. Rev. *47*, 4710–4728.

Dong, M.J., Zhao, M., Ou, S., Zou, C., and Wu, C.D. (2014). A luminescent dye@MOF platform: emission fingerprint relationships of volatile organic molecules. Angew. Chem. Int. Ed. *53*, 1575–1579.

Easun, T.L., Moreau, F., Yan, Y., Yang, S., and Schroder, M. (2017). Structural and dynamic studies of substrate binding in porous metal-organic frameworks. Chem. Soc. Rev. *46*, 239–274.

Flyagina, I.S., Mahdi, E.M., Titov, K., and Tan, J.-C. (2017). Thermo-mechanical properties of mixed-matrix membranes encompassing zeolitic imidazolate framework-90 and polyvinylidine difluoride: ZIF-90/PVDF nanocomposites. APL Mater. *5*, 086104.

Fu, H.-R., Yan, L.-B., Wu, N.-T., Ma, L.-F., and Zang, S.-Q. (2018). Dual-emission MOF⊃Dye sensor for ratiometric fluorescence recognition of RDX and detection of a broad class of nitro-compounds. J. Mater. Chem. A. *6*, 9183–9191.

Gutiérrez, M., Martín, C., Van Der Auweraer, M., Hofkens, J., and Tan, J.C. (2020). Electroluminescent guest@MOF nanoparticles for thin film optoelectronics and solid-state lighting. Adv. Opt. Mater. *8*, 2000670.

Gutiérrez, M., Moslein, A.F., and Tan, J.C. (2021). Facile and fast transformation of nonluminescent to highly luminescent metal-organic frameworks: acetone sensing for diabetes diagnosis and lead capture from polluted water. ACS Appl. Mater. Inter. *13*, 7801–7811.

Hao, J.N., and Yan, B. (2015). A water-stable lanthanide-functionalized MOF as a highly selective and sensitive fluorescent probe for Cd^{2+}. ChemComm *51*, 7737–7740.

Heine, J., and Muller-Buschbaum, K. (2013). Engineering metal-based luminescence in

coordination polymers and metal-organic frameworks. Chem. Soc. Rev. *42*, 9232–9242.

Hinckley, D.A., Seybold, P.G., and Borris, D.P. (1986). Solvatochromism and thermochromism of rhodamine solutions. Spectrochim. Acta *42*, 747–754.

Kamtekar, K.T., Monkman, A.P., and Bryce, M.R. (2010). Recent advances in white organic light-emitting materials and devices (WOLEDs). Adv. Mater. *22*, 572–582.

Kanagaraj, S., Puthanveedu, A., and Choe, Y. (2019). Small molecules in light-emitting electrochemical cells: promising light-emitting materials. Adv. Funct. Mater. *30*, 1907126.

Khader, M.A. (2008). Lasing characteristics of rhodamine B and rhodamine 6G as a sensitizer in sol–gel silica. Opt. Laser Technol. *40*, 445–452.

Li, J., Yuan, S., Qin, J.S., Pang, J., Zhang, P., Zhang, Y., Huang, Y., Drake, H.F., Liu, W.R., and Zhou, H.C. (2020). Stepwise assembly of turn-on fluorescence sensors in multicomponent metal-organic frameworks for in vitro cyanide detection. Angew. Chem. Int. Ed. *59*, 9319–9323.

Lin, R.-B., Xiang, S., Li, B., Cui, Y., Qian, G., Zhou, W., and Chen, B. (2019). Our journey of developing multifunctional metal-organic frameworks. Coord. Chem. Rev. *384*, 21–36.

Luo, T.Y., Das, P., White, D.L., Liu, C., Star, A., and Rosi, N.L. (2020). Luminescence "Turn-On" detection of gossypol using In^{3+}-based metal-organic frameworks and Ln^{3+} salts. J. Am. Chem. Soc. *142*, 2897–2904.

Lustig, W.P., Mukherjee, S., Rudd, N.D., Desai, A.V., Li, J., and Ghosh, S.K. (2017). Metal-organic frameworks: functional luminescent and photonic materials for sensing applications. Chem. Soc. Rev. *46*, 3242–3285.

Mieno, H., Kabe, R., Notsuka, N., Allendorf, M.D., and Adachi, C. (2016). Long-lived room-temperature phosphorescence of coronene in zeolitic imidazolate framework ZIF-8. Adv. Opt. Mater. *4*, 1015–1021.

Mollick, S., Mandal, T.N., Jana, A., Fajal, S., Desai, A.V., and Ghosh, S.K. (2019). Ultrastable luminescent hybrid bromide perovskite@MOF nanocomposites for the degradation of organic pollutants in water. ACS Appl. Nano Mater. *2*, 1333–1340.

Nauruzbayeva, J., Sun, Z., Gallo, A., Jr., Ibrahim, M., Santamarina, J.C., and Mishra, H. (2020). Electrification at water-hydrophobe interfaces. Nat. Commun. *11*, 5285.

Phan, A., Doonan, C.J., Uribe-Romo, F.J., Knobler, C.B., O'keeffe, M., and Yaghi, O.M. (2010). Synthesis, structure, and carbon dioxide capture properties of zeolitic imidazolate frameworks. Acc. Chem. Res. *43*, 58–67.

Qin, S.-J., and Yan, B. (2018). Dual-emissive ratiometric fluorescent probe based on Eu^{3+}/C-dots@MOF hybrids for the biomarker diaminotoluene sensing. Sens. Actuator B Chem. *272*, 510–517.

Sagoo, S.K., and Jockusch, R.A. (2011). The fluorescence properties of cationic rhodamine B in the gas phase. J. Photochem. Photobiol. A *220*, 173–178.

Stassen, I., Burtch, N., Talin, A., Falcaro, P., Allendorf, M., and Ameloot, R. (2017). An updated roadmap for the integration of metal-organic frameworks with electronic devices and chemical sensors. Chem. Soc. Rev. *46*, 3185–3241.

Stobiecka, M., and Hepel, M. (2011). Multimodal coupling of optical transitions and plasmonic oscillations in rhodamine B modified gold nanoparticles. Phys. Chem. Chem. Phys. *13*, 1131–1139.

Takashima, Y., Martinez, V.M., Furukawa, S., Kondo, M., Shimomura, S., Uehara, H., Nakahama, M., Sugimoto, K., and Kitagawa, S. (2011). Molecular decoding using luminescence from an entangled porous framework. Nat. Commun. *2*, 168.

Tang, Y., He, W., Lu, Y., Fielden, J., Xiang, X., and Yan, D. (2014). Assembly of ruthenium-based Complex into metal–organic framework with tunable area-selected luminescence and enhanced photon-to-electron conversion efficiency. J. Phys. Chem. C *118*, 25365–25373.

Titov, K., and Tan, J.-C. (2016). Facile patterning of electrospun polymer fibers enabled by electrostatic lensing interactions. APL Mater. *4*, 086107.

Wang, J., Zhang, Y., Yu, Y., Ye, F., Feng, Z., Huang, Z., Liu, X., and Zhou, X. (2019). Spectrally flat white light emission based on red-yellow-green-blue dye-loaded metal-organic frameworks. Opt. Mater. *89*, 209–213.

Yao, C.X., Zhao, N., Liu, J.C., Chen, L.J., Liu, J.M., Fang, G.Z., and Wang, S. (2020). Recent progress on luminescent metal-organic framework-involved hybrid materials for rapid determination of contaminants in environment and food. Polymers *12*, 691.

Yin, H., Khosravi, A., O'connor, L., Tagaban, A.Q., Wilson, L., Houck, B., Liu, Q., and Lind, M.L. (2017). Effect of ZIF-71 particle size on free-standing ZIF-71/PDMS composite membrane performances for ethanol and 1-butanol removal from water through pervaporation. Ind. Eng. Chem. Res. *56*, 9167–9176.

Yoo, J., Ryu, U., Kwon, W., and Choi, K.M. (2019). A multi-dye containing MOF for the ratiometric detection and simultaneous removal of $Cr_2O_7^{2-}$ in the presence of interfering ions. Sens. Actuator B Chem. *283*, 426–433.

Zhang, H., Song, H., Yu, H., Li, S., Bai, X., Pan, G., Dai, Q., Wang, T., Li, W., Lu, S., et al. (2007). Modified photoluminescence properties of rare-earth complex/polymer composite fibers prepared by electrospinning. Appl. Phys. Lett. *90*, 103103.

Zhang, Y., Gutiérrez, M., Chaudhari, A.K., and Tan, J.C. (2020). Dye-encapsulated zeolitic imidazolate framework (ZIF-71) for fluorochromic sensing of pressure, temperature, and volatile solvents. ACS Appl. Mater. Inter. *12*, 37477–37488.

Zhao, H., Ni, J., Zhang, J.J., Liu, S.Q., Sun, Y.J., Zhou, H., Li, Y.Q., and Duan, C.Y. (2018). A trichromatic MOF composite for multidimensional ratiometric luminescent sensing. Chem. Sci. *9*, 2918–2926.

STAR★METHODS

KEY RESOURCES TABLE

REAGENT or RESOURCE	SOURCE	IDENTIFIER
Chemicals, peptides, and recombinant proteins		
4,5-Dichloroimidazole	Alfa Aesar	CAS: 15965-30-7
Triethylamine	Alfa Aesar	CAS: 121-44-8
Rhodamine B	Alfa Aesar	CAS: 81-88-9
Zinc acetate dihydrate	Thermo Fisher Scientific	CAS: 5970-45-6
HSV900 poly(vinylidene fluoride)	Kynar	CAS: 24937-79-9
Deposited data		
ZIF-71 crystal structure	(Phan et al., 2010)	CCDC code: GITVIP

RESOURCE AVAILABILITY

Lead contact

Further information and requests for resources and reagents should be directed to and will be fulfilled by the lead contact, Prof. Jin-Chong Tan (jin-chong.tan@eng.ox.ac.uk).

Materials availability

Raw materials used in the study are commercially available.

Data and code availability

This study did not generate computer code. All data and analytical methods are available in the main text or in supplemental information section. The ZIF-71 crystal structure data used is from The Cambridge Crystallographic Data Center (CCDC code: GITVIP). Any additional information required to reanalyze the data reported in this paper is available from the lead contact upon request.

METHOD DETAILS

Synthesis of RhB@ZIF-71 by using HCR method

15 mL methanol solution of 4,5-dichloroimidazole (dcIm, 9.6 mmol) plus triethylamine (NEt_3, 9.6 mmol) was combined with 1 mL methanol solution of rhodamine B (RhB, 0.05 mmol). After the combination, 15 mL clear solution of zinc acetate (2.4 mmol) was immediately added into the mixture, producing a sol-like product. Then the product was washed thoroughly three times using methanol to remove the guests adhered to the MOF surface. The nanocrystals of RhB@ZIF-71 were separated from the suspension by centrifugation at 8000 rpm for 10 min.

Preparation of RhB@ZIF-71 and RhB in PVDF solution

The electrospinning polymer solution was prepared by dissolving 15 g HSV900 polyvinylidene fluoride (PVDF) powder in 94 g dimethylacetamide (DMA), to yield 13.7 wt.% PVDF in DMA. Then the appropriate amount of RhB@ZIF-71 in acetone solution was added to the PVDF in DMA solution to make the mass ratio of RhB@ZIF-71 to PVDF of 1:99, 3:97, 5:95 and the volume ratio of DMA to acetone was 3:1. According to the Beer-Lambert Law, an acetone solution of RhB with the same absorbance as RhB@ZIF-71 acetone solution was prepared (Figure S9), and then the RhB acetone solution with the same weight as RhB@ZIF-71 acetone solution was used to mix with PVDF.

Electrospinning

Electrospinning was carried out at 10.5 kV from a DC high-voltage generator. The PVDF solution was supplied to a G19 needle emitter (nozzle) with a blunt tip via a syringe pump at a processing rate of 8–20 μL/min. The distance from the collector (aluminum foil or diamond-shaped mesh) to the tip was 16 cm. Further details about the formation of the textured mat by electrospinning can be found in ref

(Titov and Tan, 2016), where they described the application of electrostatic lensing interaction to fabricate fibers with predefined orientations mirroring the architecture of a conductive wire mesh.

Materials characterization

The structures and morphologies were examined under scanning electron microscopy (SEM; Hitachi TM3030Plus and $LYRA_3$ GM TESCAN) and an atomic force microscope (Neaspec s-SNOM under tapping mode). The PXRD pattern was recorded using a Rigaku MiniFlex with a Cu Kα source (1.541 Å). UV-2600 UV-Vis diffuse reflectance spectrophotometer (Shimadzu) equipped with an integrating sphere was used to measure the reflectance spectra of the solid samples. The melting temperatures were measured by using TA Instruments DSC Q2000. ATR-FTIR absorption spectra were recorded by using a Nicolet iS10 FTIR spectrometer. An FS5 spectrofluorometer (Edinburgh Instruments) equipped with different accessories was used to measure the steady-state emission and excitation spectra, quantum yield (QY), fluorescent lifetime by time-correlated single-photon counting (TCSPC), and thermochromic response.

Paper III: Nanoconfinement of Tetraphenylethylene in Zeolitic Metal-Organic Framework for Turn-on Mechanofluorochromic Stress Sensing

Applied Materials Today 27 (2022) 101434

Contents lists available at ScienceDirect

Applied Materials Today

journal homepage: www.elsevier.com/locate/apmt

Nanoconfinement of tetraphenylethylene in zeolitic metal-organic framework for turn-on mechanofluorochromic stress sensing

Yang Zhang[a], Tao Xiong[a], Annika F. Möslein[a], Samraj Mollick[a], Vishal Kachwal[a], Arun Singh Babal[a], Nader Amin[b], Jin-Chong Tan[a,*]

[a] Multifunctional Materials & Composites (MMC) Laboratory, Department of Engineering Science, University of Oxford, Parks Road, Oxford OX1 3PJ, UK
[b] Department of Chemistry, University of Oxford, Mansfield Road, Oxford OX1 3TA, UK

ARTICLE INFO

Article history:
Received 29 October 2021
Revised 16 February 2022
Accepted 25 February 2022

Keywords:
Aggregation-induced emission (AIE)
Metal-organic framework (MOF)
Turn-on mechanofluorochromism
Guest@MOF
Photonic pressure sensor

ABSTRACT

Mechanofluorochromic materials are of great significance for the fabrication of innovative sensors and optoelectronics. However, efficient mechanofluorochromic materials are rarely explored due to the deficiency of existing design strategies. Here, we demonstrate the incarceration of aggregation-induced emission (AIE) materials within metal-organic framework (MOF) single crystals to construct a composite system with turn-on mechanofluorochromism. A new type of AIE@MOF material was designed: integrating a zeolitic MOF (ZIF-71) and tetraphenylethylene (TPE, a topical AIE material) to generate a TPE@ZIF-71 system with exceptional turn-on type mechanofluorochromism. Using terahertz vibrational spectroscopy, we show the unique fluorochromism mainly emanates from the enhanced nanoconfinement effect exerted by ZIF-71 host on TPE guest under pressure. Compared with pure TPE, we demonstrate the nanoconfinement in AIE@MOF not only changes the TPE's turn-off type sensing behavior to a turn-on type, but boosts the original sensitivity markedly by tenfold. Significantly, because ZIF-71 prevents the spontaneous recrystallization of TPE upon unloading, this allows TPE@ZIF-71 to record the stress history. This is the first demonstration of the Guest@MOF system combining the concepts of AIE and MOF; its promising properties and potential engineering applications will stimulate new directions pertaining to luminescent stress sensors and smart optics.

1. Introduction

Mechanofluorochromic material is a new type of smart material that changes its fluorescent color when subjected to an external mechanical force stimulus [1,2]. This kind of material has received extensive attention in the field of solid-state optics because of its potentially wide applications in several advanced technologies [2–4], such as fluorescence switches [5], mechanosensors [6–8], optoelectronics [9], and data storage [10].

Hitherto, there are only a few reported examples of materials that can exhibit efficient mechanofluorochromism by means of physical structural change [1,11]. The reason is that most of the existing fluorescent materials often have no emission in the solid-state due to the aggregation-caused quenching (ACQ) effect [12]. Even if some are able to show a weak mechanofluorochromic sensing behavior, they are essentially the "turn-off" types, which leads to difficulty in fabricating practical applications, because turn-off type sensors are easily affected by external environmental factors, such as temperature and humidity, causing the intensity of the emission signal to decrease and interfere with the sensing accuracy [13].

It has been proposed that one of the most effective ways to overcome the aforementioned obstacles is to prepare a "turn-on" type mechanofluorochromic material, which is not negatively affected by the ACQ effect [14–18]. Therefore, increasingly more researchers have turned their attention to studying materials with aggregation-induced emission (AIE) property. The AIE materials, contrary to ACQ materials, have zero or only weak emission when in a diluted solution state but emit strong luminescence in the aggregated state [19], and they may also possess mechanofluorochromic properties to some extent [1].

In the field of AIE materials, one of the most well-known examples is tetraphenylethylene (TPE) [14,20–24]. Nonetheless, TPE only has a weak turn-off type sensing ability in the lower pressure range under 1.5 GPa because of additional non-radiative decay caused by closer intermolecular interactions [25]. Worse still, due to its spontaneous recrystallization, the stress-induced luminescence of TPE will immediately reverse to its (original) low-intensity state once the applied pressure is removed [25,26], which hin-

* Corresponding author.
E-mail address: jin-chong.tan@eng.ox.ac.uk (J.-C. Tan).

https://doi.org/10.1016/j.apmt.2022.101434
2352-9407/

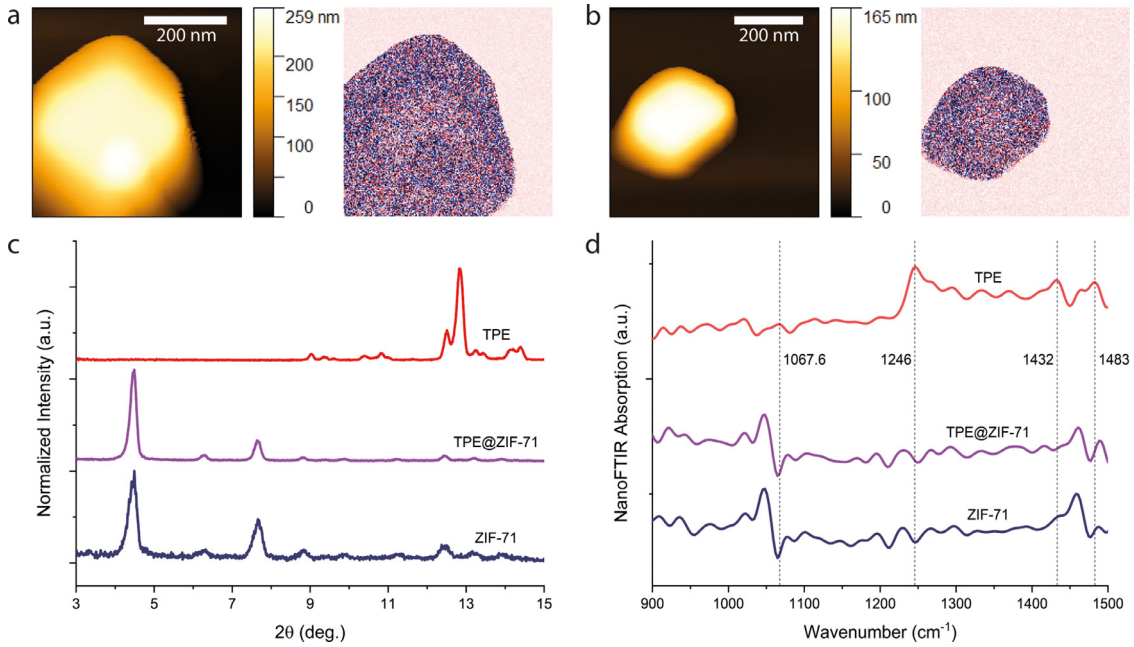

Fig. 1. (a) and (b) Atomic force microscopy (AFM) images (left) and optical phase images (right) of ZIF-71 and TPE@ZIF-71, respectively. (c) PXRD patterns of the TPE, TPE@ZIF-71, and ZIF-71 powder. (d) Near-field IR absorption spectra of TPE, TPE@ZIF-71, and ZIF-71 crystals.

ders measurement from being done *ex situ* (upon force removal). Many researchers have attempted to use organic chemistry methods to synthesize TPE derivatives for improving and optimizing its mechanofluorochromic properties [1,12,27], but these methods have limited success, and the complex synthesis also restricted its further development.

To address these challenges and promote the engineering application of TPE, herein, we propose the use of metal-organic frameworks (MOFs) as a 'host' and TPE as a 'guest' to form a TPE@MOF system. Notably, MOFs have highly porous and extended crystalline structures, giving themselves the ability to capture, isolate and stabilize other emitter molecules, including bulky fluorophores [28–36]. We hypothesize that the nanoscale caging effect induced by MOF pores could modify or enhance the mechanofluorochromic performance of the pristine TPE molecules.

In this work, we report how TPE can be encapsulated into the zeolitic imidazolate framework-71 (ZIF-71) single crystal through an easy-to-implement one-pot synthetic method. Compared with the weak turn-off type sensing performance of pure TPE in the $<$ 1.5 GPa pressure range, the introduction of ZIF-71 successfully allows the obtained TPE@ZIF-71 materials to exhibit turn-on sensing and enhances the sensitivity by 10 folds. Furthermore, the ZIF-71 solves the problem of spontaneous recrystallization in TPE, enabling the retainment of mechanofluorochromic behavior after the pressure is removed. Unlike the poor processability of other guest@MOF systems, we have successfully prepared turn-on type pressure sensing fibers and membranes with industrialization potential by leveraging TPE@ZIF-71/polymer composites. To the best of our knowledge, the TPE@ZIF-71 system is the first guest@MOF system to realize the turn-on type mechanofluorochromic sensing capability. This work has paved a new pathway for practical engineering applications of AIE-based mechanofluorochromic materials.

2. Synthesis and structure of TPE@ZIF-71

The synthesis of TPE@ZIF-71, known as the one-pot synthesis method, is straightforward: by directly mixing solutions of zinc acetate, 4,5-dichloroimidazole (dcIm), and TPE at room temperature. The full details are given in the Experimental Section. Fig. 1a and 1b show the morphology of the ZIF-71 and TPE@ZIF-71 crystals obtained, revealing the nominal size of the crystals to be ~200 nm. In addition, we performed powder X-ray diffraction (PXRD) characterization for the TPE, ZIF-71, and TPE@ZIF-71 samples. The PXRD patterns (Fig. 1c) of TPE@ZIF-71 and ZIF-71 are indistinguishable from each other, and there is no Bragg peak belonging to TPE that also shows in the TPE@ZIF-71 spectrum. The patterns suggest that the crystal structure of ZIF-71 has formed normally, and the added TPE molecules do not affect the long-range periodicity of the ZIF-71 structure.

To ensure that the TPE is captured by the ZIF-71 pores instead of being attached to the surface, we conducted near-field infrared nanospectroscopy characterization. This technique combines scattering-type scanning near-field optical microscopy (s-SNOM) and nano-Fourier transform infrared (nanoFTIR) spectroscopy, which can perform detailed chemical and physical analysis on the surface of the nanocrystal to determine the presence/absence of guest material on the external surface of crystals [37]. The obtained s-SNOM optical phase images (Fig.1a and 1b) show that the surface composition of the ZIF-71 and TPE@ZIF-71 crystals are very uniform, and there are no clusters/regions of guest material on the surface. The nanoFTIR spectra of TPE, TPE@ZIF-71 and ZIF-71 (Fig. 1d) reveal that the ZIF-71 and TPE@ZIF-71 are almost identical. Moreover, combined with the simulated infrared vibrations of TPE using density functional theory (DFT) (see Fig. S1, Supporting Information), it can be found that the main peaks of TPE (1067.6 cm^{-1}, 1432 cm^{-1}, 1483 cm^{-1}, which correspond to the C_{ph}–H in-plane bending, and 1246 cm^{-1}, which corresponds to the C–C_{ph} asymmetric stretching and the C_{ph}–H in-plane bending) are not detected in the IR spectrum of TPE@ZIF-71. Therefore, it is reasonable to believe that the TPE is encapsulated and not attached to the exterior of the crystals.

Similarly, using Fourier transform infrared spectroscopy with attenuated total reflection (ATR-FTIR) characterization (Fig. S2) of the bulk polycrystalline sample, the traces of TPE molecules were not found in the TPE@ZIF-71 spectrum as well. Subsequently, by employing thermogravimetric analysis (TGA, Fig. S3) and solution ^{1}H nuclear magnetic resonance (NMR) spectroscopy (Fig. S4), we found that the material contains only a low concentration of TPE

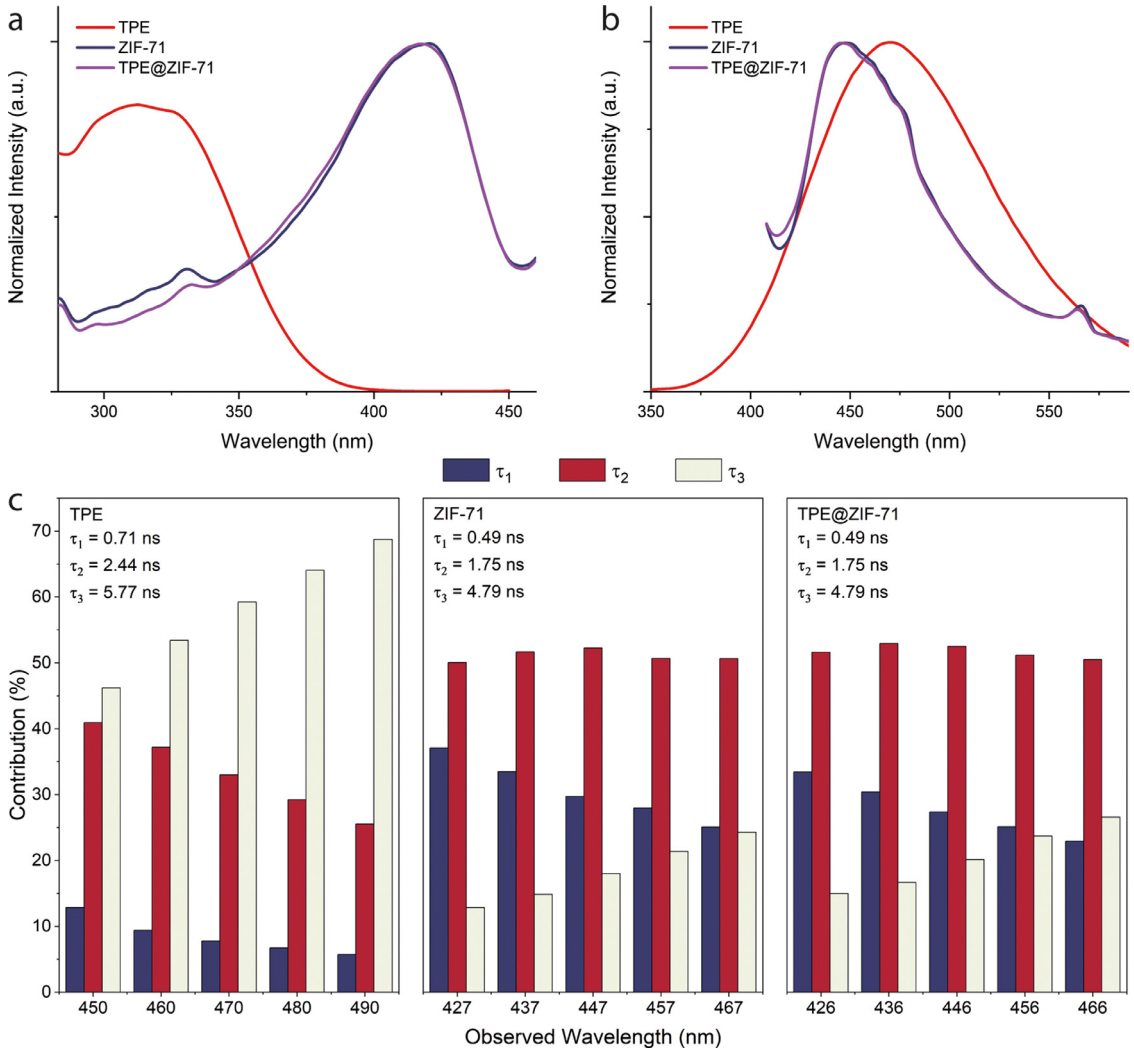

Fig. 2. (a) Normalized excitation spectra, (b) emission spectra and (c) lifetime data of TPE suspension (THF-water mixture containing 99% volume fraction of water), ZIF-71, and TPE@ZIF-71 powder. Time constants (τ_i) and fractional contributions from fluorescent lifetime measurements.

molecules: from TGA ~0.24 wt.%, and from NMR the molar ratio of TPE: dcIm = 0.00029 (guest loading calculated is 1 TPE for every 146 cages of ZIF-71). Additionally, according to the DFT simulation, the size of a TPE dimer is about 18.06 Å (including the *van der Waals* surface, see Fig. S5); because the minimum distance inside the ZIF-71 pore is 16.58 Å, this means that most TPE guest can only exist as a monomer in the pores of the ZIF-71 host.

3. Fluorescent properties of TPE@ZIF-71

To understand the photophysical properties of the resulting composite system, we performed fluorescence spectroscopy on the TPE (pristine guest), ZIF–71 (pristine host), and TPE@ZIF-71 samples (Fig. 2). The excitation and emission spectra (Fig. 2a and 2b) show that the luminescence of ZIF-71 and TPE@ZIF-71 are almost identical to each other. The excitation peak (300–350 nm) and emission peak (470 nm) pertaining to the pure TPE molecules do not appear in the TPE@ZIF-71 spectra. Therefore, we established that virtually all the fluorescence of TPE@ZIF-71 powder comes from the ZIF-71 itself, which indicates that the TPE is well dispersed in the ZIF-71, and the ZIF-71 pore does not effectively restrict the intramolecular vibrations of TPE in the absence of an external mechanical force stimulus (or pressure). Besides, ZIF-71 possesses an emission peak at 565 nm (Fig. 2b), which is attributed to the ligand-metal charge transfer (LMCT) as identified by previous research [38]. We may surmise that there is initially no strong interaction between the TPE and ZIF-71, because the encapsulation of TPE materials does not lead to the disappearance of the LMCT peak.

Using the time-correlated single-photon-counting (TCSPC) technique to analyze the lifetime data of TPE@ZIF-71, ZIF-71, and TPE, we further verified the assumption made above. The lifetimes (τ) of TPE@ZIF-71 and ZIF-71 shown in Fig. 2c and Table S1 are the same, and the contributions (c) for each τ are also comparable, which proves that the fluorescence of TPE@ZIF-71 powder originates from the ZIF-71 alone, thereby confirming that: (i) TPE molecules are uniformly dispersed in ZIF-71, and (ii) there is no strong interaction between TPE and ZIF-71.

4. Mechanofluorochromism of TPE@ZIF-71

To study the mechanofluorochromism of the TPE@ZIF-71 system, we compressed it into pellets under different pressures using a hydraulic press. Fig. 3a and 3b show the color of the pellets viewed under ambient daylight and UV light (365 nm), respectively. Clearly, it can be seen with the naked eye that TPE@ZIF-71 exhibits a turn-on type mechanofluorochromic behavior even in the low-pressure range below 350 MPa. Conspicuously, the quantum yield (QY) of TPE@ZIF-71 pellets (Table S2) increases with increasing pelleting pressure. Moreover, the fluorescent property of

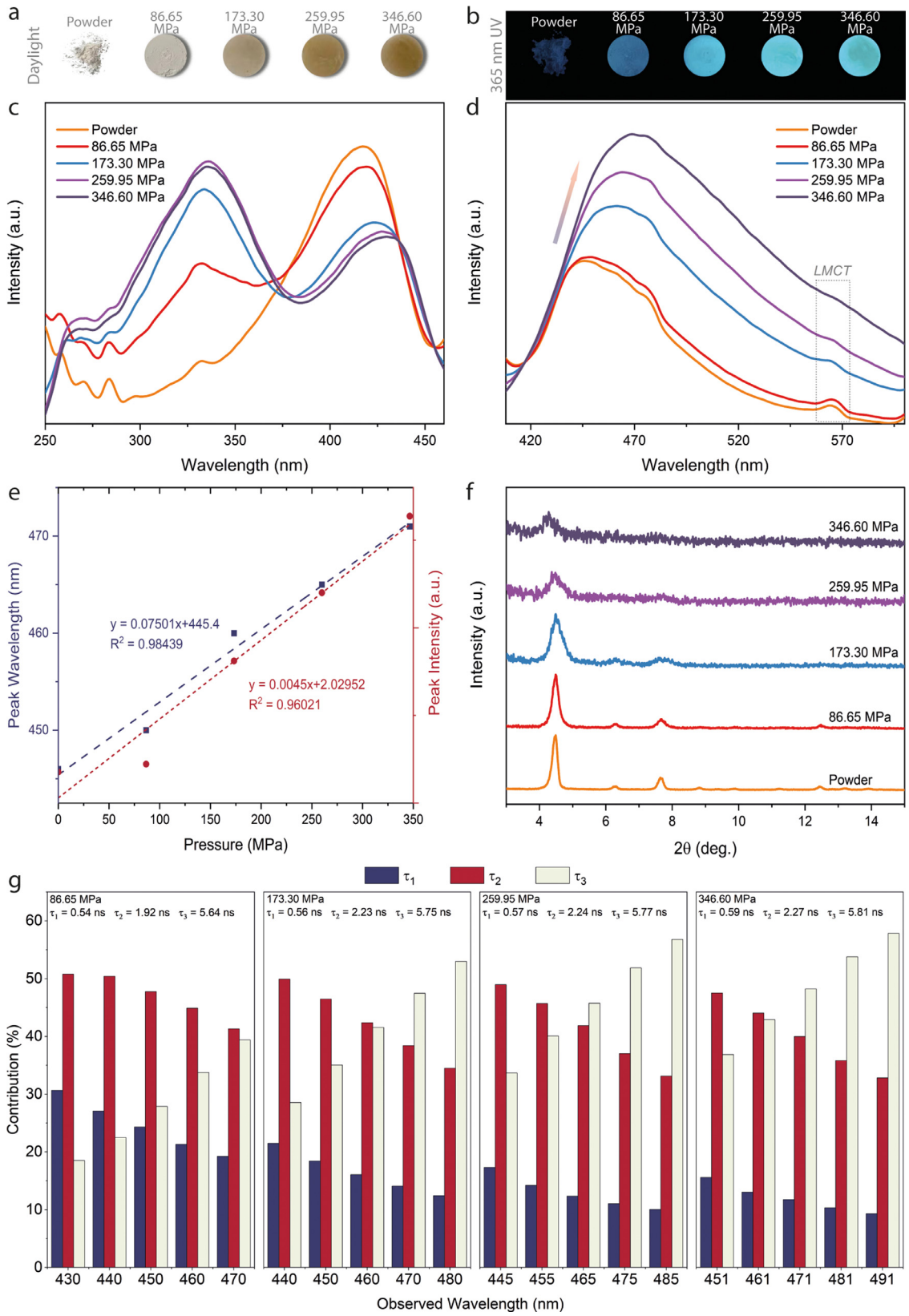

Fig. 3. (a) TPE@ZIF-71 pellets prepared under different pressures, their colors viewed in ambient light, and (b) their fluorescence observed under the 365 nm UV lamp. (c) Normalized excitation spectra and (d) normalized emission spectra of the TPE@ZIF-71 powder and pellets. (e) Linear relationship between the emission peak wavelength, peak intensity, and the applied pelleting pressure for TPE@ZIF-71. (f) PXRD patterns of the TPE@ZIF-71 powder and pellets. (g) Time constants (τ_i) and fractional contributions from fluorescence lifetime measurements of TPE@ZIF-71 pellets.

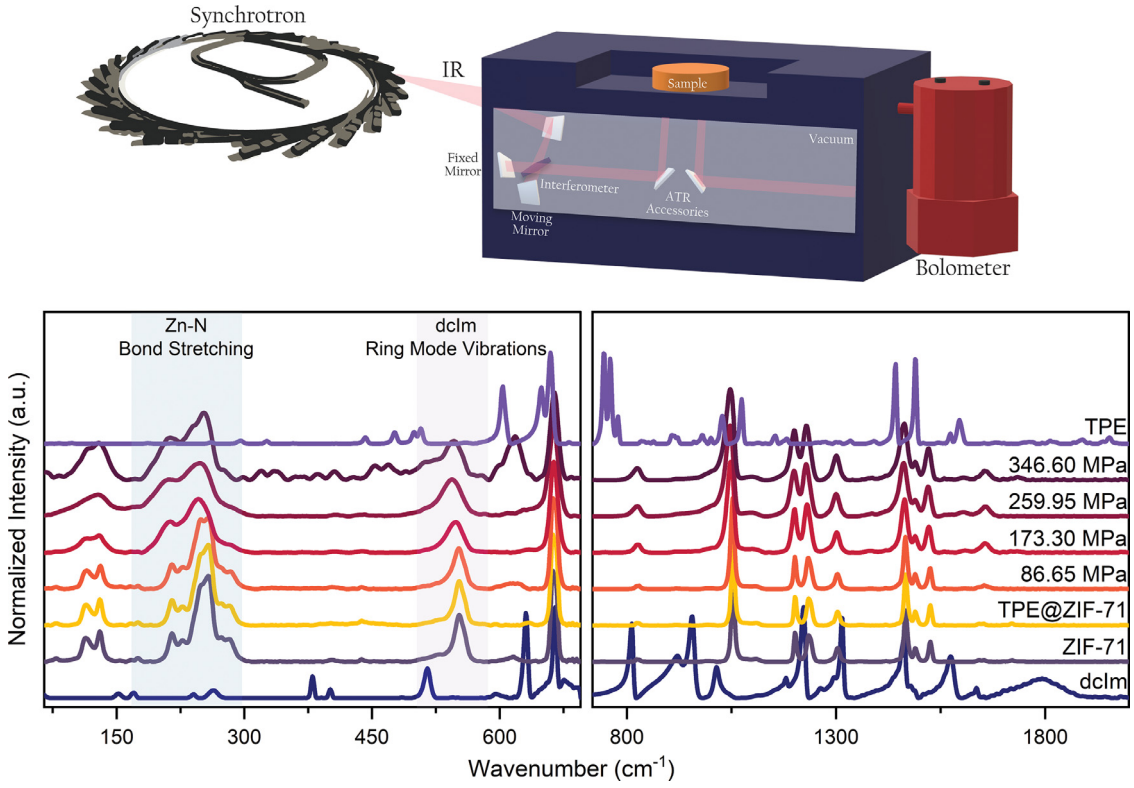

Fig. 4. Diamond Light Source synchrotron used for SR-FTIR characterization (upper row); SR-FTIR spectra in the 65–2000 cm^{-1} region (left: spectral region < 700 cm^{-1} collected using a bolometer; right: > 700 cm^{-1} collected from a standard detector).

the TPE@ZIF-71 pellets is maintained after pressure removal, which indicates that the nanoconfinement of ZIF-71 suppresses the spontaneous recrystallization of TPE molecules.

Then the excitation and emission spectra of these pellets were measured and analyzed (Fig. 3). The excitation spectrum (Fig. 3c) reveals that with the increase of pelleting pressure, the intensity of the peak belonging to TPE in the range of 300–350 nm rises, and there is a small redshift, while the intensity of the peak belonging to ZIF-71 (400–450 nm) gradually decreases and a greater redshift appears. The emission diagram (Fig. 3d) shows that the TPE@ZIF-71 pellets present a larger fluorescence intensity and peak wavelength under higher pelleting pressure. The observed trend of increasing intensity and shifting wavelength also shows a certain degree of linear relationship with the applied nominal pressure (Fig. 3e). From these phenomena, we inferred that as the pressure increases, the TPE molecules within the ZIF-71 pore are becoming more and more confined, resulting in a stronger caging effect. This causes more restrictions to the intramolecular vibrations of TPE, giving a brighter red-shifted emission [38,39]. In contrast, as a control experiment, a mechanically mixed powder of TPE and ZIF-71 was also prepared and subjected to the same pressure. It can be seen that, without the guest-host caging effect, this physically combined powder does not exhibit any mechanochromism under that same condition (Fig. S6).

Detailed analysis of lifetime data further verifies our speculation. From Fig. 3g and Table S3, it is clear that the lifetimes τ_1, τ_2, and τ_3 of pellets rise with the incremental pressure, and the values become closer to the ones of pure TPE. In particular, when the pressure is above 259.95 MPa, the value of τ_3 approximates to or even exceeds the τ_3 of pure TPE. These findings prove that as the pressure increases, the emission of TPE starts to dominate, which results from the fact that the intramolecular vibrations of TPE are becoming more and more restricted. Moreover, Fig. 3g and Table S3 also indicate that under low pressure, the relationship between the contributions (c) of each lifetime is: $c_2 > c_1 > c_3$, and when the pressure increases, c_3 rises significantly, while c_1 decreases distinctly. The reason for this variation is that the fluorescence of TPE within the pores is turning increasingly dominant, because the contribution of pure ZIF-71 is $c_2 > c_1 > c_3$ and the contribution of pure TPE is $c_3 > c_2 > c_1$ (Fig. 2c and Table S1). Hence, it follows that the data of lifetime further confirm our hypothesis on the relationship between the deformed structure and fluorescence property of TPE@ZIF-71.

Using synchrotron radiation Fourier-transform infrared spectroscopy (SR-FTIR) in Beamline B22 MIRIAM at the Diamond Light Source (Oxfordshire, UK), more evidence was obtained to substantiate the proposed mechanism. As shown in Figs. 4 and S7, we identified that: (i) the collective vibrational modes of TPE@ZIF-71 in the terahertz region (< 325 cm^{-1}, < 10 THz) broaden gradually with an increase of pelleting pressure; (ii) the vibrational peaks in the region of 490–590 cm^{-1} (< 20 THz) decrease in their wavenumbers and progressively broaden as the pressure increases. From literature [40], the former mode corresponds to the Zn–N bond stretching of ZIF-71, and the widening trend indicates that the framework is becoming structurally distorted or more amorphized under pressure; the latter spectral change is attributed to the dcIm ring mode vibrations, and the reduced wavenumbers represent the longer bond length, hence reflecting a weaker bond strength. The results support the notion that as the pressure increases, the TPE molecule begins to interact with the dcIm linker, and this intermolecular interaction becomes increasingly stronger with higher stress. The SR-FTIR spectra therefore confirm our proposed theory that the TPE experiences a more significant mechanically-induced caging effect as the pressure increases.

On the other hand, from the XRD patterns of pellets (Fig. 3f), we could observe a progressive decline in intensity and sharpness of the XRD peaks, indicating that the crystalline structure of ZIF-71 is being amorphized with greater pressure. The evolving XRD

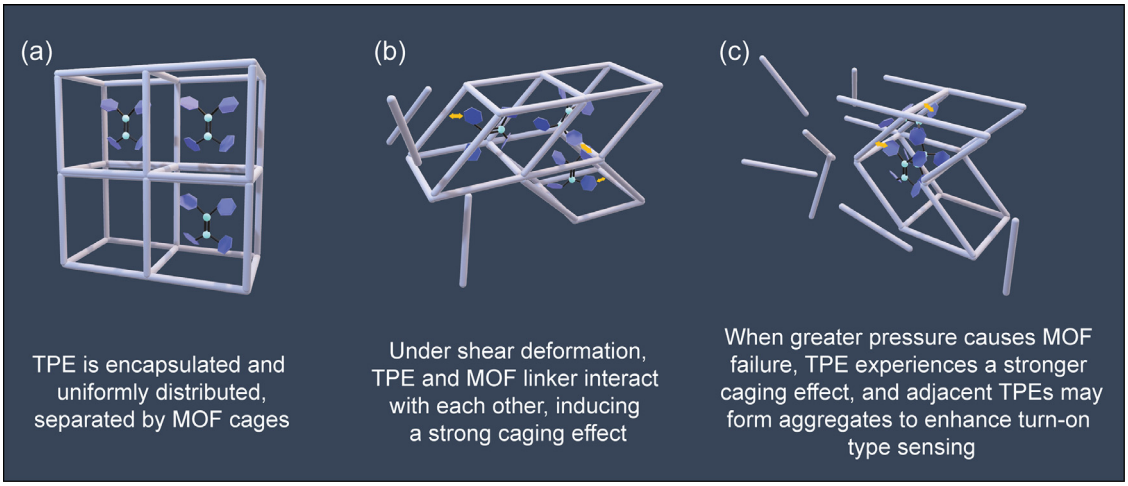

Scheme 1. (a) Proposed deformation of the TPE@ZIF-71 structure subject to a mechanical pressure. White sticks represent the secondary building units (SBUs) of ZIF-71. Purple hexagons, cyan balls, and black sticks represent the TPE molecules. Yellow arrows represent possible interactions. (b) As pressure increases, the ZIF-71 structure begins to mechanically deform and shear under stress, resulting in a strong caging effect. (c) When pressure continues to increase further to cause framework fracture, some ZIF-71 pores will collapse and become amorphized, causing TPE molecules located in adjacent pores to form aggregates.

patterns lead us to propose that, upon the collapse of the initially periodic framework, the TPE molecules in the adjacent pores could form new aggregates to help enhance the emission, contributing to the further rise of intensity and redshift of the excitation and emission spectra. The mechanically-induced rupture of the crystalline structure also results in the decrease and redshift of the excitation of ZIF-71 (375–450 nm, Fig. 3c). As the pressure progresses, the framework is gradually amorphized. Such a structural collapse could be triggered by shear deformation [41,42], thus reducing the distance between the linkers. Therefore, more interaction will occur between the discrete linkers or the remaining framework, causing the excitation peak to fall and redshift. The gradual disappearance of the 565 nm LMCT peak also proves our inference. Based on the systematic findings from photophysical analysis combined with structural evolution data evidenced from XRD patterns, the proposed mechanism of TPE@ZIF-71 mechanofluorochromism can be illustrated in Scheme 1.

Through the comparison of other TPE@MOF composites, the proposed mechanofluorochromic mechanism is further validated. Meanwhile, the TPE@ZIF-71 system is also proven to have better sensitivity than other TPE@MOF systems. Here we chose another two “stable” MOFs, UiO-67 (UiO: University of Oslo) and MIL-68(In) (MIL: Materials Institute Lavoisier), to encapsulate TPE. Fig. S8 shows the mechanofluorochromic behavior of TPE@ZIF-71, TPE@UiO-67, and TPE@MIL-68(In) under the same pressure. It can be seen with the naked eye that TPE@ZIF-71 exhibits a more considerable peak intensity increase and wavelength shift as the pressure rises. The reason is closely related to the mechanical rigidity of the different frameworks. Due to the different organic linkers in the MOF structure, MIL-68(In) and UiO-67 are perceived to be more rigid than ZIF-71 [43–45], resulting in TPE experiencing a weaker caging effect inside MIL-68(In) and UiO-67, which explains why they both did not display as good of a sensing performance compared with TPE@ZIF-71. Concomitantly, this also proves the proposed turn-on sensing mechanism from another perspective.

Unlike other delicate guest@MOF systems [39], TPE@ZIF-71 offers facile processability and unique turn-on luminescence under stress. This further motivates us to combine TPE@ZIF-71 with polyurethane (PU) and polyvinylidene difluoride (PVDF) matrices to prepare TPE@ZIF-71/PU fiber by electrospinning and TPE@ZIF-71/PVDF membrane by doctor-blade technique. Fig. S9 shows that both the fibers and membranes maintain the excellent turn-on type mechanochromism and can realize fluorescence sensing under compressive stress. To our best knowledge, this is also the first turn-on type mechanofluorochromic electrospun fiber and membrane to be demonstrated to date. The detailed performance of these proof-of-concept TPE@ZIF-71/polymer composites and their practical deployment warrants further investigations.

5. Conclusions

In summary, through a simple one-pot synthesis method, we successfully encapsulated the bulky TPE monomers as guest into the pores of the ZIF-71 host framework. The new TPE@ZIF-71 composite based on the Guest@MOF concept, for the first time, exhibits the turn-on mechanofluorochromic sensing behavior under stress. Furthermore, TPE@ZIF-71 can retain the results of the mechanofluorochromism after the pressure is removed. Utilizing far-infrared vibrational spectroscopy to probe the THz collective modes of TPE@ZIF-71, it was determined that this stress-induced response mainly originates from the caging effect bestowed by MOF pores upon the TPE molecules, where (permanent) plastic deformation of the ZIF-71 framework constraints the intramolecular rotation and motion of TPE under stress/pressure. Compared with pure TPE and other TPE@MOF systems, the introduction of ZIF-71 not only reverses the turn-off type sensing of TPE (observed at pressure < 1.5 GPa) [25] to a turn-on type, but further boosts the sensitivity of TPE by 10 folds to detect a mechanical force stimulus (Table S4). The TPE@ZIF-71 system reported herein is the first study of its kind to combine AIE materials with stable MOFs, the high-sensitivity fluorescent properties and the potential engineering application of which have opened up a new way to design bespoke AIE materials by harnessing the nanoscale confinement effect.

Experimental Section

Synthesis of TPE@ZIF-71: 90 mL methanolic solution of 19.2 mmol 4,5-dichloroimidazole (dcIm), 10 mL tetrahydrofuran (THF) solution of 0.2 mmol tetraphenylethylene (TPE), and 90 mL methanolic solution of 4.8 mmol zinc acetate were quickly combined under stirring. After stirring for 24 h, the sample was centrifuged at 8000 rpm for 10 min to remove excess reactants, and then washed 4 times (2 times with THF, 2 times with methanol). The crystals of TPE@ZIF-71 were separated from the suspension by centrifugation at 8000 rpm for 10 min. The procedure for preparing ZIF-71 was the same, except no TPE was added.

Synthesis of TPE@UiO-67: 68 mL dimethylformamide (DMF) solution of 4.8 mmol biphenyl-4,4′- dicarboxylic acid (BPDC) plus triethylamine (NEt_3, 14.4 mmol) was combined with 10 mL THF

solution of 0.2 mmol TPE. After the combination, 20 mL acetic acid solution of 4.8 mmol zirconium chloride was heated at 80 °C for one hour and then added into the mixture, producing a sol-like product. Subsequently, the product was heated at 120 °C for 24 h and washed thoroughly 5 times (2 times with THF, 2 times with DMF, 1 time with methanol) to remove any excess guests adhered to the MOF surface. The nanocrystals were separated from the suspension by centrifugation at 8000 rpm for 10 min.

Synthesis of TPE@MIL-68(In): 9 mL DMF solution of 4.8 mmol benzenedicarboxylate (BDC) plus triethylamine (NEt_3, 9.6 mmol) was combined with 2 mL THF solution of 0.2 mmol TPE. After the combination, 6 mL DMF solution of 4.8 mmol indium nitrate was immediately added into the mixture. Then the product was washed thoroughly 5 times (2 times with THF, 2 times with DMF, 1 time with methanol) to remove the guests adhered to the MOF surface. The nanocrystals of TPE@MIL-68(In) were separated from the suspension by centrifugation at 8000 rpm for 10 min.

Sample Preparation for Fluorescence Characterization: TPE suspension was prepared by diluting 0.1 M TPE THF solution in water (the volume ratio of water to THF was 99:1). The pellets for mechanofluorochromism study were made by using a manual hydraulic press (Specac Atlas) with a 1.2 cm diameter steel die under compressive forces of 1, 2, 3, and 4 tones.

Electrospinning: The solution for electrospinning was prepared by dissolving 13.7 g of polyurethane (PU) in 86.3 g of *N*, *N*-dimethylformamide (DMF), yeilding 13.7 wt.% of PU in DMF, and afterward, 100 mg of TPE@ZIF-71 powder was added into a 10 g of as-prepared solution. The mixed solution was loaded into a 5 mL glass syringe with a G-19 needle emitter (nozzle) connected and dispensed utilizing an automatic syringe pump. The infusion rate was set to 0.25 mL/h. A high voltage of 11.5 kV was applied between the nozzle and the base collector set 18 cm vertically apart.

Doctor Blade: The polymer solution for doctor-blade membrane fabrication was prepared by dissolving 13.7 g HSV900 polyvinylidene fluoride (PVDF) powder in 86.3 g dimethylacetamide (DMA) to yield 13.7 wt.% PVDF in DMA. Then, 100 mg of TPE@ZIF-71 powder was added into the 10 g of 13.7 wt.% PVDF solution. The membranes were deposited using an automatic doctor-blade apparatus (MTI Corporation, MSK-AFA-II). The thickness was set to 0.95 mm, and the coating speed was set to 10 mm/s.

Materials Characterization: The morphologies, optical phase images, and nanoFTIR results were examined using the neaSNOM instrument (neaspec GmbH) based on a tapping-mode AFM where a platinum-coated tip (cantilever resonance frequency 250 kHz, nominal tip radius ~20 nm) was illuminated by a broadband infrared laser. To suppress background contributions, the signal was modulated at the third harmonic of the tip frequency for optical phase images, and at the second harmonic for nanoFTIR absorption spectra. Each spectrum was obtained from averaging over 14 individual measurements with an integration time of 14 s, and subsequently normalized to the spectrum of the silicon substrate. The PXRD pattern was recorded using a Rigaku MiniFlex with a Cu Kα source (1.541 Å). Steady-state fluorescent spectra, lifetime, and QY were recorded employing the FS-5 spectrofluorometer (Edinburgh Instruments). For lifetime TCSPC measurement, a 362.5 nm laser was used and the stop condition was set to be at 10,000 counts. FTIR results were recorded by using a Nicolet iS10 FTIR spectrometer. TGA was performed using a TGA-Q50 machine (TA Instruments) equipped with a platinum sample holder under an N_2 inert atmosphere at a heating rate of 10 °C/min from 30 to 800 °C.

Solution ^{1}H NMR Spectroscopy: Samples for NMR were dissolved in a solution composed of 500 μL methanol-d4 and 50 μL DCl / D_2O (35 wt%). All NMR spectroscopy was done at 298 K using a Bruker Avance III spectrometer operating at 600 MHz, equipped with a BBO Prodigy cryoprobe. Data was collected with 64 k points and a sweep width of 20 ppm, giving a digital resolution of 0.37 Hz. For the samples containing only TPE and only ZIF-71, a relaxation delay of 2 s was used. For the sample containing both TPE and ZIF-71, a relaxation delay of 20 s was used. Data was processed and analyzed using JEOL Jason. The ratio of TPE: dcIm was calculated from the integral ratio of the peak corresponding to the 8 ortho protons of the TPE phenyl groups and the peak corresponding to the single proton of the dcIm imidazole ring of ZIF-71. As each cage of ZIF-71 contains 24 dcIm ligands, the molar ratio was multiplied by 24 to obtain the guest loading (see Fig. S4).

Synchrotron Radiation Infrared Spectroscopy: High-resolution infrared (IR) vibrational spectra of all compounds were recorded at the Multimode InfraRed Imaging and Microspectroscopy (MIRIAM) Beamline B22 at the Diamond Light Source synchrotron. IR spectroscopy was performed in vacuum *via* a Bruker Vertex 80 V Fourier Transform IR (FTIR) with an Attenuated Total Reflection (ATR) accessory (Bruker Optics, Germany). The mid-IR spectra were collected using a standard DLaDTGS detector. For the far-infrared spectral range below 700 cm^{-1}, a bolometer cooled by liquid helium was used for the detection of terahertz signals. All spectra were acquired with a resolution of 4 cm^{-1} and a scanner velocity of 20 kHz.

Simulation of TPE molecules: Geometry optimization of the electronic ground state of TPE was performed using density functional theory (DFT) at the B3LYP/6-311G* level of theory [46–50], followed by normal mode analysis to confirm that the stationary structure is a local minimum, using the quantum chemical package Gaussian 16 [51]. The vibrational frequencies obtained were scaled by an empirical factor of 0.97 [52]. Also, efforts to obtain the simplest form of aggregates, i.e., dimers, were made to evaluate the possibility of encapsulation of aggregates by the MOF. For the simulations for dimers, the DFT-D3 version of Grimme et al [53]. was used to account for the dispersion correction.

Declaration of Competing Interest

The authors declare that they have no known competing financial interests or personal relationships that could have appeared to influence the work reported in this paper.

CRediT authorship contribution statement

Yang Zhang: Conceptualization, Methodology, Investigation, Writing – original draft, Writing – review & editing, Formal analysis. **Tao Xiong:** Software. **Annika F. Möslein:** Investigation, Writing – review & editing. **Samraj Mollick:** Investigation, Writing – review & editing. **Vishal Kachwal:** Investigation. **Jin-Chong Tan:** Methodology, Writing – review & editing, Funding acquisition, Supervision.

Acknowledgments

This work was supported by the EPSRC Impact Acceleration Account Award (EP/R511742/1) and the ERC Consolidator Grant (PROMOFS grant agreement 771575). We acknowledge the Diamond Light Source (Harwell, Oxford) for the award of beamtime SM25407; we thank Dr Mark Frogley for his assistance during the B22 MIRIAM beamline. We thank the Research Complex at Harwell (RCaH) for the provision of materials characterization facilities. We would like to acknowledge the use of the University of Oxford Advanced Research Computing (ARC) facility in carrying out this work (10.5281/zenodo.22558).

Supplementary materials

Supplementary material associated with this article can be found, in the online version, at doi:10.1016/j.apmt.2022.101434.

References

[1] Z. Chi, X. Zhang, B. Xu, X. Zhou, C. Ma, Y. Zhang, S. Liu, J. Xu, Recent advances in organic mechanofluorochromic materials, Chem. Soc. Rev. 10 (2012) 3878–3896.

[2] B.H. Di, Y.L. Chen, Recent progress in organic mechanoluminescent materials, Chin. Chem. Lett. 2 (2018) 245–251.

[3] Y. Jiang, An outlook review: mechanochromic materials and their potential for biological and healthcare applications, Mater. Sci. Eng. C Mater. Biol. Appl. (2014) 682–689.

[4] L. Ma, X. Feng, S. Wang, B. Wang, Recent advances in aiegen-based luminescent metal-organic frameworks and covalent organic frameworks, Mater. Chem. Front. 12 (2017) 2474–2486.

[5] Z. Ma, Z. Wang, X. Meng, Z. Ma, Z. Xu, Y. Ma, X. Jia, A mechanochromic single crystal: turning two color changes into a tricolored switch, Angew. Chem. Int. Ed. 2 (2016) 519–522.

[6] D.A. Davis, A. Hamilton, J. Yang, L.D. Cremar, D. Van Gough, S.L. Potisek, M.T. Ong, P.V. Braun, T.J. Martinez, S.R. White, J.S. Moore, N.R. Sottos, Force-induced activation of covalent bonds in mechanoresponsive polymeric materials, Nature 7243 (2009) 68–72.

[7] C. Löwe, C. Weder, Oligo(p-phenylene vinylene) excimers as molecular probes: deformation-induced color changes in photoluminescent polymer blends, Adv. Mater. 14 (2002) 1625–1629.

[8] A. Pucci, F. Di Cuia, F. Signori, G. Ruggeri, Bis(benzoxazolyl)stilbene excimers as temperature and deformation sensors for biodegradable poly(1,4-butylene succinate) films, J. Mater. Chem. 8 (2007) 783–790.

[9] K.P. Gan, M. Yoshio, T. Kato, Columnar liquid-crystalline assemblies of x-shaped pyrene–oligothiophene conjugates: photoconductivities and mechanochromic functions, J. Mater. Chem. C 22 (2016) 5073–5080.

[10] J. Han, J. Sun, Y. Li, Y. Duan, T. Han, One-pot synthesis of a mechanochromic AIE luminogen: implication for rewritable optical data storage, J. Mater. Chem. C 39 (2016) 9287–9293.

[11] D.C. Wang, Y. Lei, W. Jiao, Y.F. Liu, C.H. Mu, X. Jian, A review of helical carbon materials structure, synthesis and applications, Rare Met. 1 (2021) 3–19.

[12] Z. Yang, Z. Chi, Z. Mao, Y. Zhang, S. Liu, J. Zhao, M.P. Aldred, Z. Chi, Recent advances in mechano-responsive luminescence of tetraphenylethylene derivatives with aggregation-induced emission properties, Mater. Chem. Front. 5 (2018) 861–890.

[13] A. Karmakar, P. Samanta, S. Dutta, S.K. Ghosh, Fluorescent "turn-on" sensing based on metal-organic frameworks (MOFs), Chem. Asian J. 24 (2019) 4506–4519.

[14] Z. Zhao, J.W.Y. Lam, B.Z. Tang, Tetraphenylethene: a versatile AIE building block for the construction of efficient luminescent materials for organic light-emitting diodes, J. Mater. Chem. 45 (2012) 23726–23740.

[15] D.D. La, S.V. Bhosale, L.A. Jones, S.V. Bhosale, Tetraphenylethylene-based AIE-active probes for sensing applications, ACS Appl. Mater. Interfaces 15 (2018) 12189–12216.

[16] J. Dong, P. Shen, S. Ying, Z.J. Li, Y.D. Yuan, Y. Wang, X. Zheng, S.B. Peh, H. Yuan, G. Liu, Y. Cheng, Y. Pan, L. Shi, J. Zhang, D. Yuan, B. Liu, Z. Zhao, B.Z. Tang, D. Zhao, Aggregation-induced emission-responsive metal–organic frameworks, Chem. Mater. 15 (2020) 6706–6720.

[17] Z. Hu, H. Zhang, Y. Chen, Q. Wang, M.R.J. Elsegood, S.J. Teat, X. Feng, M.M. Islam, F. Wu, B.Z. Tang, Tetraphenylethylene-based color-tunable AIE-ESIPT chromophores, Dye. Pigment. (2020) 108175.

[18] M.H. Xie, W. Cai, X. Chen, R.F. Guan, L.M. Wang, G.H. Hou, X.G. Xi, Q.F. Zhang, X.L. Yang, R. Shao, Novel CO_2 fluorescence turn-on quantification based on a dynamic AIE-active metal-organic framework, ACS Appl. Mater. Interfaces 3 (2018) 2868–2873.

[19] J. Luo, Z. Xie, J.W. Lam, L. Cheng, H. Chen, C. Qiu, H.S. Kwok, X. Zhan, Y. Liu, D. Zhu, B.Z. Tang, Aggregation-induced emission of 1-methyl-1,2,3,4,5-pentaphenylsilole, Chem. Commun. 18 (2001) 1740–1741.

[20] Y. Liu, C. Deng, L. Tang, A. Qin, R. Hu, J.Z. Sun, B.Z. Tang, Specific detection of d-glucose by a tetraphenylethene-based fluorescent sensor, J. Am. Chem. Soc. 4 (2011) 660–663.

[21] N.B. Shustova, B.D. McCarthy, M. Dinca, Turn-on fluorescence in tetraphenylethylene-based metal-organic frameworks: an alternative to aggregation-induced emission, J. Am. Chem. Soc. 50 (2011) 20126–20129.

[22] Q. Zhang, J. Su, D. Feng, Z. Wei, X. Zou, H.C. Zhou, Piezofluorochromic metal-organic framework: a microscissor lift, J. Am. Chem. Soc. 32 (2015) 10064–10067.

[23] Q.Y. Li, Z. Ma, W.Q. Zhang, J.L. Xu, W. Wei, H. Lu, X. Zhao, X.J. Wang, AIE-active tetraphenylethene functionalized metal-organic framework for selective detection of nitroaromatic explosives and organic photocatalysis, Chem. Commun. 75 (2016) 11284–11287.

[24] L. Yu, H. Wang, W. Liu, S.J. Teat, J. Li, Blue-light-excitable, quantum yield enhanced, yellow-emitting, zirconium-based metal–organic framework phosphors formed by immobilizing organic chromophores, Cryst. Growth Des. 12 (2019) 6850–6854.

[25] H. Yuan, K. Wang, K. Yang, B. Liu, B. Zou, Luminescence properties of compressed tetraphenylethene: the role of intermolecular interactions, J. Phys. Chem. Lett. 17 (2014) 2968–2973.

[26] J. Shi, N. Chang, C. Li, J. Mei, C. Deng, X. Luo, Z. Liu, Z. Bo, Y.Q. Dong, B.Z. Tang, Locking the phenyl rings of tetraphenylethene step by step: understanding the mechanism of aggregation-induced emission, Chem. Commun. 86 (2012) 10675–10677.

[27] M.P. Aldred, C. Li, M.Q. Zhu, Optical properties and photo-oxidation of tetraphenylethene-based fluorophores, Chemistry 50 (2012) 16037–16045.

[28] A.K. Chaudhari, H.J. Kim, I. Han, J.C. Tan, Optochemically responsive 2D nanosheets of a 3D metal-organic framework material, Adv. Mater. 27 (2017) 1701463.

[29] T.L. Easun, F. Moreau, Y. Yan, S. Yang, M. Schroder, Structural and dynamic studies of substrate binding in porous metal-organic frameworks, Chem. Soc. Rev. 1 (2017) 239–274.

[30] J. Heine, K. Muller-Buschbaum, Engineering metal-based luminescence in coordination polymers and metal-organic frameworks, Chem. Soc. Rev. 24 (2013) 9232–9242.

[31] W.P. Lustig, S. Mukherjee, N.D. Rudd, A.V. Desai, J. Li, S.K. Ghosh, Metal-organic frameworks: functional luminescent and photonic materials for sensing applications, Chem. Soc. Rev. 11 (2017) 3242–3285.

[32] J. Aguilera-Sigalat, D. Bradshaw, Synthesis and applications of metal-organic framework-quantum dot (QD@MOF) composites, Coord. Chem. Rev. (2016) 267–291.

[33] M.D. Allendorf, R. Medishetty, R.A. Fischer, Guest molecules as a design element for metal-organic frameworks, MRS Bull. 11 (2016) 865–869.

[34] M. Gutiérrez, C. Martín, M. Van der Auweraer, J. Hofkens, J.C. Tan, Electroluminescent guest@MOF nanoparticles for thin film optoelectronics and solid-state lighting, Adv. Opt. Mater. 16 (2020) 2000670.

[35] L. Wang, H. Xu, J. Gao, J. Yao, Q. Zhang, Recent progress in metal-organic frameworks-based hydrogels and aerogels and their applications, Coord. Chem. Rev. (2019) 213016.

[36] H. Xu, J. Gao, X. Qian, J. Wang, H. He, Y. Cui, Y. Yang, Z. Wang, G. Qian, Metal-organic framework nanosheets for fast-response and highly sensitive luminescent sensing of Fe^{3+}, J. Mater. Chem. A 28 (2016) 10900–10905.

[37] A.F. Möslein, M. Gutierrez, B. Cohen, J.C. Tan, Near-field infrared nanospectroscopy reveals guest confinement in metal-organic framework single crystals, Nano Lett. 10 (2020) 7446–7454.

[38] Y. Zhang, M. Gutiérrez, A.K. Chaudhari, J.C. Tan, Dye-encapsulated zeolitic imidazolate framework (ZIF-71) for fluorochromic sensing of pressure, temperature, and volatile solvents, ACS Appl. Mater. Interfaces 33 (2020) 37477–37488.

[39] Y. Zhang, J.C. Tan, Electrospun rhodamine@MOF/polymer luminescent fibers with a quantum yield of over 90%, iScience 9 (2021) 103035.

[40] M.R. Ryder, B. Civalleri, T.D. Bennett, S. Henke, S. Rudic, G. Cinque, F. Fernandez-Alonso, J.C. Tan, Identifying the role of terahertz vibrations in metal-organic frameworks: from gate-opening phenomenon to shear-driven structural destabilization, Phys. Rev. Lett. 21 (2014) 215502.

[41] J.C. Tan, B. Civalleri, C.C. Lin, L. Valenzano, R. Galvelis, P.F. Chen, T.D. Bennett, C. Mellot-Draznieks, C.M. Zicovich-Wilson, A.K. Cheetham, Exceptionally low shear modulus in a prototypical imidazole-based metal-organic framework, Phys. Rev. Lett. 9 (2012) 095502.

[42] Z. Su, Y.R. Miao, S.M. Mao, G.H. Zhang, S. Dillon, J.T. Miller, K.S. Suslick, Compression-induced deformation of individual metal-organic framework microcrystals, J. Am. Chem. Soc. 5 (2015) 1750–1753.

[43] Y. Bai, Y. Dou, L.H. Xie, W. Rutledge, J.R. Li, H.C. Zhou, Zr-based metal-organic frameworks: design, synthesis, structure, and applications, Chem. Soc. Rev. 8 (2016) 2327–2367.

[44] A. Noguera-Díaz, J. Villarroel-Rocha, V.P. Ting, N. Bimbo, K. Sapag, T.J. Mays, Flexible ZIFs: probing guest-induced flexibility with CO_2, N_2 and Ar adsorption, J. Chem. Technol. Biotechnol. 12 (2019) 3787–3792.

[45] K. Zhang, R.P. Lively, C. Zhang, R.R. Chance, W.J. Koros, D.S. Sholl, S. Nair, Exploring the framework hydrophobicity and flexibility of ZIF-8: from biofuel recovery to hydrocarbon separations, J. Phys. Chem. Lett. 21 (2013) 3618–3622.

[46] A.D. Becke, Density-functional exchange-energy approximation with correct asymptotic behavior, Phys. Rev. A 6 (1988) 3098–3100.

[47] S.H. Vosko, L. Wilk, M. Nusair, Accurate spin-dependent electron liquid correlation energies for local spin density calculations: a critical analysis, Can. J. Phys. (1980) 1200–1211.

[48] C. Lee, W. Yang, R.G. Parr, Development of the Colle-Salvetti correlation-energy formula into a functional of the electron density, Phys. Rev. B 2 (1988) 785–789.

[49] A.D. McLean, G.S. Chandler, Contracted Gaussian basis sets for molecular calculations. I. Second row atoms, Z=11–18, J. Chem. Phys. 10 (1980) 5639–5648.

[50] R. Krishnan, J.S. Binkley, R. Seeger, J.A. Pople, Self-consistent molecular orbital methods. XX. A basis set for correlated wave functions, J. Chem. Phys. 1 (1980) 650–654.

[51] M.J. Frisch, G.W. Trucks, H.B. Schlegel, G.E. Scuseria, M.A. Robb, J.R. Cheeseman, G. Scalmani, V. Barone, G.A. Petersson, H. Nakatsuji, X. Li, M. Caricato, A.V. Marenich, J. Bloino, B.G. Janesko, R. Gomperts, B. Mennucci, H.P. Hratchian, J.V. Ortiz, A.F. Izmaylov, J.L. Sonnenberg, Williams, F. Ding, F. Lipparini, F. Egidi, J. Goings, B. Peng, A. Petrone, T. Henderson, D. Ranasinghe, V.G. Zakrzewski, J. Gao, N. Rega, G. Zheng, W. Liang, M. Hada, M. Ehara, K. Toyota, R. Fukuda, J. Hasegawa, M. Ishida, T. Nakajima, Y. Honda, O. Kitao, H. Nakai, T. Vreven, K. Throssell, J.A. Montgomery, J.E. Peralta, F. Ogliaro, M.J. Bearpark, J.J. Heyd, E.N. Brothers, K.N. Kudin, V.N. Staroverov, T.A. Keith, R. Kobayashi, J. Normand, K. Raghavachari, A.P. Rendell, J.C. Burant, S.S. Iyengar, J. Tomasi, M. Cossi, J.M. Millam, M. Klene, C. Adamo, R. Cammi, J.W. Ochterski, R.L. Martin, K. Morokuma, O. Farkas, J.B. Foresman, D.J. Fox, Gaussian 16, Revision C.01; Gaussian Inc.: Wallingford, CT, 2016.

[52] G. Rauhut, P. Pulay, Transferable scaling factors for density functional derived vibrational force fields, J. Phys. Chem. 10 (1995) 3093–3100.

[53] S. Grimme, J. Antony, S. Ehrlich, H. Krieg, A consistent and accurate ab initio parametrization of density functional dispersion correction (DFT-D) for the 94 elements H-Pu, J. Chem. Phys. 15 (2010) 154104.

Paper IV: Turn-On Fluorescence Chemical Sensing Through Transformation of Self-Trapped Exciton States at Room Temperature

Turn-on fluorescence chemical sensing through transformation of self-trapped exciton states at room temperature

*Yang Zhang, Samraj Mollick, Michele Tricarico, Jiahao Ye, Dylan Sherman, Jin-Chong Tan**

Multifunctional Materials & Composites (MMC) Laboratory, Department of Engineering Science, University of Oxford, Parks Road, Oxford OX1 3PJ, United Kingdom.

*Corresponding author
E-mail: jin-chong.tan@eng.ox.ac.uk

Abstract

Most of the current fluorescence sensing materials belong to the turn-off type, which are hard to detect toxic substances such as benzene, toluene, and xylene (BTX) due to the lack of active chemical sites, thereby limiting their development and practical use. Herein we show a guest-host mechanism stemming from the confined emitter's self-trapped exciton (STE) states or electron-phonon coupling to achieve turn-on fluorescence. We designed a luminescent guest@metal-organic framework (LG@MOF) composite material, termed perylene@MIL-68(In), and established its E-type excimeric emission properties in the solid-state. Upon exposure to BTX, especially xylene, we show the E-excimer readily converts into the Y-excimer due to nanoconfinement of the MOF structure. Such a transformation elevates the fluorescence intensity, thus realizing a turn-on type fluorescent sensor for detecting BTX solvents. Our results further demonstrate the controlling of the STE states of perylene at room temperature (versus previous report of < 50 K) made possible *via* nanoscale confinement, paving the way to enabling turn-on type fluorescence sensors fit for engineering practical use.

Keywords: Turn-on fluorescent sensor; Self-trapped exciton states; Perylene; Metal-organic framework (MOF); Luminescent guest@MOF

1. Introduction

Fluorescence sensing has recently become a popular research direction because of its simplicity, portability, rapid response, high selectivity, and high sensitivity [1-4]. It works mainly through weakening of the fluorescence intensity (i.e. quenching mechanism) of the materials by affecting the photoinduced electron transfer [5], Förster resonance energy transfer (FRET) [6, 7], and/or charge transfer [8] to achieve "turn-off" type fluorescence sensing.

These mechanisms pose two major limitations in principle. The first is that the side effects of environmental interference cannot be efficiently ruled out. For example, molecules in the environment, like water moisture and oxygen, may also cause a decrease in emission intensity [9, 10]. The second limitation is that it is hard to produce a fluorescent sensor to detect molecules that do not have active chemical sites [11], such as "BTX", namely benzene, toluene, and xylene. However, the demand for BTX sensing is urgent because exposure to this kind of substances presents the risk of reproductive toxicity, and it is prevalent in industrial production and daily life [12-15].

To address the foregoing problems, herein we demonstrate a novel "*turn-on*" type fluorescence sensing for the detection of BTX molecules without active chemical sites, we accomplished this by controlling the self-trapped exciton (STE) states of the emitters. Theoretically, the analyte may affect the coupling effect between excitons and phonons, thereby resulting in different fluorescent response that can be harnessed for sensor applications.

In terms of STE, perylene is a good starting point to discuss. This material is widely used in light-emitting diodes [16, 17], photovoltaics [18], and organic field effect transistors [19]. More importantly, perylene possesses two different STE states (Y- and E-state) with different fluorescent properties [16, 20-22]. Nevertheless, it is hard to use perylene itself as a sensor. The reasons are that perylene is susceptible to aggregation-caused quenching (ACQ) effect, it thus has no fluorescence in the solid-state form, and the solubility of perylene is not high in many solvents, making it challenging to form a dimeric structure or STE states [23].

Because of their porous, ordered, and highly adjustable crystalline structure, metal-organic frameworks (MOFs) are believed to be one of the most promising materials to combine with perylene to yield tunable luminescent sensing properties [24-28]. In principle, the pores/channels of the MOF "host" can be used to encapsulate and isolate perylene "guest" molecules to overcome the ACQ effect, and when confined within a MOF structure, the solubility of perylene is no longer a concern [29]. Of note, the emerging concept of confinement

of a luminescent guest (LG) in a MOF host, conferring a "LG@MOF" composite system, has huge potential for designing and engineering unconventional turn-on type luminescent sensors and lighting devices [30].

In this work, we demonstrate a fluorescence sensing LG@MOF material by encapsulating perylene into an easy-to-synthesise and stable Materials of Institut Lavoisier-68(In) [MIL-68(In)]. For this perylene@MIL-68(In) composite, we show that perylene exhibits the E-state excimer fluorescence in solid-state powder form, and it changes to Y-state excimer emission when exposed to BTX, resulting in a prominent turn-on type sensing response. To the best of our knowledge, this kind of turn-on sensing from the transformation of STE states is the first example realized in the research field of LG@MOFs [30]. Significantly, it is also the first time the transformation of perylene E-state to Y-state is evidenced at room temperature condition.

2. Synthesis and Structure of the Perylene@MIL-68(In) Composite System

The perylene@MIL-68(In) system was synthesized by using the simple one-pot high concentration reaction (HCR) method, a facile approach first described by Chaudhari *et al* [31, 32]. Full details of the synthetic steps for perylene@MIL-68(In) are given in the Experimental Section. It is worth mentioning that due to the deprotonation of triethylamine (TEA), this is the first method to produce MIL-68(In) at room temperature. The resulting composite materials were subsequently characterized by powder X-ray diffraction (PXRD), attenuated total reflection Fourier-transform infrared spectroscopy (ATR-FTIR), synchrotron radiation infrared spectroscopy (SR-IR), nanoindentation, and scanning electron microscope (SEM).

From Figure 1a, it can be seen that the PXRD patterns of prepared MIL-68(In) MOF host and perylene@MIL-68(In) are consistent with the simulations, which indicate that MIL-68(In) crystal structure is successfully generated by HCR method and the introduction of perylene molecules will not hinder the crystal formation of the MOF host [33]. The same conclusion can also be drawn from the FTIR results (Figure 1c) due to the high similarity between the spectra of MIL-68(In) and perylene@MIL-68(In). The nanoindentation results show the hardness of the crystal increased by ~20% after the encapsulation of perylene (Figure S1 and Table S1), suggesting the formation of perylene@MIL-68(In) may have given rise to an interstitial hardening effect. SEM images (Figure 1b and Figure S2) show the synthesized MIL-68(In) and perylene@MIL-68(In) possess nanosized columnar crystals, which coincide with the typical

crystal morphology of MIL-68 produced through a long reaction time (hours) under high temperature (> 55 ℃) [34]. Together, our results demonstrate that the HCR method can produce MIL-68(In) immediately under a significantly milder reaction condition potentially useful for future commercialization.

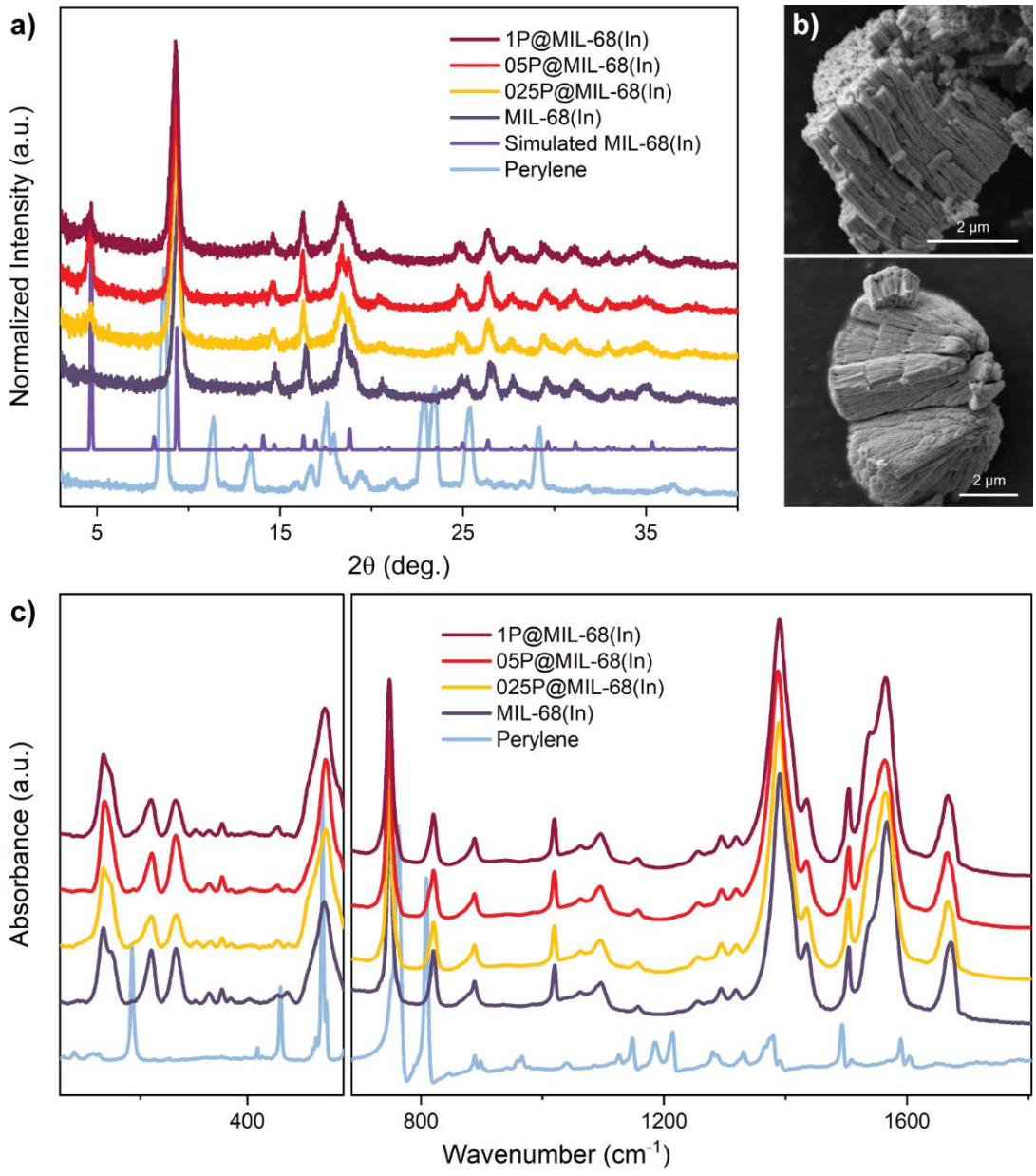

Figure 1. (a) Comparison of the XRD patterns of the simulated/synthesized MIL-68(In) and perylene@MIL-68(In) featuring three perylene concentrations (1P, 05P, and 025P designate the amount of perylene used in the synthesis to be 1 mmol, 0.5 mmol, and 0.25 mmol). (b) SEM images of MIL-68(In). (c) FTIR results of the MIL-68(In) and perylene@MIL-68(In), (left: from SR-FTIR; right: from ATR-FTIR).

3. Luminescent Properties of Perylene@MIL-68(In)

We then performed photophysical characterization of the perylene@MIL-68(In) with different amounts of perylene guest loading. The excitation and emission spectra are shown in Figures 2a and 2b, respectively. It is apparent that the fluorescence properties of the perylene@MIL-68(In) systems are derived from perylene molecules because pure MIL-68(In) is virtually non-emissive at the selected excitation wavelength of 440 nm. For the perylene@MIL-68(In) at all three concentrations, their emission peaks can be divided into two parts: 1) a small peak at around 475 nm; 2) a broad and intense peak at around 600 nm. On the basis of previous studies on perylene [16, 20-23], we reasoned that the first peak originates from the emission of free excitons, and the second peak is attributed to the STE emission. These photophysical characteristics indicate the α-perylene-like structure is generated inside the MIL-68(In) channel and emits as the E-state excimer [35]. Furthermore, the lifetime data of the system obtained by using the time-correlated single-photon-counting (TCSPC) technique (Table S2, Figure S4) show a lifetime component (τ_4) that is around 18 ns, further supporting the existence of the E-state excimer. It is worth mentioning that the fluorescence performance of perylene solutions with different concentrations verified our theoretical hypothesis in the introduction part: Perylene is challenging to form a dimeric structure and induce excimer emission due to the solubility problem, but MOFs can help to overcome this limitation through confinement in nanoscale pores/channels.

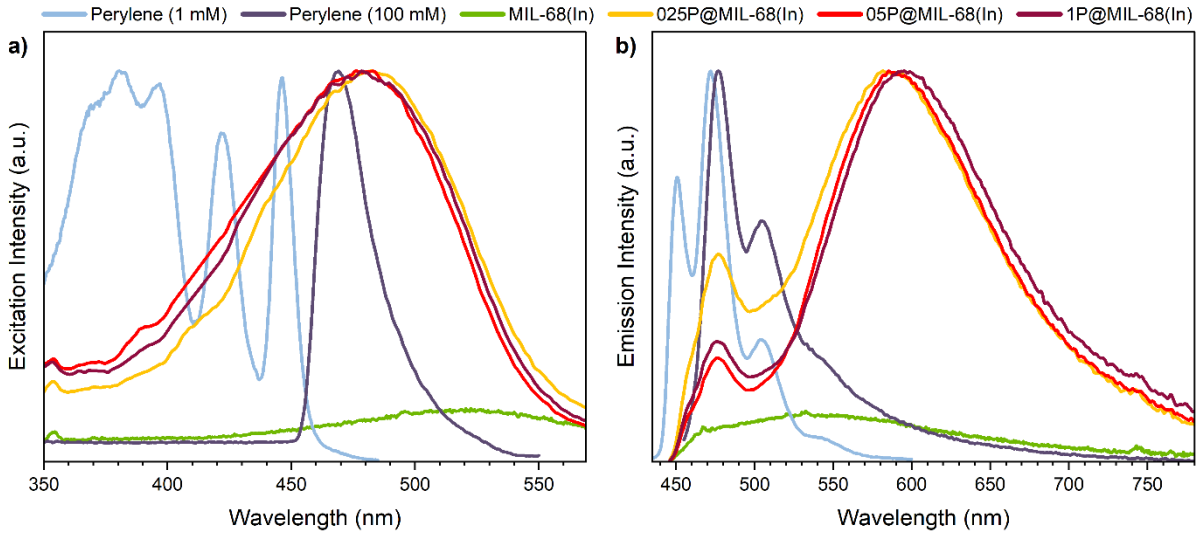

Figure 2. Normalized (a) excitation spectra (measured under em@600 nm) and (b) emission spectra (measured under ex@440 nm) of perylene solutions, MIL-68(In) powders, and perylene@MIL-68(In) in solid state. Note: MIL-68(In) is not normalized due to its weak signal.

Considering the E-state emission characteristic, the channel size of MIL-68(In) (16 and 6 Å), and the previous research outcome in ref [20], it is reasonable to infer that in the channel of MIL-68(In), perylene molecules exist as disordered dimeric structure. This means the longest axis of perylene molecules tilts in the radial direction of MIL-68(In) channels, as shown in Scheme 1(c). This kind of structural alignment of confined guests also explains the incremental red-shift evidenced for the 025P, 05P, and 1P@MIL-68(In) samples (Figure 2b), because the dimeric perylene can interact with the adjacent perylenes, and the interaction will be enhanced with the increase of perylene amount trapped within the MOF channel. The decrease in quantum yields (QY, Table S3) and excimer lifetime (τ_4, Table S2, Figure S4) when the perylene amount increases also supports the proposed structure, as the enhanced interactions will increase the non-radiative decay [24, 28].

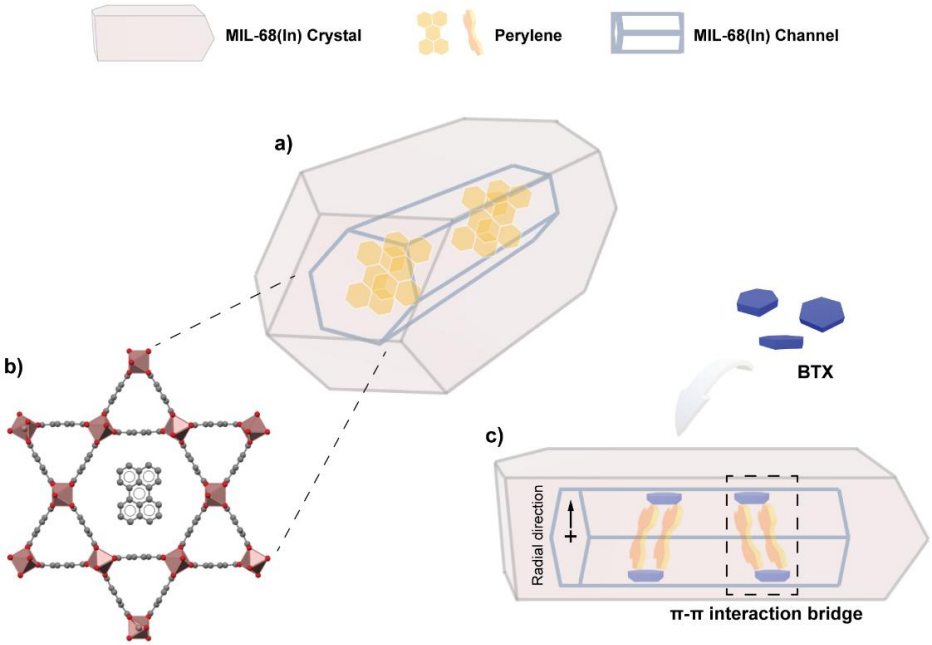

Scheme 1. (a-b) Illustrations of the LG@MOF crystal structure of perylene@MIL-68(In) and its initial molecular configuration under confinement of 1-D channels. (b) Proposed sensing mechanism of perylene@MIL-68(In) subject to benzene, toluene, xylene (BTX) molecules. Color scheme: indium in dark red, carbon in gray, and oxygen in red.

4. BTX Sensing Performance of Perylene@MIL-68(In)

Subsequently, we tested the benzene, toluene, and xylene (BTX) sensing properties of the perylene@MIL-68(In) system. In order to better observe the subtle changes, we chose the 025P@MIL-68(In) with the least amount of perylene and the highest QY for testing. As shown in Figure 3, perylene@MIL-68(In) delivers prominent turn-on sensing response with a slight

blue-shift and splitting of the emission peak (~600 nm) when exposed to the BTX molecules in solution. On the contrary, when exposed to DMF/acetone, such polar aprotic electron-deficient solvents, the peak at 600 nm exhibits a red-shift with a decline in its intensity.

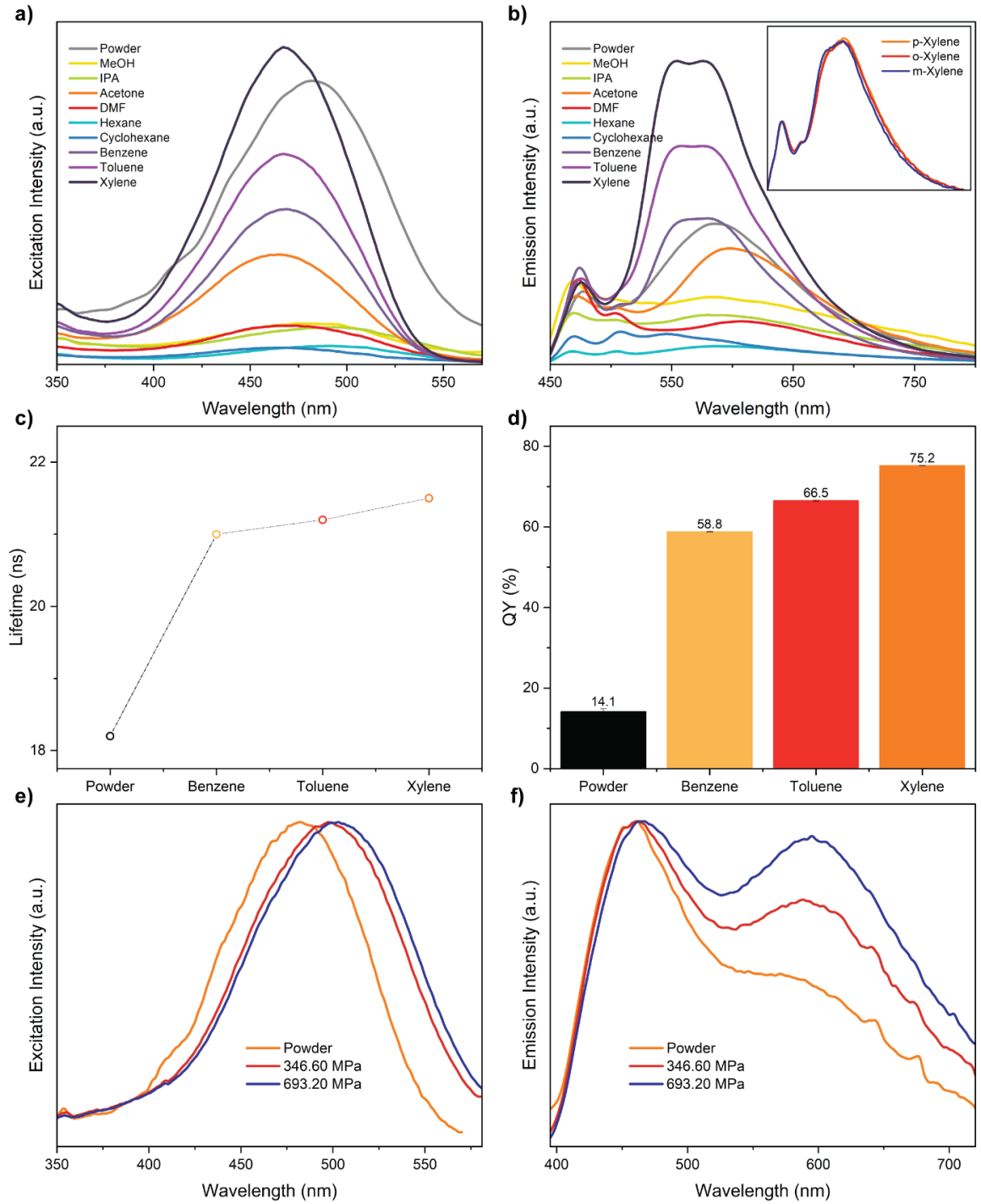

Figure 3. (a) Excitation (measured under em@600 nm) and (b) emission spectra (measured under ex@440 nm) of 025P@MIL-68(In) in different solvents. The inset of (b) shows the emission spectra of 025P@MIL-68(In) in p-, o-, m-xylene. (c) Lifetimes (excimer component) and (d) QYs of 025P@MIL-68(In) powders and when mixed in BTX. (e) Normalized excitation (measured under em@600 nm) and emission spectra (measured under ex@380 nm) of 025P@MIL-68(In) and its pellets.

The rising intensity and splitting of the peak at ~600 nm (Figure 3b) can be explained by the perylene in the MIL-68(In) channels undergoing a transformation from the E-state to Y-state [22]. This kind of transformation can be attributed to the formation of the π-π interaction bridge depicted in Scheme 1. When the perylene inside encounters BTX, such electron-rich solvents, the organic linker of MIL-68(In) (BDC), BTX, and dimeric perylene form a relatively strong π-π interaction "chain", thereby inducing an effect similar to the lattice confinement effect [22, 24, 36, 37]. In that situation, the electron-phonon coupling of the E-state will be affected to generate the Y-state. Compared with the single emission characteristic of E-state, Y-emission itself possesses multiple luminescent peaks, higher peak intensity, and a shorter peak wavelength [22]. Therefore, when exposed to BTX, the perylene@MIL-68(In) peak showed an intensity enhancement, splitting, and blue-shift. The deconvolution result of the emission peak (Figure S3) reveals the typical feature of the Y-excimer, in which the fitted peaks denoted as 2, 3, and 4 obviously correspond to the emission of Y-excimer reported by ref [22].

Furthermore, based on that, the occurrence of higher peak intensity and more pronounced peak splitting upon contact with xylene (compared to benzene and toluene) can also be understood. As the electron-donating ability of BTX becomes stronger (i.e., benzene < toluene < xylene), the π-π interaction bridge will become stronger correspondingly, resulting in a more substantial confinement effect for perylene in the channel [38]. It is worth mentioning that the Y-emission can only be observed at temperatures below 50 K for pure perylene [22]. Remarkably, herein we show for the first time that, thanks to the LG@MOF assembly the transformation between the E-state and Y-state is realized at room temperature.

To further validate the proposed theory, we performed the lifetime and QY measurements on perylene@MIL-68(In) (Figure 3c and 3d). The lifetime data shown in Figure 3c, Table S4, and Figure S5 suggest that the 18 ns time component (belonging to the E-state) increases when contacting BTX solvents [23]. Meanwhile, the QY also shows an increasing trend. More importantly, this rise can be associated with BTX electron-donating ability (Figure 3b-d): higher electron-donating ability, larger lifetime and QY. These phenomena indicate that the non-radiative decay of perylene in the MIL-68(In) is reduced due to the π-π interaction bridge, thus inducing a strong confinement effect and proving the transformation from the E- to Y-emission.

The fluorescence performance of perylene@MIL-68(In) subject to different compressive pressures also supports our theory. According to the previous studies [24, 37, 38], it can be deduced that when the pressure increases, the π-π interaction between the linker (BDC) and perylene will increase, thus causing perylene to becoming more tightly constrained. The excitation and emission spectra of the perylene@MIL-68(In) under pressure (Figure 3e and 3f) illustrate that, when the interaction is enlarged, the peak intensity corresponding to the perylene excimer increases. Furthermore, the τ_4 excimer lifetime also increases sharply with pressure rise (Table S5, Figure S6), compared with the τ_1 to τ_3 lifetime components which are relatively unchanging. Therefore, it is shown that enhancing the π-π interaction in this LG@MOF system does enhance the confinement effect and hence resulting in a stronger excimer emission. The pressure-dependent luminescence data further substantiate the rational of our proposed theory from another standpoint.

By way of comparison, the behavior of perylene@MIL-68(In) when exposed to electron-deficient solvents can be explained by the proposed theory as well. When the system is in DMF/acetone solvents, the emission at ~600 nm shows a relative decline and red-shift (Figure 3b). In Table S4 and Figure S5, the perylene@MIL-68(In) lifetime is smaller in DMF and acetone than in BTX. Based on the theory, those can be interpreted as electron-deficient solvents reducing the π-π interaction between the BDC linkers and perylene, making the dimeric structure to becoming more closely combined.

5. Conclusions

In conclusion, we have shown the facile synthesis of perylene@MIL-68(In) at ambient conditions by harnessing the HCR method. Of note, the perylene@MIL-68(In) exhibits the E-excimer emission characteristics in the solid-state. When exposed to BTX, the perylene molecules present in the MIL-68(In) channels will receive a strong confinement effect and affect the STE states. This guest-host confinement effect switches the E-state to Y-state emission, resulting in the turn-on fluorescent response when subject to the electron-rich BTX solvents. The sensing mechanism proposed here using the transformation between different STE states is the first exemplar in the field of LG@MOF research. The simple synthesis method and the uncommon turn-on type sensing behavior have opened up a new approach for developing highly-selective fluorescence sensors.

ACKNOWLEDGMENTS

This work was supported by the EPSRC Impact Acceleration Account Award (EP/R511742/1) and the ERC Consolidator Grant (PROMOFS grant agreement 771575). We acknowledge the Diamond Light Source (Harwell, Oxford) for the award of beamtime SM27504; we thank Dr Gianfelice Cinque for his assistance during the B22 MIRIAM beamline. We thank the Research Complex at Harwell (RCaH) for the provision of materials characterization facilities. We would like to acknowledge Jingwei Chen and Professor Alexander M. Korsunsky for the acquisition of the FESEM images.

AUTHOR CONTRIBUTIONS

Conceptualization, Y.Z.; Methodology, Y.Z. and S.M.; Investigation, Y.Z.; MIL-68(In) Synthesis, S.M. and Y.Z.; Nanoindentation, M.T.; Synchrotron Beamtime, J.Y. and D.S.; Writing – Original Draft, Y.Z.; Writing – Review & Editing, Y.Z. and J.C.T.; Supervision, J.C.T.

Experimental Section

***Synthesis of Perylene@MIL-68(In) and MIL-68(In) by using HCR method*:** The synthesis was accomplished by leveraging the high-concentration reaction (HCR) method [31, 32]. 15 mL dimethylformamide (DMF) solution of 4.8 mmol benzenedicarboxylate (BDC) plus triethylamine (TEA, 9.6 mmol) was combined with 50 mL dichloromethane (DCM) solution of 0.25/0.5/1 mmol perylene. After the combination, 15 mL DMF solution of 4.8 mmol indium nitrate was immediately added into the mixture. Then the product was formed instantly and washed thoroughly 5 times (2 times with DCM, 2 times with DMF, 1 time with methanol) to remove the excess guests adhered to the external MOF surfaces. The nanocrystals of perylene@MIL-68(In) were separated from the suspension by centrifugation at 8000 rpm for 10 mins.

Sample Preparation for Fluorescence Characterization: The pellets for mechanofluorochromic study were made by using a manual hydraulic press (Specac Atlas) with a 1.2 cm diameter die under a uniaxial compressive force of 4 and 8 tones. Perylene@MIL-68(In) suspensions for solvatochromic study were prepared by diluting 5 mg of perylene@MIL-68(In) in 8 mL solvent.

Materials Characterization: The crystal morphologies and structures were examined under field-emission scanning electron microscopy (FESEM $LYRA_3$ GM TESCAN). Powder X-ray diffraction (PXRD) patterns were recorded using a Rigaku MiniFlex with a Cu Kα source (1.541 Å). The nanoindentation tests were conducted using an iMicro nanoindenter (KLA-Tencor). Steady-state fluorescent spectra, lifetime, and quantum yield (QY) were recorded employing the FS-5 spectrofluorometer (Edinburgh Instruments). For TCSPC lifetime measurement, a 445 nm laser was used and the stop condition was set to be at 10,000 counts. Attenuated Total Reflection Fourier Transform Infrared (ATR-FTIR) spectra were recorded by using a Nicolet iS10 FTIR spectrometer.

Synchrotron Radiation Infrared (SR-IR) Spectroscopy: High-resolution SR-IR vibrational spectra of all compounds were recorded at the Multimode InfraRed Imaging and Microspectroscopy (MIRIAM) Beamline B22 at the Diamond Light Source synchrotron. Measurements were performed in vacuum *via* a Bruker Vertex 80V FTIR with an ATR

accessory (Bruker Optics, Germany). For far-infrared spectral range below 700 cm^{-1}, a bolometer cooled by liquid helium was used for the detection of terahertz signals. All spectra were acquired with a resolution of 4 cm^{-1} and a scanner velocity of 20 kHz.

References

[1] Chowdhury, S.; Rooj, B.; Dutta, A.; Mandal, U., Review on Recent Advances in Metal Ions Sensing Using Different Fluorescent Probes. *J. Fluoresc.* **2018,** 28, 999-1021.

[2] Shin, Y.-H.; Teresa Gutierrez-Wing, M.; Choi, J.-W., Review—Recent Progress in Portable Fluorescence Sensors. *J. Electrochem. Soc.* **2021,** 168, 017502.

[3] Wu, D.; Sedgwick, A. C.; Gunnlaugsson, T.; Akkaya, E. U.; Yoon, J.; James, T. D., Fluorescent Chemosensors: the Past, Present and Future. *Chem. Soc. Rev.* **2017,** 46, 7105-7123.

[4] Silva, A. P. d.; Eilers, J.; Zlokarnik, G., Emerging Fluorescence Sensing Technologies: From Photophysical Principles to Cellular Applications. *Proc. Natl. Acad. Sci. U.S.A* **1999,** 96, 8336-8337.

[5] Aucejo, R.; Díaz, P.; García-España, E.; Alarcón, J.; Delgado-Pinar, E.; Torres, F.; Soriano, C.; Guillem, M. C., Naphthalene-Containing Polyamines Supported in Nanosized Boehmite Particles. *New J. Chem.* **2007,** 31, 44-51.

[6] Puthiyedath, T.; Bahulayan, D., A Click-Generated Triazole Tethered Oxazolone-Pyrimidinone Dyad: A Highly Selective Colorimetric and Ratiometric FRET Based Fluorescent Probe for Sensing Azide Ions. *Sens. Actuators B Chem.* **2017,** 239, 1076-1086.

[7] Ren, C.; Wang, H.; Mao, D.; Zhang, X.; Fengzhao, Q.; Shi, Y.; Ding, D.; Kong, D.; Wang, L.; Yang, Z., When Molecular Probes Meet Self-Assembly: An Enhanced Quenching Effect. *Angew. Chem. Int. Ed.* **2015,** 54, 4823-4827.

[8] Xu, Z.; Xiao, Y.; Qian, X.; Cui, J.; Cui, D., Ratiometric and Selective Fluorescent Sensor for CuII Based on Internal Charge Transfer (ICT). *Org. Lett.* **2005,** 7, 889–892.

[9] Ma, D.; Li, B.; Cui, Z.; Liu, K.; Chen, C.; Li, G.; Hua, J.; Ma, B.; Shi, Z.; Feng, S., Multifunctional Luminescent Porous Organic Polymer for Selectively Detecting Iron Ions and 1,4-Dioxane via Luminescent Turn-off and Turn-on Sensing. *ACS Appl. Mater. Interfaces* **2016,** 8, 24097-24103.

[10] Zhou, J.; Li, H.; Zhang, H.; Li, H.; Shi, W.; Cheng, P., A Bimetallic Lanthanide Metal-Organic Material as a Self-Calibrating Color-Gradient Luminescent Sensor. *Adv. Mater.* **2015,** 27, 7072-7077.

[11] Liu, X.; Gong, Y.; Xiong, W.; Cui, L.; Hu, K.; Che, Y.; Zhao, J., Highly Selective Detection of Benzene, Toluene, and Xylene Hydrocarbons Using Coassembled Microsheets with Forster Resonance Energy Transfer-Enhanced Photostability. *Anal. Chem.* **2019,** 91, 768-771.

[12] Mirzaei, A.; Kim, J.-H.; Kim, H. W.; Kim, S. S., Resistive-Based Gas Sensors for Detection of Benzene, Toluene and Xylene (BTX) Gases: A Review. *J. Mater. Chem. C* **2018,** 6, 4342-4370.

[13] Qin, S.-J.; Hao, J.-N.; Xu, X.-Y.; Lian, X.; Yan, B., Highly Sensing Probe for Biological Metabolite of Benzene Series Pollutants Based on Recyclable Eu^{3+} Functionalized Metal-Organic Frameworks Hybrids. *Sens. Actuators B Chem.* **2017,** 253, 852-859.

[14] Kansal, A., Sources and Reactivity of NMHCs and VOCs in the Atmosphere: A Review. *J. Hazard. Mater.* **2009,** 166, 17-26.

[15] An, Y. R.; Kim, S. J.; Yu, S.-Y.; Yoon, H.-J.; Song, M.-K.; Ryu, J.-C.; Hwang, S. Y., Identification of Genetic/Epigenetic Biomarkers for Supporting Decision of VOCs Exposure. *BioChip J.* **2013,** 7, 1-5.

[16] Ma, L.; Tan, K. J.; Jiang, H.; Kloc, C.; Michel-Beyerle, M. E.; Gurzadyan, G. G., Excited-State Dynamics in an Alpha-Perylene Single Crystal: Two-Photon- and

Consecutive Two-Quantum-Induced Singlet Fission. *J. Phys. Chem. A* **2014,** 118, 838-843.
[17] Angadi, M. A.; Gosztola, D.; Wasielewski, M. R., Organic Light Emitting Diodes Using Poly(phenylenevinylene) Doped with Perylenediimide Electron Acceptors. *Mater. Sci. Eng. B* **1999,** 63, 191-194.
[18] Schmidt-Mende, L.; Fechtenkötter, A.; Müllen, K.; Moons, E.; Friend, R. H.; MacKenzie, J. D., Self-Organized Discotic Liquid Crystals for High-Efficiency Organic Photovoltaics. *Science* **2001,** 293, 1119-1122.
[19] Jones, B. A.; Ahrens, M. J.; Yoon, M. H.; Facchetti, A.; Marks, T. J.; Wasielewski, M. R., High-Mobility Air-Stable N-Type Semiconductors with Processing Versatility: Dicyanoperylene-3,4:9,10-Bis(dicarboximides). *Angew. Chem. Int. Ed.* **2004,** 43, 6363-6366.
[20] Tange, M.; Okazaki, T.; Liu, Z.; Suenaga, K.; Iijima, S., Room-Temperature Y-type Emission of Perylenes by Encapsulation within Single-Walled Carbon Nanotubes. *Nanoscale* **2016,** 8, 7834-7839.
[21] Nishimura, H.; Yamaoka, T.; Mizuno, K.-i.; Iemura, M.; Matsui, A., Luminescence of Free and Self-Trapped Excitons in α- and β-Perylene Crystals. *J. Phys. Soc. Jpn.* **1984,** 53, 3999-4008.
[22] Walker, B.; Port, H.; Wolf, H. C., The Two-Step Excimer Formation in Perylene Crystals. *Chem. Phys.* **1985,** 92, 177-185.
[23] Katoh, R.; Sinha, S.; Murata, S.; Tachiya, M., Origin of the Stabilization Energy of Perylene Excimer as Studied by Fluorescence and Near-IR Transient Absorption Spectroscopy. *J. Photochem. Photobiol. A: Chem.* **2001,** 145, 23-34.
[24] Zhang, Y.; Gutiérrez, M.; Chaudhari, A. K.; Tan, J. C., Dye-Encapsulated Zeolitic Imidazolate Framework (ZIF-71) for Fluorochromic Sensing of Pressure, Temperature, and Volatile Solvents. *ACS Appl. Mater. Interfaces* **2020,** 12, 37477-37488.
[25] Allendorf, M. D.; Bauer, C. A.; Bhakta, R. K.; Houk, R. J., Luminescent Metal-Organic Frameworks. *Chem. Soc. Rev.* **2009,** 38, 1330-1352.
[26] Heine, J.; Muller-Buschbaum, K., Engineering Metal-Based Luminescence in Coordination Polymers and Metal-Organic Frameworks. *Chem. Soc. Rev.* **2013,** 42, 9232-9242.
[27] Lustig, W. P.; Mukherjee, S.; Rudd, N. D.; Desai, A. V.; Li, J.; Ghosh, S. K., Metal-Organic Frameworks: Functional Luminescent and Photonic Materials for Sensing Applications. *Chem. Soc. Rev.* **2017,** 46, 3242-3285.
[28] Zhang, Y.; Tan, J. C., Electrospun Rhodamine@MOF/Polymer Luminescent Fibers with a Quantum Yield of Over 90%. *iScience* **2021,** 24, 103035.
[29] Allendorf, M. D.; Foster, M. E.; Leonard, F.; Stavila, V.; Feng, P. L.; Doty, F. P.; Leong, K.; Ma, E. Y.; Johnston, S. R.; Talin, A. A., Guest-Induced Emergent Properties in Metal-Organic Frameworks. *J. Phys. Chem. Lett.* **2015,** 6, 1182-1195.
[30] Gutierrez, M.; Zhang, Y.; Tan, J. C., Confinement of Luminescent Guests in Metal-Organic Frameworks: Understanding Pathways from Synthesis and Multimodal Characterization to Potential Applications of LG@MOF Systems. *Chem. Rev.* **2022**.
[31] Chaudhari, A. K.; Kim, H. J.; Han, I.; Tan, J. C., Optochemically Responsive 2D Nanosheets of a 3D Metal-Organic Framework Material. *Adv. Mater.* **2017,** 29, 1701463.
[32] Chaudhari, A. K.; Han, I.; Tan, J. C., Multifunctional Supramolecular Hybrid Materials Constructed from Hierarchical Self-Ordering of In Situ Generated Metal-Organic Framework (MOF) Nanoparticles. *Adv. Mater.* **2015,** 27, 4438-4446.
[33] Xiong, T.; Zhang, Y.; Donà, L.; Gutiérrez, M.; Möslein, A. F.; Babal, A. S.; Amin, N.; Civalleri, B.; Tan, J.-C., Tunable Fluorescein-Encapsulated Zeolitic Imidazolate

Framework-8 Nanoparticles for Solid-State Lighting. *ACS Appl. Nano Mater.* **2021,** 4, 10321-10333.

[34] Embrechts, H.; Kriesten, M.; Ermer, M.; Peukert, W.; Hartmann, M.; Distaso, M., In Situ Raman and FTIR Spectroscopic Study on the Formation of the Isomers MIL-68(Al) and MIL-53(Al). *RSC Adv.* **2020,** 10, 7336-7348.

[35] Freydorf, E. V.; Kinder, J.; Michel-Beyerle, M. E., On Low Temperature Fluorescence of Perylene Crystals. *Chem. Phys.* **1978,** 27, 199-209.

[36] Tamai, N.; Porter, C.; Masuhara, H., Femtosecond Transient Absorption-Spectroscopy of a Single Perylene Microcrystal under a Microscope. *Chem. Phys. Lett.* **1993,** 211, 364-370.

[37] Chaudhari, A. K.; Tan, J. C., Mechanochromic MOF Nanoplates: Spatial Molecular Isolation of Light-Emitting Guests in a Sodalite Framework Structure. *Nanoscale* **2018,** 10, 3953-3960.

[38] Zhang, Y.; Xiong, T.; Möslein, A. F.; Mollick, S.; Kachwal, V.; Babal, A. S.; Amin, N.; Tan, J. C., Nanoconfinement of Tetraphenylethylene in Zeolitic Metal-Organic Framework for Turn-on Mechanofluorochromic Stress Sensing. *Appl. Mater. Today* **2022,** 27, 101434.